Measurement of Unpolarized Inclusive Neutral Current Cross Sections in Positron-Proton Collisions at $\sqrt{s} \simeq 320$ GeV

Diplomarbeit

vorgelegt von

Shiraz Habib

Institut für Experimentalphysik
Universität Hamburg

Hamburg
July, 2005

This is to certify that this report represents independent work done by the author, and that where others have contributed, they have been suitably acknowledged.
Hamburg, July 2005.

Hiermit versichere ich, dass die vorliegende Arbeit selbständig und nur unter Verwendung der angegebenen Hilfsmittel erstellt wurde.
Hamburg, Juli 2005.

Abstract

A measurement of the unpolarized inclusive single and double differential neutral current cross sections in e^+p scattering at a center of mass energy of $\sqrt{s} \simeq 320$ GeV is presented. The data was collected by the H1 detector during the years 2003 and 2004, after the HERA luminosity upgrade, and represents one of the first of such post-upgrade measurements. The data corresponds to an integrated luminosity of 47.4 pb^{-1} and an average longitudinal polarization of the lepton beam of $-0.9\% \pm 0.3 \pm 0.8$. The cross section measurements were made for four-momentum transfer squared Q^2 values between 120 and 30 000 GeV^2 and Bjorken x between 0.002 and 0.65. The details of the analysis are presented here.

The single and double differential cross section measurements presented here are found to agree with previously published data as well as Standard Model predictions within the uncertainties quoted.

Kurzfassung

Diese Arbeit stellt die Analyse von Wechselwirkungen zwischen Positronen und Protonen am HERA-Beschleuniger bei einer Schwerpunktsenergie von $\sqrt{s} \simeq 320$ GeV vor. Die Daten wurden in den Jahren 2003 und 2004 mit dem H1 Detektor genommen und entsprechen einer integrierten Luminosität von 47.4 pb^{-1} und einer mittleren Polarisation von $-0.9\% \pm 0.3 \pm 0.8$. Die Wirkungsquerschnitte wurden gemessen für Werte des Quadrats des Vierer-Impuls-Übertrages Q^2 zwischen 150 und 30 000 GeV^2 und Bjorken-x-Werte zwischen 0.002 und 0.65. Die gesamte hierfür notwendige Analysekette wird beschreiben.

Die hier vorgestellte Messung gehört zu den ersten Ergebnissen aus nach dem HERA-Luminositätsupgrade (HERA II) genommenen Daten. Die gemessenen einfach und doppelt differentiellen Wirkungsquerschnitte stimmen innerhalb der experimentellen Unsicherheiten gut mit dem Standardmodell und mit den bereits veröffentlichten HERA-I-Ergebnissen überein.

Contents

Introduction

Scattering is an established tool used by particle physicists to probe the structure of matter. When Rutherford scattered α-particles on a gold target, he was astounded to find a significant number of particles deflected through very large angles. This was inconsistent with the idea held at the time that the charge of the atom was uniformly distributed over its volume. The observation could be explained if one assumed the charge to be tightly packed into what is now called the nucleus, and so the atomic model acquired structure.

In the late sixties Bjorken predicted that at high energies the inelastic structure functions were independent of the relevant scale Q^2[1]. This *scaling* was verified at SLAC in the early seventies. Callan and Gross proposed the relationship between the Bjorken's scaling functions which was also experimentally confirmed. Scaling and the Callan-Gross relation were consequences of the fact that the proton consisted of pointlike spin-$\frac{1}{2}$ constituents, now identified as quarks. The model of the *proton* had now acquired structure, and became known as the Quark Parton Model(QPM). In the QPM, the sum of the momentum distributions of the quarks is directly related to the F_2 structure function. Experimentally, F_2 is derived from the double differential *ep* cross section. This sets the stage as an experimental test of a theory of proton structure.

Today Quantum Chromodynamics (QCD) is the field theory of the strong interactions, the force which holds the quarks together in the proton. As it turns out, the strong mediators, *gluons*, together with the sea quarks carry about half of the proton's momentum. QCD is not yet able to *predict* the quark and gluon densities however.

HERA continues the tradition of deep inelastic scattering by colliding electrons[1] with protons at a centre of mass energy of $\simeq 320$ GeV. The collisions at HERA therefore provide a laboratory to study structure functions at Bjorken $x \gtrsim 10^{-6}$ for Q^2 values $0.1 \gtrsim \mathrm{GeV}^2$. At the highest values of Q^2 the weak interactions of the Standard Model (SM) may also be tested.

This thesis explores the *high* Q^2 regime of the kinematic region accessible at HERA. Measurements of the unpolarized neutral current single and double differential cross sec-

[1]Throughout the thesis, the term "electron" refers generically to both electrons and positrons, unless otherwise stated.

tions are presented in the kinematic range $120 < Q^2 < 30\,000$ GeV^2 and $0.002 < x < 0.65$. The data used was collected by the H1 detector during operation of the HERA collider over the period September 2003 to August 2004, that is, after the HERA luminosity upgrade. The upgrade allows the possibility of colliding longitudinally polarized leptons on unpolarized protons. The data set corresponds to an integrated luminosity of 47.4 pb^{-1} and an average polarization of $-0.9\% \pm 0.3 \pm 0.8$, which is $\simeq 0$ within error.

This report takes the reader along the following path. Chapter 1 summarizes the theory relevant to the analysis. It is difficult to have an appreciation for any measurement without some knowledge of the instruments used, therefore Chapter 2 introduces the HERA collider and the H1 detector. As simulations are used extensively throughout the analysis, Monte Carlo programs and their application are discussed in Chapter 3. Chapter 4 discusses the various methods of reconstructing the event kinematics and the choice made for the analysis. Chapter 5 explains in some detail the complete event selection used to reduce the data set to the final sample upon which the cross section is measured. Finally Chapter 6 explains the method used to extract the cross section and gives the final results, along with comparisons to previously taken data and Standard Model expectations. A summary then follows.

Chapter 1

Theoretical Considerations

This chapter provides a short summary of the theoretical background which both motivates the cross section measurement as well as provides a basis for its interpretation. The kinematics of deep inelastic scattering are first introduced, followed by the cross section and structure function formulae derived using quantum field theory. Quantum chromodynamics and its role in determining the proton´s structure, as well as previously deduced parton distributions are also presented.

1.1 Kinematics of Deep Inelastic Scattering (DIS)

In the framework of Quantum Field Theory, the scattering of an electron e with a proton p is mediated by the exchange of a gauge boson. This process is represented in Figure 1.1(a). The four-momenta depicted are:

- l for the incoming lepton
- l' for the outgoing lepton
- q for the exchanged boson $(= l - l')$
- p for the incoming proton
- p' for the outgoing hadronic final state X.

According to the type of boson exchanged, the interaction can be classified as either neutral current (NC) if the boson carries no electric charge, or charged current (CC) if it does. Thus in the Standard Model, NC interactions are mediated by a photon (γ) or Z boson. CC interactions on the other hand are mediated by a W boson ($W^{\pm}$), and the outgoing lepton is a neutrino ν_e (or anti-neutrino $\bar{\nu_e}$) due to charge and lepton number conservation.

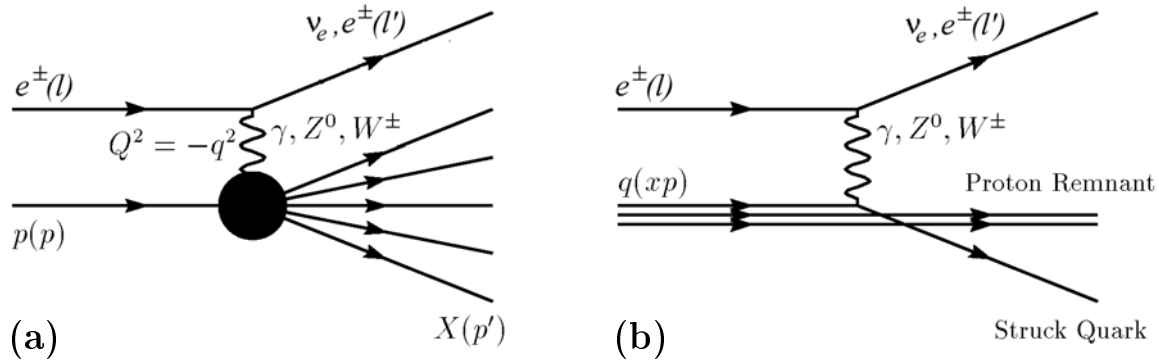

Figure 1.1: *(a)Representation of ep scattering in the single boson exchange approximation. The four-momenta of the incoming and scattered lepton are denoted by l and l' respectively. Those of the incoming proton and the hadronic final state X are denoted by p and p' respectively. The exchanged boson carries the four-momentum q. (b) Feynman diagram representation of ep scattering in the Quark Parton Model.*

For given electron and proton beam energies, which corresponds to a center of mass energy squared $s = (l + p)^2$, the event kinematics can be defined by any two[1] Lorentz invariants from the four-momentum transfer squared Q^2 , the Bjorken scaling variable x, and the inelasticity y defined by:

$$Q^2 = -q^2 = -(l - l')^2, \qquad (0 \leq Q^2 \leq s) \tag{1.1}$$

$$x = \frac{Q^2}{2p \cdot q}, \qquad (0 \leq x \leq 1) \tag{1.2}$$

$$y = \frac{p \cdot q}{p \cdot l}, \qquad (0 \leq y \leq 1) \tag{1.3}$$

where Q^2, x and y are related via $Q^2 = sxy$ (neglecting the electron and proton masses). Q^2 represents the transverse resolving power of the virtual photon probe with wavelength $\lambda = 1/\sqrt{Q^2}$ (setting $\hbar = c = 1$); y is the fraction of the incident electron energy given to the proton, in a frame where the proton is at rest. Figure 1.1(b) shows *ep* scattering as represented in the Quark Parton Model (QPM) in which the *inelastic* scattering of the electron with the proton is now interpreted as *elastic* scattering of the electron with an essentially free proton constituent - nowadays held to be a quark[2]. The variable x then represents the fraction of the momentum carried by the struck quark in the infinite momentum frame where the proton's energy is so much larger than its mass, that it and

[1] Intuitively, two degrees of freedom are allowed since the electron can be scattered at various angles, for each of which, the invariant mass of the hadronic final state X can vary.

[2] The original term for a constituent of the proton was a *parton*, which was used when quarks and gluons were not already well established.

its constituents can be regarded as massless[3].

1.2 Neutral Current Inclusive Cross Section and Structure Functions

If the cross section for the NC process $ep \to eX$ includes all final states X then it is called an *inclusive* cross section.

After correcting for QED radiative effects (see *Section* 6.4), the NC inclusive cross section for unpolarized beams, the cross section actually measured in this analysis, is given by [14]:

$$\frac{d^2\sigma_{NC}^{e^{\pm}p}}{dxdQ^2} = \frac{2\pi\alpha^2}{xQ^4}\phi_{NC}^{\pm}(x,Q^2)(1+\Delta_{NC}^{\pm,weak}) \tag{1.4}$$

$$\text{where: } \phi_{NC}^{\pm} = Y_+\tilde{F}_2(x,Q^2) \mp Y_- x\tilde{F}_3(x,Q^2) - y^2\tilde{F}_L(x,Q^2) \tag{1.5}$$

$$\mathrm{Y}_{\pm} = 1 \pm (1-y)^2 \tag{1.6}$$

Here $\alpha \equiv \alpha(Q^2=0)$ is the fine structure constant. The $\Delta_{NC}^{\pm,weak}$ corrections are defined in [25] and are typically less than 1% but never more than 3%. $\phi_{NC}^{\pm}$ is the NC structure function term; it can be expressed as a linear combination of the generalised[4] structure functions $\tilde{F}_2$, $x\tilde{F}_3$ and $\tilde{F}_L$. The helicity dependences of the electroweak interactions are contained in $Y_{\pm}$. The Born cross section, order $\mathcal{O}(\alpha^2)$, is given by the term $\frac{2\pi\alpha^2}{xQ^4}\phi_{NC}^{\pm}(x,Q^2)$.

The generalized structure functions can be further decomposed into contributions from pure electromagnetic and weak contributions, as well as the contribution from γZ interference according to:

$$\tilde{F}_2 \equiv F_2 \quad - v_e\frac{\kappa Q^2}{Q^2+M_Z^2}F_2^{\gamma Z} \quad + (v_e^2+a_e^2)(\frac{\kappa Q^2}{Q^2+M_Z^2})^2F_2^Z, \tag{1.8}$$

$$x\tilde{F}_3 \equiv \quad - a_e\frac{\kappa Q^2}{Q^2+M_Z^2}xF_3^{\gamma Z} \quad + (2v_ea_e)(\frac{\kappa Q^2}{Q^2+M_Z^2})^2xF_3^Z, \tag{1.9}$$

with $\kappa^{-1} = 4\frac{M_W^2}{M_Z^2}(1-(\frac{M_W^2}{M_Z^2})$ in the on-mass-shell scheme [26]. Here v_e and a_e are the the vector and axial-vector weak couplings respectively of the electron to the Z^0. The structure function F_2 originates from pure γ exchange, F_2^Z and xF_3^Z from pure Z^0 exchange

[3]The lab frame at HERA where the proton energy is measured at 920 GeV can be considered an approximation to the infinite momentum frame.

[4]Generalized in the sense that the $\tilde{F}_i$s include the contributions from Z^0 exchange.

and $F_2^{\gamma Z}$ and $xF_3^{\gamma Z}$ from γZ interference. The longitudinal structure function $\tilde{F}_L$ may be decomposed in a manner similar to $\tilde{F}_2$. Its contribution is significant only at high y.

Over most of the kinematic range at HERA, the largest contribution to the cross section comes from pure photon exchange via F_2. The contribution due to Z^0 exchange only becomes significant at large Q^2.

In the QPM the structure functions F_2, $F_2^{\gamma Z}$ and F_2^Z are related to the sum of the various quark and anti-quark distributions $xq(x,Q^2)$ and $x\bar{q}(x,Q^2)$ by:

$$F_2 = x\sum_q e_q^2\{q+\bar{q}\} \tag{1.10}$$

$$F_2^{\gamma Z} = x\sum_q 2e_q v_q\{q+\bar{q}\} \tag{1.11}$$

$$F_2^Z = x\sum_q (v_q^2+a_q^2)\{q+\bar{q}\} \tag{1.12}$$

while $xF_3^{\gamma Z}$ and xF_3^Z are related to the difference, which determine the valence quark distributions $xq_v(x,Q^2)$,

$$xF_3^{\gamma Z} = 2x\sum_q e_q a_q\{q-\bar{q}\} = 2x\sum_{q=u,d} e_q a_q q_v \tag{1.13}$$

$$xF_3^Z = 2x\sum_q v_q a_q\{q-\bar{q}\} = 2x\sum_{q=u,d} v_q a_q q_v. \tag{1.14}$$

In equations 1.10 and 1.13, e_q is the charge of quark q, while v_q and a_q are respectively the vector and axial-vector weak coupling of the quarks to the Z^0. In the QPM, the longitudinal structure function $\tilde{F}_L \equiv 0$.

1.3 Quantum Chromodynamics(QCD) and Parton Distributions

Quantum chromodynamics is the theory of the strong interaction. The role of "charge" in QCD is *color* of which there are three kinds: red, green and blue. The strong force is mediated by massless *gluons*, which as well carry color, thus allowing gluons to couple with other gluons. The coupling of gluons to one another has the effect of causing the size of the running coupling constant α_s to get quite small as the distance between the interacting particles is reduced to that comparable to the size of the proton. This is known as *asymptotic freedom*. It is for this reason that the quarks within a proton at small distances can be considered to have very little interaction with each other.

The parton distributions of the proton are in principle determined by QCD since it is the strong force that holds the quarks together. Presently these distributions are not calculable and so are determined using QCD fits. One such fit, termed the *H1 PDF 2000 fit* [14] uses inclusive NC and CC data collected from the years 1997 to 2000 by the H1 Collaboration. The results are shown in Figure 1.2.

This thesis represents the first experimental step in the determination of structure functions and parton distributions, that is - an inclusive double differential cross section measurement using the most recent data collected by the H1 detector at the HERA collider.

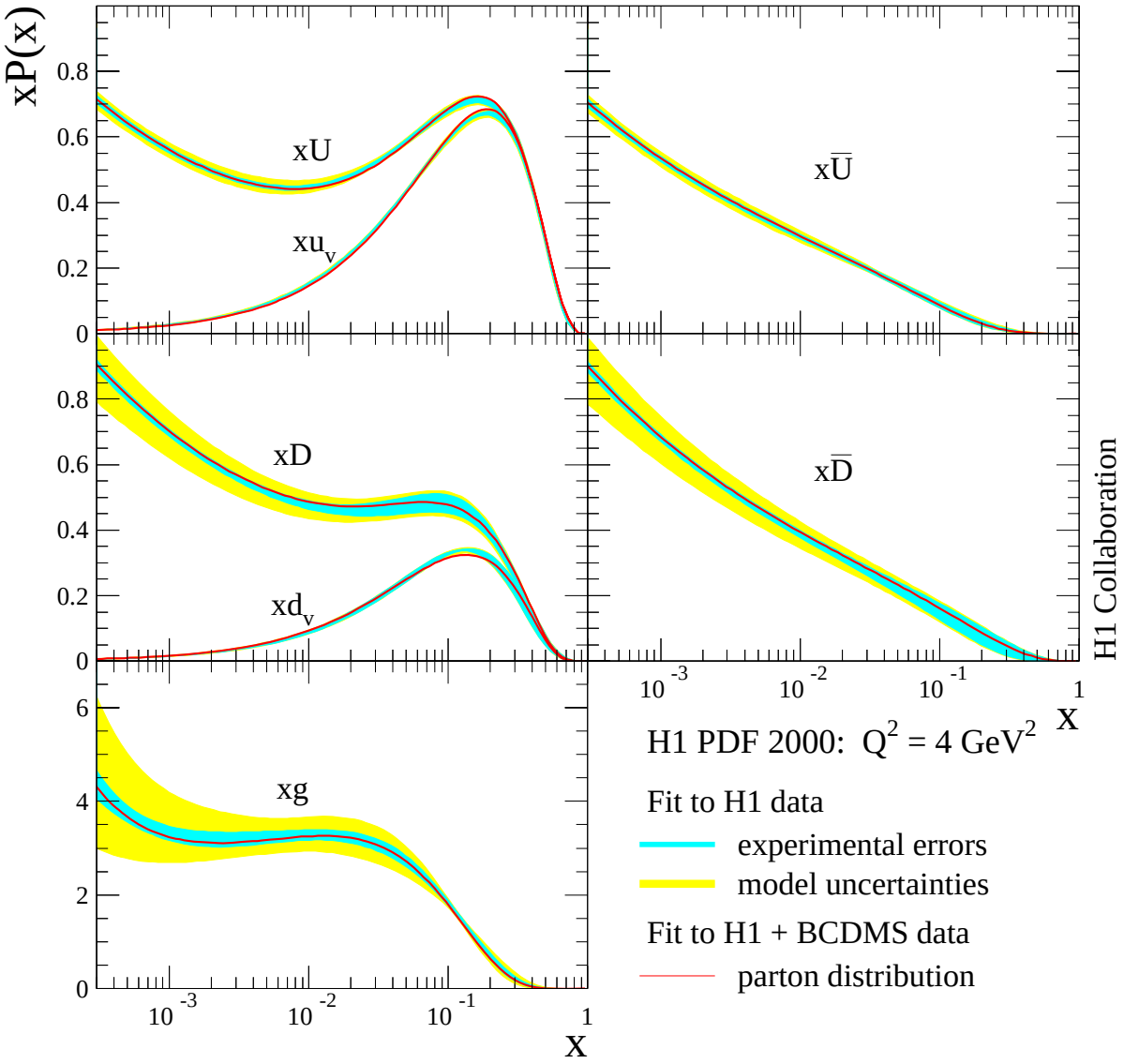

Figure 1.2: Parton distributions (a)xU, (b)$x\bar{U}$, (c)xD, (d)$x\bar{D}$ and (e) xg as determined from the H1PDF 2000 Fit to H1 data only. The distributions are shown at the initial scale $Q_0^2 = 4\ GeV^2$. The inner error band represents the experimental uncertainty as determined from the fit. The outer error band shows the total uncertainty by adding in quadrature the experimental and model uncertainties. The valence quark distributions (a)xu_v and (c)xd_v are also shown. For comparison, the parton distributions from the fit to H1 and BCDMS [14] data are shown as the full curves.

Chapter 2

The Experiment

To study the structure of the proton as described in Chapter 1 requires a device which produces ep collisions, that is the purpose of the collider. The observation of the interactions and measurement of the quantities of interest requires a detector. This chapter introduces the HERA collider and H1 detector. The collider is discussed with an emphasis on the HERA luminosity upgrade while the detector is discussed with an emphasis on those components most relevant to the analysis.

2.1 The Collider - HERA

The HERA particle accelerator (*Hadron-Elektron-Ring-Anlage*) located at DESY (*Deutsches Elektronen-Synchrotron*), Hamburg, brings together electrons at 27.6 GeV and protons at 920 GeV into a high energy collision with centre of mass energy $\sqrt{s} \approx 320$ GeV. The electron beam serves as an ideal probe into the structure of the proton since the electroweak interactions of electrons are well understood. Figure 2.1(a) shows a schematic view of the HERA storage ring with the four experiments H1 and ZEUS (colliding-beam), HERMES (lepton beam on gas target) and HERA-B (proton beam on nuclei). At HERA, the particles are produced in *bunches* which cross the interaction point every 96 ns.

HERAI → HERAII Luminosity Upgrade

August 2000 marked the end of the first phase of operation (HERA I) of HERA, with a total luminosity of 190 pb^{-1} having been delivered to H1 and ZEUS starting from 1992. In September 2000 the collider underwent a shutdown, the aim of which was to embark on a major luminosity upgrade program designed to increase the instantaneous luminosity by a factor 4 compared to HERA I [29]. This task involved the installation of almost 80 new magnets, and was a major engineering challenge. The increased luminosity was accompanied by an unforeseen increase in background. After much effort, the problem

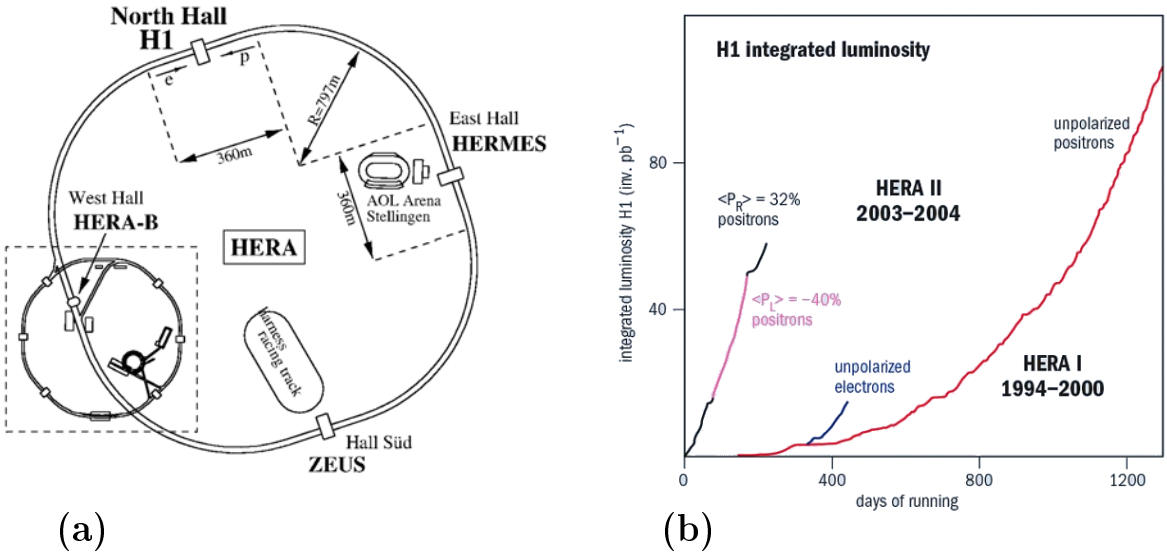

Figure 2.1: *(a) The HERA storage ring with the colliding-beam experiments H1 and ZEUS and the fixed target experiments HERMES and HERA-B. (b) Integrated luminosity collected by H1 during the running periods HERAI and HERAII [29].*

was reduced to a satisfactory level as H1 demonstrated in February 2004 tolerable levels of background up to the highest beam intensties. Thus by August 2004, 92 pb^{-1} of luminosity was delivered by HERA using positrons, the period considered in this analysis. Figure 2.1(b) shows that part of the delivered luminosity collected by H1 as a function of running day. After a short shutdown in August and September 2004 operations resumed using an e^- beam for the first time since 1999.

Another objective of the upgrade program was to supply longitudinally spin-polarized electron beams to the two colliding-beam experiments (prior to the upgrade, only HERMES had access to such a supply). This would be achieved by the installation of spin rotators before and after the interaction points Figure 2.2(a). By February 2003, HERA successfully delivered high longitudinal spin polarization, and in so doing became the world's first to achieve longitudinally polarized positron and high energy proton collisions. During the positron run, the polarization was tuned to values up to 50%. Figure 2.2(b) shows preliminary physics results of this effort: the total charged current cross section as a function of polarization[8].

Presently the plan is to continue with the e^- run until mid-2006, then switch back to positrons, and by mid-2007 complete the data-taking of HERA.

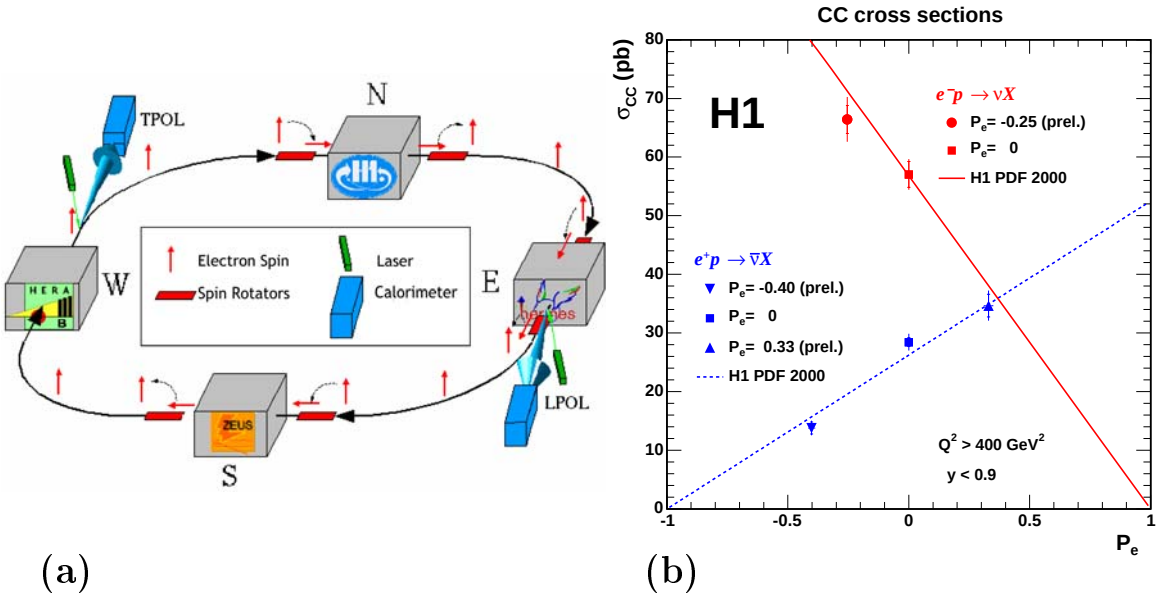

Figure 2.2: *(a) Spin rotators used to achieve longitudinally spin polarized lepton beams. (b) Total charged current cross section as a function of polarization.*

2.2 The Detector - H1

The purpose of the H1 detector is to identify particles produced in ep interactions, and reconstruct their four-momenta and trajectories. This is done by surrounding the interaction point with several *subdetectors*, each sensitive to the energetic particles produced. The energy lost by a partice traversing the detector medium is eventually converted into electrical signals which are then read out and interpreted as a physics quantity (energy or position for example). By combining the measurements of the various subdetectors using well understood techniques (such as track reconstruction), the *event* can be reconstructed.

Figure 2.3 shows a 3-dimensional view of the H1 detector. The ep collisions occur at or near the *nominal interaction point*, defined as the origin of the H1 frame of reference. The x-axis points in the horizontal direction towards the center of the HERA ring, the y-axis points upwards and the z-axis points in the flight direction of the incoming proton. It is convenient to refer to the regions of the detector in the positive and negative z direction relative to the nominal interaction point as the *forward* and *backward* regions respectively; the region surrounding the nominal interaction point is described as *central*. As the proton's momentum is much more than the electron's, most of the particles produced are scattered in the forward direction.

Particles produced in ep interactions first traverse the tracker, Figure 2.4, followed by

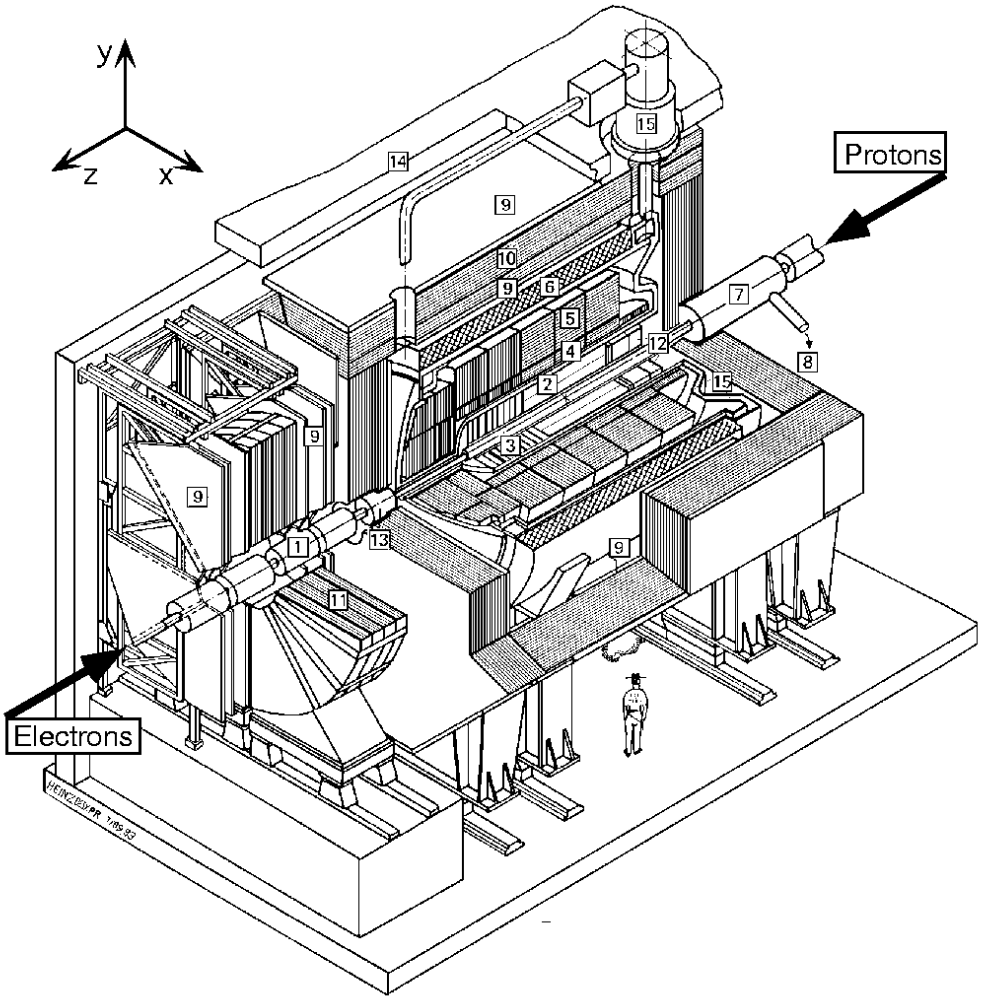

Figure 2.3: *3-Dimensional view of the H1 detector.*

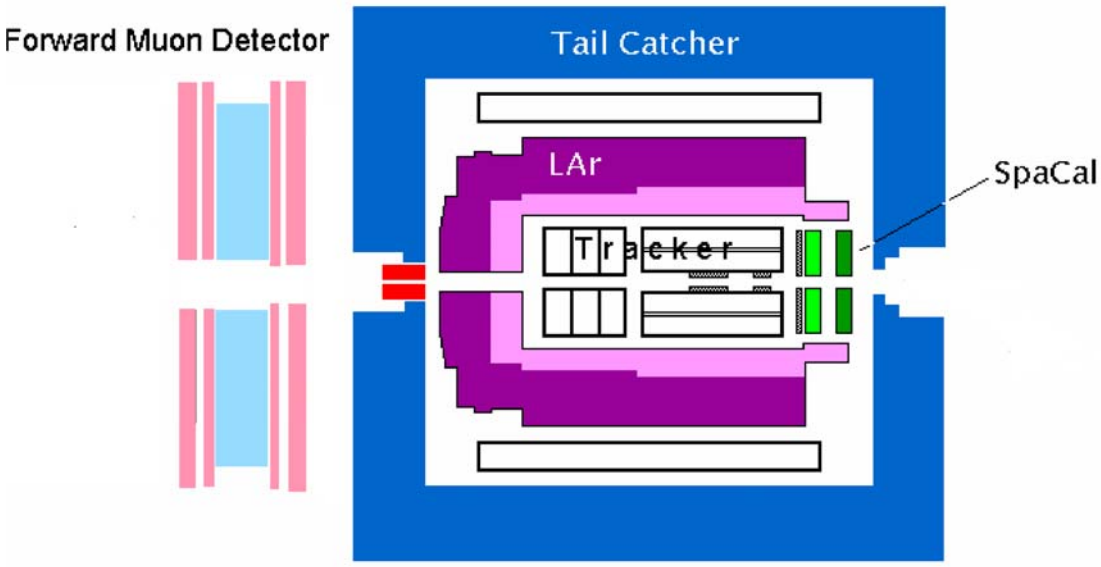

Figure 2.4: *Schematic side view of the H1 detector.*

the calorimeters (the Liquid Argon (LAr) calorimeter in the central and forward regions and the Lead-Fibre Spaghetti (SPACAL) calorimeter in the backward region). The iron return yoke (Tail Catcher) which surrounds the detector, detects particles that penetrate beyond the various calorimeters; this is important in identifying muons as well as reconstructing the hadronic shower tails. Beyond the iron in the forward region is the Forward Muon Detector (FMD): drift chambers in a toroidal magnetic field used to identify muons and measure their trajectories.

In a NC analysis apart from background rejection, the detector is used primarily to reconstruct the four-momenta of the scattered electron and hadronic final state (all particles excluding the scattered electron). With this in mind, the most important subdetectors used in this analysis are presented in the following pages.

2.3 The Calorimeters

The Liquid Argon Calorimeter

The LAr calorimeter covers the angular range $4^\circ \lesssim \theta \lesssim 153^\circ$ and is shown schematically in Figure 2.5. It is a sandwich calorimeter with the inner part (EM) for electromagnetic shower measurements and the outer (HAD) for hadronic measurements. The depth of the EM section is between 20 to 30 radiation lengths while the total depth of the calorimeter is between 5 and 8 hadronic interaction lengths. The EM section uses lead as the absorber

material while the HAD section uses stainless steel. Liquid argon is used as the sampling medium between the absorber plates.

The calorimeter is partitioned in the z direction into several distinct *wheels*, Figure 2.5(a):

- the Backward Barrel Electromagnetic calorimeter(BBE)
- the Central Barrel calorimeters (CB1, CB2, CB3)
- the Forward Barrel calorimeters (FB1, FB2)
- the Inner and Outer Forward calormeters (IF, OF)

The wheels are divided in ϕ into 8 octants, Figure 2.5(b). The octants of the BBE has a 16-fold symmetry, Figure 2.6. Each wheel is further divided into layers of cells. In total there are 44,000 cells. All the wheels have EM and HAD sections except for the BBE which has only an EM section and the OF which has only a HAD section.

The region between the wheels (z-cracks) and between the octants (ϕ-cracks), Figure 2.5, are not insrumented and prove problematic due to the presence of insensitive material which hampers the energy measurement and subsequent particle identification (see *Section 5.2*).

The most basic use of a calorimeter is an energy measurement, and test beam results of the LAr have shown an energy resolution of $\sigma_{em}(E)/E = 12\%/\sqrt{E/GeV} \oplus 1\%$ for electrons and $\sigma_{had}(E)/E = 50\%/\sqrt{E/GeV} \oplus 2\%$ for charged pions[4, 5, 6]. The 44,000 cells mentioned earlier also allow an excellent spatial resolution. The polar angle of the scattered electron (which is required to be in the LAr in the present analysis) is thus taken from the calorimeter measurement. The energy clusters (apart from the scattered electron) produced in the LAr contribute to the reconstruction of the hadronic final state (see *Section* 2.4).

The Spaghetti Calorimeter (SPACAL)

The SPACAL extends the solid angle calorimeter coverage into the angular range $153^\circ \lesssim \theta \lesssim 178^\circ$. It consists of scintillating lead fibres embedded in a lead absorber, and has also an electromagnetic and a hadronic section. The electromagnetic energy resolution is $\sigma_{em}(E)/E = (7.1 \pm 0.2)\%/\sqrt{E/GeV} \oplus (1.0 \pm 0.1)\%$ [21].

2.4 The Tracking System

At the heart of the H1 tracking system are the two drift chambers CJC1 (inner) and CJC2 (outer), Figures 2.7 and 2.8. With sensor wires running in the z direction, and using a

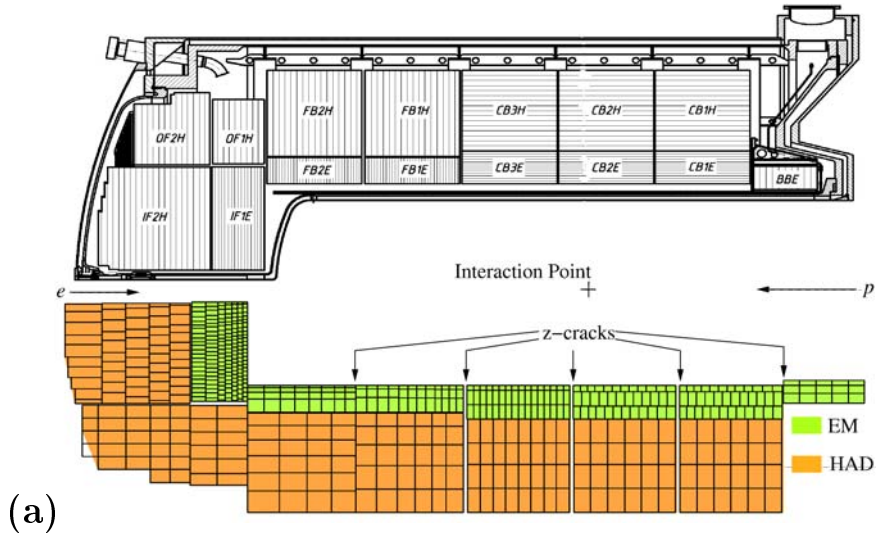

(a)

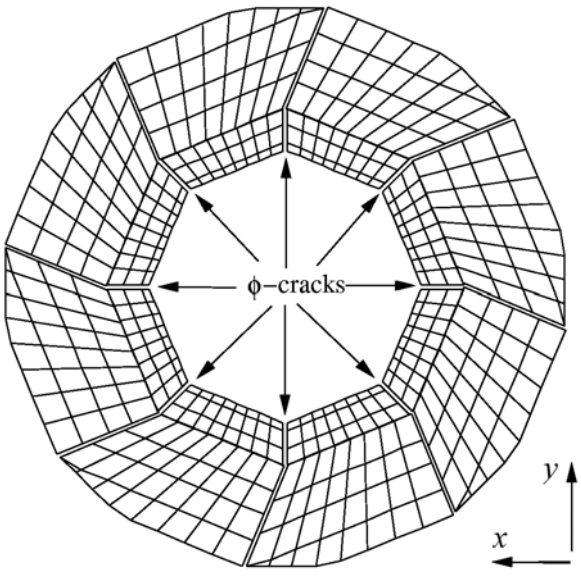

(b)

Figure 2.5: *(a) Schematic view of the wheel and cell structure of the LAr calorimeter. Shown are the Backward Barrel Electromagnetic (BBE), Central Barrel (CB1, CB2, CB3), Forward Barrel (FB1, FB2), Inner Forward (IF) and Outer Forward (OF) wheels, with the electromagnetic (EM) and hadronic (HAD) sections indicated. The z-cracks are also shown. (b) Schematic view of the octant structure of the CB1 wheel with ϕ cracks indicated.*

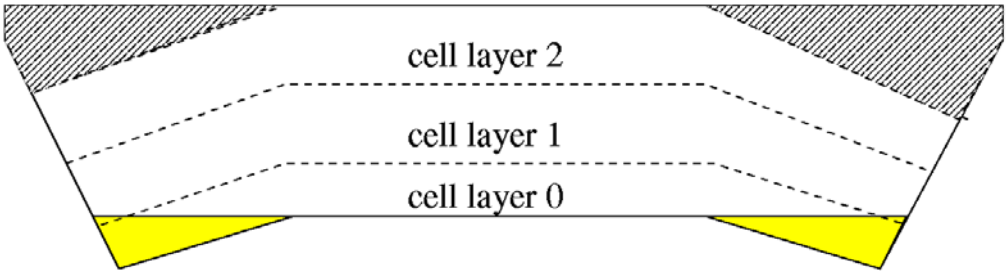

Figure 2.6: *Schematic view of a BBE octant showing the 16-fold symmetry. The grey areas indicate the regions where there is no overlap woth the CB1 wheels.*

1.15 T magnetic field parallel to the z-axis, charged particles run a helical course through the CJCs, producing *hits* which are used in the track reconstruction. The hit resolution in the radial plane is $\approx 170\mu$m. By using the collected charge at both ends of the wire, a z resolution between 2 to 3 cm results. The central outer z chamber (COZ)[1] is used to improve the precision of the z measurement having wires that run normal to the z direction. The silicon trackers are located just outside the beam pipe.

The Central Inner Proportional Chanmber (CIP2k) is a multiwire proportional chamber (MWPC) used for the purpose of triggering on the number of recognised track patterns that occur in the event near the central part of the detector [27]. In this thesis a study was made on the hit resolution of the CIP2k using muons and electrons, the results of which are presented in *Appendix A - Measurement of the Efficiency of the Central Inner Proportional Chamber (CIP2k) at H1, HERA II.*

Event timing signals from the CJC and CIP are also used in the analysis (see *Section* 2.5).

The presence of noise in the calorimeters can fake particles and so noise *suppression* is vital in reconstructing the HFS[2]]Reconstruction of the Hadronic Final State (HFS) The entities that are used in reconstructing the hadronic final state are clusters and tracks. Only the tracks that are classified as "Lee West" type[19] satisfying certain quality requirements are used, and only clusters from the LAr calorimeter and SPACAL are considered.

The presence of noise in the calorimeters can fake particles and so noise *suppression*

[1]The Central Inner z Chamber (CIZ) was removed during the HERA luminosity upgrade to make way for the new Central Inner Proportional Chamber (CIP2K). Refer to [27] for changes made to the H1 detector during the upgrade. See also Figure 2.8.

[2]For a full discussion on the reconstruction of the hadronic final state, refer to *An energy flow algorithm for Hadronic Reconstruction in OO: Hadroo2* [19].

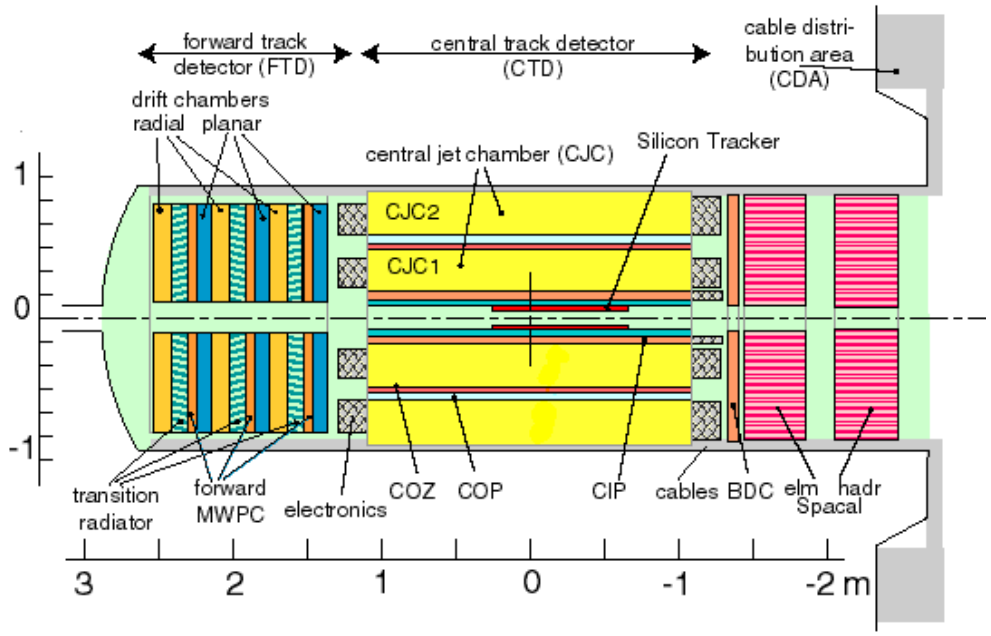

Figure 2.7: *The H1 tracking system: The central track detector (CTD) and the forward track detector (FTD). The CTD is composed of the central jet chambers (CJC1 and CJC2), the Z-chambers (CIZ and COZ) and the silicon tracker. The multiwire proportional chamber (CIP) is used for triggering.*

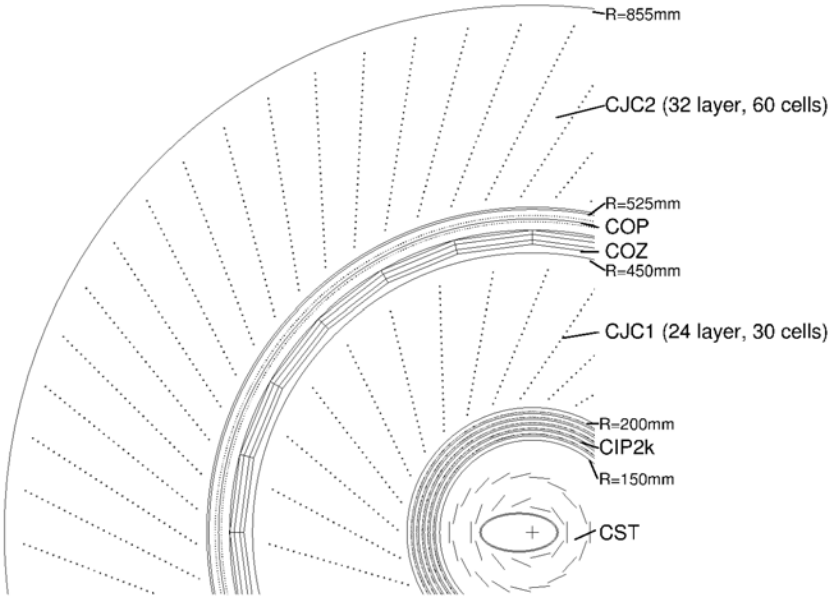

Figure 2.8: *The $r\phi$ view of the upgraded H1 tracker. See [27] for a list of the changes made.*

is vital in reconstructing the HFS[3]. Typically noise may amount to a few GeV per event and is non-negligable. Noise is attributed as having either an electrical origin or non-*ep* physics origin such as clusters caused by cosmics. Several algorithms reject noisy clusters on the basis of their isolation and topology (e.g. a narrow energy deposit parallel to the z-axis characteristic of a halo muon).

Charged particles can be reconstructed using either the track or the cluster. A decision then has to be made on whether the track or the corresponding cluster should be used to reconstruct the particle. The choice depends on the energy and its resolution of each method of reconstruction. If for example the track is chosen, an amount of energy in the cluster is supressed to remove double counting. Else the cluster is used and the track information is supressed.

Once all the tracks have been considered, particle candidates are made out of the remaining clusters. The hadronic final state is then the ensemble of all particle candidates that result, apart from the scattered electron.

2.5 Triggering

The majority of the events that are seen by the H1 detector come from non-*ep* interactions (see *Section* 5.5) which outnumber *ep* interactions by a factor of $\approx 10^4$ [15]. The high rate of background coupled with a high bunch crossing rate of 10.4 MHz requires fast decisions on whether to keep or reject an event, since a complete detector readout of an event necessarily involves dead-time[4]. The goal of the H1 trigger system therefore is to separate out interesting *ep* physics events while keeping dead-time to a minimum.

In order to achieve this aim, carefully selected trigger signatures are defined. Since some trigger decisions are more elaborate and hence more time consuming than others, the trigger system is sequenced into several levels which together form the pipeline, illustrated in Figure 2.9. The further the event progresses down the pipeline, the more time is allowed to make a decision (since there are much less events to process) and the decisions become more complex. Finally, events that make it through the pipeline get classified into certain physics classes (such as High Q^2 or Diffraction) and written to a Data Summary Tape (DST) where physics analyses can begin.

Regarding L1, the subdetectors send information to the Central Trigger Logic (CTL) in the form of *trigger elements* (TE). The CTL combines these trigger elements into a physics subtrigger (ST). If any of the physics subtrigger is satisfied the event progresses

[3]For a full discussion on the reconstruction of the hadronic final state, refer to *An energy flow algorithm for Hadronic Reconstruction in OO: Hadroo2* [19].

[4]Dead-time refers to time for which the detector is effectively "blind".

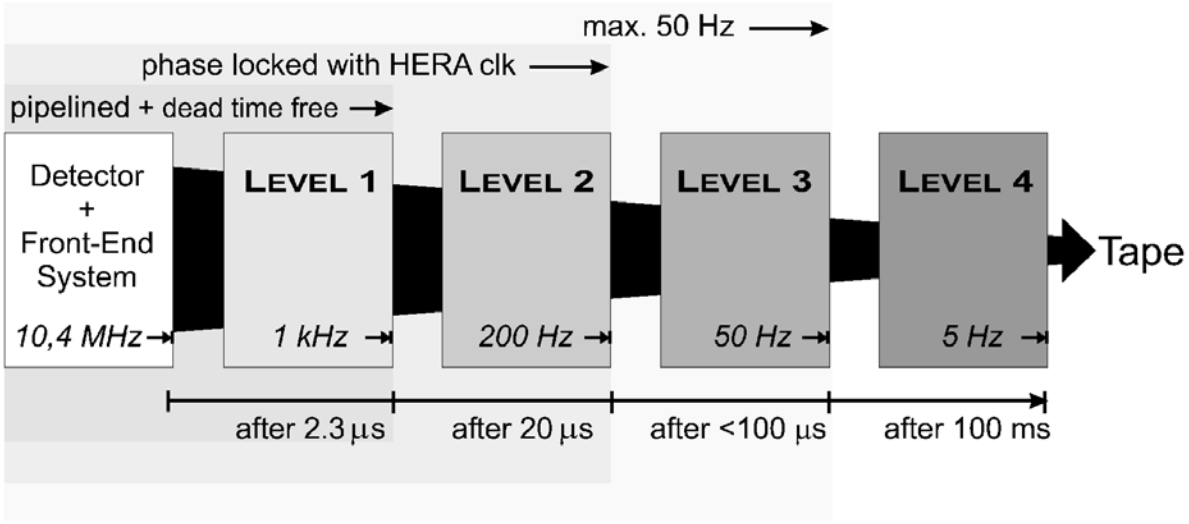

Figure 2.9: *A schematic view of the trigger levels. The input and output rates as well as the time limit of every trigger level are illustrated. The first level trigger (L1, FLT) must come to a trigger decision within 2.3 µs. It reduces the input rate of 10.4 MHz to ≈ 1 kHz. Clear non-ep events are rejected in an early stage of the trigger. If for example the second level trigger L2 decides to reject the event currently being read out, then the readout ceases.*

down the pipeline. The following pages outline the trigger elements used to make the L1 trigger decision for subtriggers ST67 and ST77, the subtriggers used in this analysis.

The LAr-based Trigger Elements

For the purpose of triggering, 16 neighbouring cells of the LAr calorimeter are grouped together into Trigger Cells (TCs) [12]. These TCs are further grouped into Trigger Towers (TTs). The analog signal of the trigger towers are summed and then digitized using FADCs (flash analog to digital converter). These FADCs are then summed into Big Towers (BTs), of which there are 14 in θ and 16 in ϕ, Figure 2.10. Several thresholds are introduced to suppress electronic noise and background: the AGM-threshold for the sum of the analog signals and the BT-threshold for summing the digitized signals into BTs.

The TEs used in this analysis are described below:

- **LAr_electron_1**: This TE fires if the energy deposited in one of the BTs exceeds a certain threshold. The threshold is set to ≈ 5 GeV in the CB and FB regions, and increases in the forward direction to ≈ 25 GeV due to the large amount of beam induced background present.

- **LAr_Etmiss**: This TE fires if the missing transverse energy calculated from the BTs

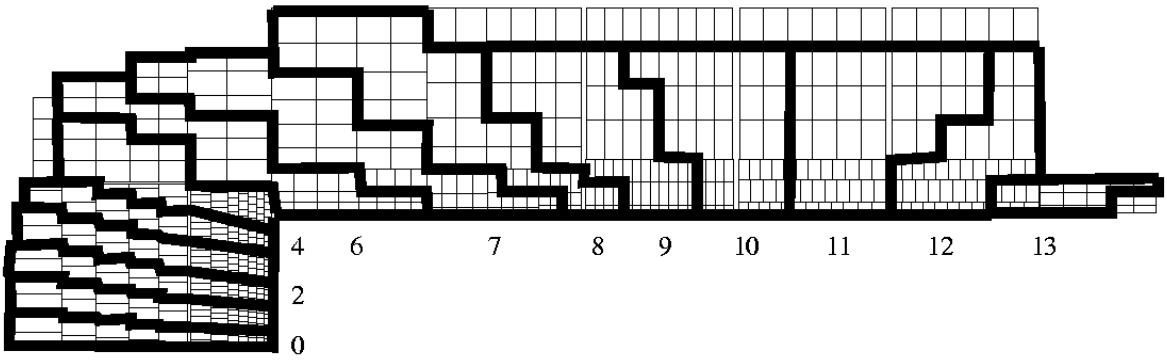

Figure 2.10: *Definition of the Big Towers (BTs) in the Liquid Argon Calorimeter.*

exceeds threshold. The missing transverse energy is $\sqrt{(\sum_{BT} E_{BT,x})^2 + (\sum_{BT} E_{BT,y})^2}$. Although this TE is based on *missing* transverse energy, it still provides an efficient NC trigger for in the case where an electron energy exceeds the dynamic range of the FADC this is interpreted as missing energy.

- **LAr_T0**: The LAr_T0 provides a timing signal which is determined from the trigger tower signals. The signal of the trigger tower is copied with 500 ns delay. The crossing point of the delayed signal with the original signal determines the trigger tower T_0. These are combined into the big tower T_0. LAr_T0 fires if a signal in at least one TT exceeds T_0 threshold.

The CIP-based Trigger Elements

CIP_mul: CIP_mul is set to a value depending on the sum of the number of tracks counted by CIP in the backward, central and forward regions. The TE CIP_mul is used with several thresholds.

CIP_sig==0: CIP_sig is set to a value depending on the ratio of central to non-central (backward plus forward) tracks.

CIP_T0, CIP_T0_nextbc: An important function of the CIP is to provide a timing signal, used as a reference for other subdetectors, especially the drift chambers. The trigger system is well suited to decide in which bunch crossing the event occured. CIP_T0 is asserted as 1 if at least one track is seen in the central region. Additionally, the same T0 signal is given one bunch crossing earlier in the form of the CIP_T0_nextbc TE. If a trigger comes at the same time as the CIP_T0_nextbc, it has the wrong timing and can

be rejected. Instead, it will be recorded in the following bunch crossing, as long as it is still active.

The Time-of-Flight(ToF)-based Trigger Elements

The ToF system consists of three scintillators at different positions along the beam pipe; z = -275 cm corresponds to the backward ToF (BToF). In addition there are two scintillator walls ("Veto Wall") at z = -810 cm and z = -650 cm. The trigger elements VETO_BG, BToF_BG and SToF_BG are used to reject events that arrive out of time based on the respective scintillators' (and SPACAL, SToF) timing. Also used are the FIT_IA and FIT_BG TEs which are based on forward interaction timing.

The subtriggers ST67 and ST77 use the trigger elements mentioned above in various combinations. Just as an example, one definition each of the ST67 and ST77 trigger condition are given below (the exact definition changes from time to time depending on background conditions):

ST67 Definition
Run : 372718 Date : 21/02/04
L1:(LAr_electron_1)&&
(!VETO_BG&&!BToF_BG&&!SToF_BG)&&
(CIP_T0||(LAr_T0&&!CIP_T0_nextbc))&&
(FIT_IA||!FIT_BG)&&(!(CIP_mul>7&&CIP_sig==0))

ST77 Definition
Run : 367258 Date : 02/01/04
(LAr_Etmiss>1)&&
(!BToF_BG&&!SToF_BG)&&
(CIP_T0)&&
(FIT_IA||!FIT_BG)&&
(!(CIP_mul==7&&CIP_sig==0)).

Chapter 3

Simulation

To correct for effects resulting from geometrical acceptance, inefficiency and resolution requires a firm understanding of the detector. To correct for radiative effects requires a firm understanding of physics. This knowledge is expressed in the form of a Monte Carlo (MC) simulation, an indispensable tool used in high energy physics.

3.1 Monte Carlo Simulations

It is difficult to claim to have a thorough understanding of a detector without first using a detector simulation. For example, the energy resolution of the scattered electron cannot be known using only data, since the *true* energy is never known. Of course one can use an independent method which does not rely on the electromagnetic calorimeter to *compare* (see Section 6.4), and so check agreement, but it still does not give the real resolution. If the simulation however produces an electron enery distribution which is in good agreement with the data, then it can be inferred that the resolution of the simulation (which is known of course) is very close to the resolution of the real detector.

Detector simulations are also useful in understanding detector problems such as inefficient regions in the detector. For example, if the trigger efficiency in the data is significantly lower than the MC simulation for a particular physical region of the LAr calorimeter, but the MC and data agree otherwise, then this may give a clue to an underlying electrical problem within the detector. The simulated detector should be as true as possible to the real one, which would involve for example simulating cracks and dead material. In cases the simulated detector is better than the actual, the MC can be smeared or suppressed accordingly.

If it can be shown that the distributions of the simulated detector are in good agreement to those of the actual detector, then the real power of simulations can be exploited - the power to *correct*. Suppose in a particular bin of a given quantity, due to resolution effects,

events migrate out. The simulation can be used to give a measurement of what *fraction* migrated out. This fraction can be used for a correction. Using the correction, and the number of events that remained in the data, it is possible to deduce with a given accuracy the real number of events that belonged to the bin before the migration took place. In this way the simulation is used to correct for the effects of detector resolution. This is very useful when there are several efficiencies relevant to an analysis that are distributed in a complex manner.

Event generators are ambitious computer programs that use our best knowledge of physics to produce events with the final state completely defined. This by itself is no easy task, for in the ideal case, an ensemble of MC generated events would reproduce what would be found in nature. At the end of the MC generating process is a set of known particles with their four-momenta completely specified.

Just as detector simulation can correct for detector effects, so too can MC generators correct for *physics* effects. For example, it may be impossible to know if a particular event has initial state radiation and in what amount, even given a perfect detector. However, if the simulation has radiative effects built in, then the simulation can be used to make radiative corrections, because just as the migration rate was known in the previous example, so too the amplitudes of radiative events in the MC (assumed to be close to nature) are known. So, detector simulations if handled properly are indeed powerful.

One final note, a correction is just that, a correction. It is the physicist's assertion that *both* physics and simulation are understood well enough to make the correction to the data. The correction need not be perfect, since it is usually given with an estimated error, with which the sensitivity of the measurement to the size of the correction can be calculated.

3.2 Generators

Signal Generator

DIS events are generated using the DJANGO program [9] which includes electroweak corrections of $\mathcal{O}(\alpha)$ and in which the following programs are integrated. The cross section is generated using HERACLES [17]. The events generated by HERACLES are completely described by the flavour of the scattering quark and the four-momenta of the final electron, final quark and potentially radiated photon. Regarding QCD dynamics the program LEPTO [16] is used. Hadronization is modelled using the JETSET program package [24] which uses parameters derived form e^+e^- scattering, assumed to be the same in DIS.

The events are generated using the MRSH[18] parton density functions (PDF) and then reweighted according to H1 PDF2000 Fit (see *Section* 1.3).

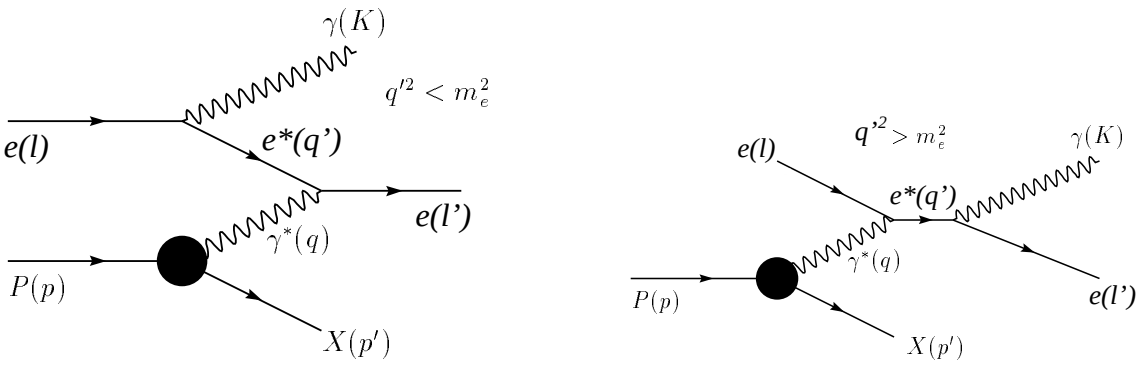

(a) **(b)**

Figure 3.1: *Feynman diagrams of the QED Compton process, (a) and (b). Here K and q′ are the four-momenta of the radiated photon γ and virtual electron e^* respectively.*

Background Generators

The main sources of *ep* background are outlined below, together with their MC generators:

- **Photoproduction (γp)**: In photoproduction ($ep \to eX$), $Q^2 < 0.01$ GeV^2 so that the exchanged photon is quasi-real[3]. Thus the electron is scattered through such a small angle that it escapes the main detector. Photoproduction is the most significant *ep* background contributor due to the size of the cross section, $\sim$ 165,000 nb and fakes the NC signal when a final state particle (or set of particles) is misidentified as an electron in the LAr. In this analysis direct, resolved and prompt photoproduction are simulated using the PYTHIA generator [23].

- **Low Q^2 DIS events**: If $Q^2 \lesssim 60$ GeV^2 the scattered electron will end up in the SPACAL, however particles in the final state may fake the electron signature in the LAr. The cross section due to low Q^2 DIS is much less than photoproduction (due to the $1/Q^4$ dependence) and is taken into account in the error attributed to *ep* background (see Section 6.4).

- **Elastic QED Compton**: The Feynman diagrams that contribute to the QED Compton cross section ($ep \to ep\gamma$) is shown in Figure 3.1. If the negative four-momentum transfer squared ($-q^2$) of the virtual photon $\gamma*$ is small, and that of the virtual electron $e*$ is relatively large in magnitude ($|q'^2|$), then the scattered electron can end up in the LAr calorimeter, making the event appear as a high Q^2 event. Elastic QED Compton is simulated using the WABGEN generator.

  The *inelastic* part of the QED Compton cross section is however counted as signal.

- **Lepton pair production (l^+l^-)**: In lepton pair-production ($ep \rightarrow eXl^+l^-$) the final state has a lepton pair l^+l^- where l is an electron, muon or tauon. The background contribution to the sample is estimated using GRAPE-Dilepton MC [2]. GRAPE-Dilepton implements pair-production using contributions of both photons and Z^0s.

3.3 Detector Simulation

The response of the detector to the generated particles is simulated by the H1SIM-package which is based on the GEANT-program [11]. The parameters used by this program were determined in test beam measurements and optimized during *ep* data taking. For energy response of the calorimeters, a fast parametrization for the development of electromagnetic and hadronic showers is used. Both data and simulated events are then subject to the same reconstruction program (H1REC) and the same analysis chain.

Chapter 4

Kinematic Reconstruction

Several methods of reconstructing the kinematics of high Q^2 NC events are available at the H1 detector since both the scattered electron and hadronic final state are measured. This chapter discusses the different methods, and explains why the e-Σ method is chosen for this analysis.

The two most important contributions to the NC cross section that need to be considered when reconstructing the kinematics are the leading order (LO) and initial state radiation (ISR, see *Section* 6.3) contributions. The corresponding Feynmann diagrams are repeated below, Figure 4.1.

For $Q^2 \gtrsim 1$ GeV^2, both the scattered electron e' and hadronic final state X are reconstructed in the detector, and so the kinematics of the leading order process is overdetermined, since only two final state measurements (excluding ϕ) are needed. The *extra* measurements are useful in reducing resolution effects as well as correcting for influences of higher order processes by using a combination of the measured quantities. The most common reconstruction methods[1] are the electron method (e-method), hadron method (h-method) and sigma method (Σ-method).

The **e-method** assumes that the process took place at leading order. Thus the kinematics of the event can be reconstructed solely from the scattered electron's energy $E_{e'}$ and angle $\theta_{e'}$. The reconstructed quantities are:

$$Q_e^2 \cong 4E_e E_{e'}(1+\cos\theta_{e'}), \qquad y_e \cong \frac{(2E_e - \Sigma_{e'})}{2E_e} \quad \text{and} \quad x_e \cong \frac{Q_e^2}{s y_e}$$

where: $\Sigma_{e'} = E_{e'}(1 - \cos\theta_{e'})$.(4.1)

[1]The double angle method is mainly used to calibrate the calorimeters (see *Section* 6.4) and is not considered here.

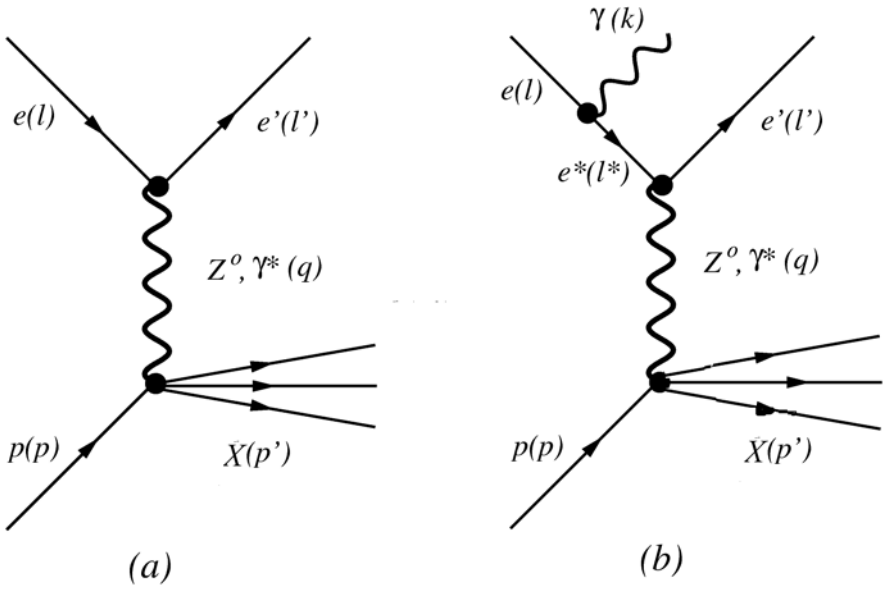

Figure 4.1: *Feynman diagrams for (a) leading order and (b) initial state radiative neutral current scattering. The quantities in parenthesis are the corresponding four-vectors.*

In the case where the process actually had initial state radiation, Figure 4.1, then the *mismeasurement* of Q^2, x and y (the kinematic variables at the Born level where the hard interaction occurs) are given by:

$$\frac{Q_e^2 - Q^2}{Q^2} = (1-z)(\frac{1}{z}), \qquad \frac{y_e - y}{y} = (1-z)(\frac{1}{y} - 1) \quad \text{and} \quad \frac{x_e - x}{x} = -(1-z)(\frac{1}{y} - 1) \quad (4.2)$$

assuming that the radiated photon γ is emitted in the direction of the beam lepton[2]. Here z is the fraction of energy remaining after the beam lepton emits the photon, that is:

$$z \equiv \frac{E_e - E_\gamma}{E_e}.$$

Under this assumption then, the e-method overestimates Q^2 and underestimates x. Figure 4.2 shows the change in the means $\langle (Q_e^2 - Q_{gen}^2)/Q_{gen}^2 \rangle$ and $\langle (x_e - x_{gen})/x_{gen} \rangle$ *after* ISR is switched on for signal MC events[3]. As can be observed for the e-method, $\langle (Q_e^2 - Q_{gen}^2)/Q_{gen}^2 \rangle$ increases and $\langle (x_e - x_{gen})/x_{gen} \rangle$ decreases. The large drop in the x measurement at low y is due to the $1/y$ term in equation 4.2.

The resolution of Q_e^2 , $\sigma(Q_e^2)$ due to the detector smearing of the energy and polar

[2]This is a fair assumption owing to the singularity of the matrix element as $(l^*)^2 \to m_e^2$.
[3]The subscript "gen" refers to the generated quantities at the Born level in the MC.

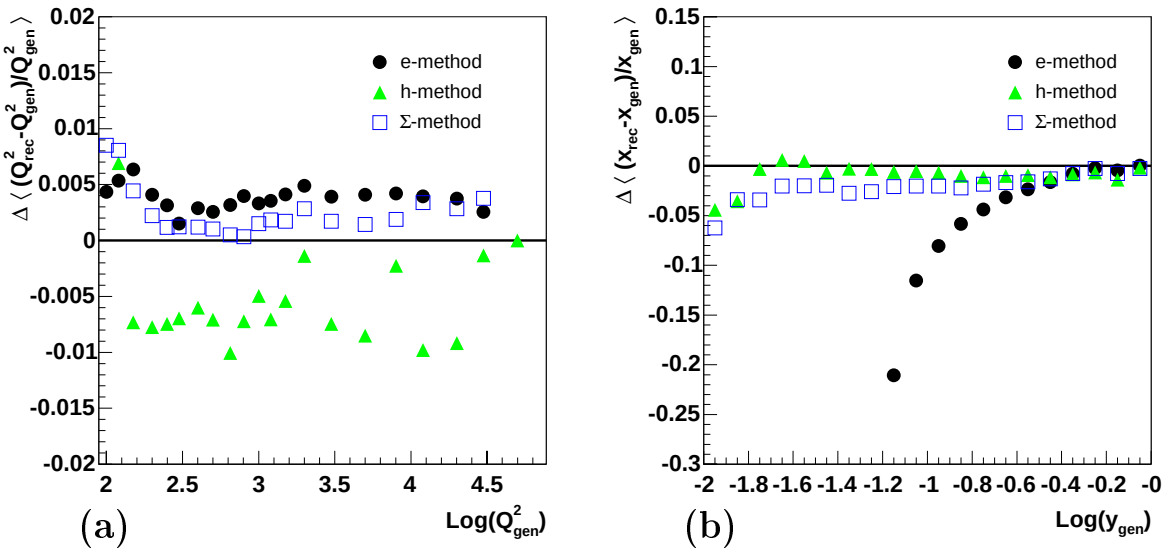

Figure 4.2: *The change Δ of the means (a) $\langle(Q^2_{rec}-Q^2_{gen})/Q^2_{gen}\rangle$ and (b) $\langle(x_{rec}-x_{gen})/x_{gen}\rangle$ after initial state radiation is switched on. The three reconstruction methods discussed are shown. See Appendix B for resolution plots.*

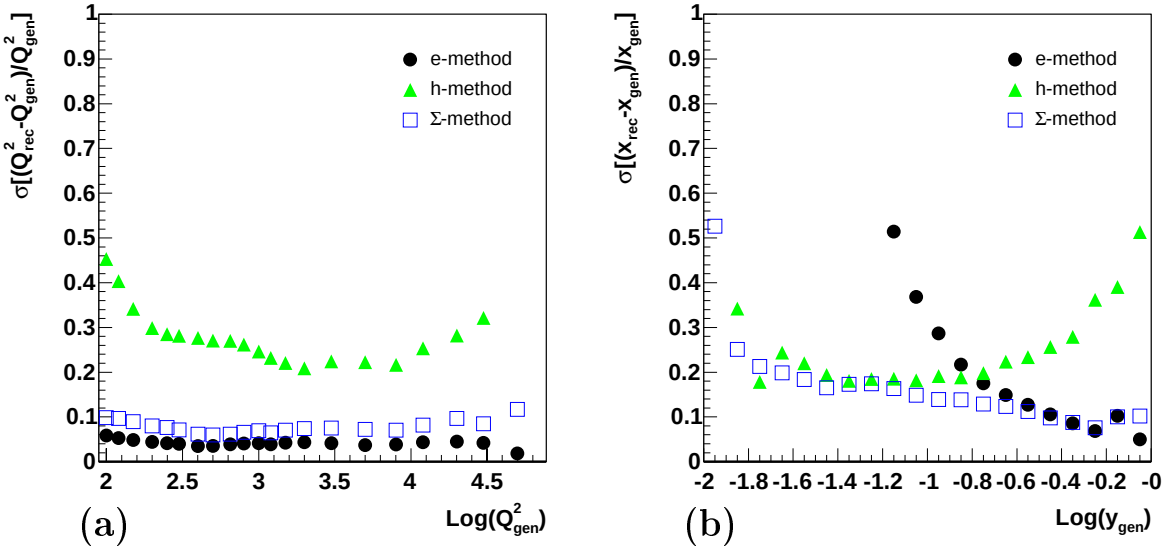

Figure 4.3: *The width σ of the reconstructed kinematic quantities for the three reconstruction methods, (a) for Q^2 and (b) for x versus Log(y_{gen}). See Appendix B for resolution plots.*

angle measurement is given by:

$$\frac{\sigma(Q_e^2)}{Q_e^2} = \frac{\sigma(E_{e'})}{E_{e'}} \oplus \frac{\sin\theta_{e'}}{1+\cos\theta_{e'}}\sigma(\theta_{e'}) \tag{4.3}$$

where $\sigma(E_{e'})$ and $\sigma(\theta_{e'})$ are the resolutions of the energy and polar angle measurement respectively and $a \oplus b \equiv \sqrt{a^2+b^2}$. The resolution σ of Q_e^2 relative to Q^2 generated is shown in Figure 4.3(a). The precision of the energy and polar angle (*Section 6.4*) measurement allows Q_e^2 to have an excellent resolution ($\approx 5\%$) over the full kinematic range.

The resolution of x_e and y_e can be expressed as:

$$\frac{\sigma(y_e)}{y_e} = \frac{\sigma(\Sigma_{e'})}{2E_e - E_{e'}} \left(= \frac{\sigma(\Sigma_{e'})}{2E_e y_e} \right) \tag{4.4}$$

$$\frac{\sigma(x_e)}{x_e} = \frac{\sigma(Q_e^2)}{Q_e^2} \oplus \frac{\sigma(y_e)}{y_e}. \tag{4.5}$$

For large values of $\Sigma_{e'}$ (or equivalently, low values of y_e) the resolution of both y_e and x_e degrade significantly due to the $1/y_e$ term in equation 4.4. This can be seen in Figure 4.3(b) where σ increases as y drops.

The **Jacquet-Blondel method**[13] or **h-method** also assumes that the process took place at leading order, however the measurements are taken from the hadronic final state. The quantities Σ_h and P_{th} are reconstructed as:

$$\Sigma_h = \sum_i (E_i - p_{zi}) \qquad \text{and} \qquad P_{th} = \sqrt{(\sum_i p_{xi})^2 + (\sum_i p_{yi})^2}. \tag{4.6}$$

Here E_i, p_{xi}, p_{yi} and p_{zi} are the energy and momentum components of the ith particle reconstructed; i runs over all particles except the scattered electron. Particle masses are ignored. With this in mind the reconstructed kinematic variables Q_h^2 , y_h and x_h are given by:

$$y_h \cong \frac{\Sigma_h}{2E_e}, \qquad Q_h^2 \cong \frac{p_{th}^2}{1-y_h} \quad \text{and} \quad x_h \cong \frac{Q_h^2}{s y_h}. \tag{4.7}$$

Figure 4.3(a) shows the poor resolution of Q_h^2 . The h-method is only used in charged current analyses, where there is no alternative but to use the hadronic final state as the neutrino leaves undetected.

Unlike the first two methods, the **Σ-method** assumes that the process which took place had initial state radiation, and that the photon was radiated in the direction of the incoming lepton. This extra condition requires one extra variable, and this is taken

as the longitudinal momentum of the hadronic final state Σ_h. The kinematics are now reconstructed as:

$$y_\Sigma \cong \frac{\Sigma_h}{\Sigma_h + \Sigma_{e'}}, \qquad Q^2_\Sigma \cong \frac{(E_{e'} \sin\theta_{e'})^2}{1 - y_\Sigma} \quad \text{and} \quad x_\Sigma \cong \frac{Q^2_\Sigma}{s y_\Sigma}. \tag{4.8}$$

Figure 4.2 shows that when ISR is applied, there is very little change in $\langle (Q^2_\Sigma - Q^2_{gen})/Q^2_{gen} \rangle$ and $\langle (x_\Sigma - x_{gen})/x_{gen} \rangle$. This is because the radiated photon is taken into account in the reconstruction.

The resolution of y_Σ is given by:

$$\frac{\sigma(y_\Sigma)}{y_\Sigma} = \frac{\sigma(\Sigma_{e'})}{\Sigma_{e'} + \Sigma_h} \oplus \frac{\Sigma_{e'}}{\Sigma_{e'} + \Sigma_h} \left(\frac{\sigma(\Sigma_h)}{\Sigma_h} \right). \tag{4.9}$$

The resolution of y_Σ is significantly better than y_e at low y values since the term due to $\sigma(\Sigma_{e'})$ is now effectively *reduced* by $\Sigma_{e'} + \Sigma_h$ (compare equation 4.4 with equation 4.9). This produces a substantial improvement in the resolution of x_Σ compared to x_e as seen in Figure 4.3(b).

In this analysis, Q^2 is reconstructed using the e-method, and x is reconstructed using the Σ-method. Together this is called the **e-Σ method** of reconstruction. That is:

$$Q^2_{e\Sigma} = Q^2_e, \qquad x_{e\Sigma} = x_\Sigma \quad \text{and} \quad y_{e\Sigma} = \frac{Q^2_e}{s x_\Sigma}. \tag{4.10}$$

Chapter 5

Event Selection

Resolving signal from background events requires an understanding of the various types of processes involved, as well as the detector response to these processes. This chapter lays out in a step by step fashion the method used to reduce an inital sample of ≈ 2 *million events having a significant amount of background to the final sample made up of* $\approx$ *135,700 events rich with signal. An estimate of the amount of background present in the final sample is also given.*

5.1 Run Selection

Not all events that are written to tape represent ep interactions. Of those that do, many are not high Q^2 NC events. The first step in filtering out the signal from tape is to select runs where at least the essential sub-detectors required in the analysis are active. Specifically these are the central jet chambers (CJC1 and CJC2), central inner proportional chamber (CIP), LAr and SPACAL calorimeters, luminosity system and time of flight system (ToF). Runs are also rejected if the relevant physics subtriggers ST67 and ST77 are disabled.

The run selection was made for the dataset corresponding to the period September 3rd 2003 to August 4th, 2004. The interacting leptons are exclusively positrons, e^+, and the time interval covers both left and right handed helicities. This selection resulted in an integrated luminosity $\mathcal{L}$ of 47.4 pb^{-1} and an average polarization[1] of $-0.9\% \pm 0.3 \pm 0.8$, $\simeq 0$ within error. Hence the cross section measured in this analysis corresponds to the unpolarized NC cross section. Figure 5.1 shows the integrated luminosity as a function of polarization; the left and right handed running periods are clearly distinguishable.

[1] Polarization is measured in the range -100 to 100%.

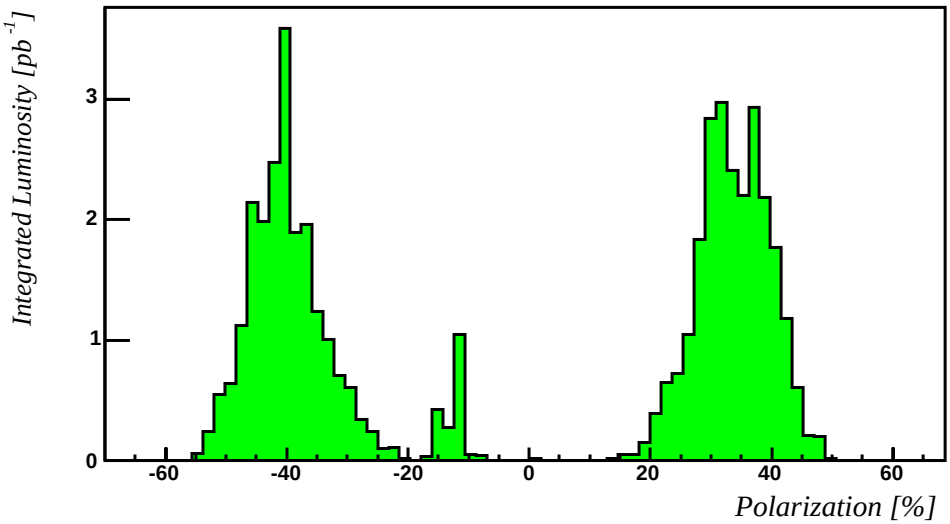

Figure 5.1: *Integrated Luminosity as a function of Polarization.*

5.2 Event Signature - High Energy Deposit in LAr Electromagnetic Calorimeter

With the required sub-detectors on, events can be reconstructed. Figure 5.2 is a computer generated image of a signal event; the electron enters the detector from the left, the proton from the right. The reconstructed vertex V corresponds to the *ep* interaction point. The scattered electron traverses the central jet chambers leaving a track T. It then enters the LAr electromagnetic calorimeter where it produces a high energy deposit C. This energy deposit can be regarded as the signature of the signal, and provides the basis for triggering.

The subtrigger ST67 uses the trigger element LAr_electron_1 to identify events with high energy deposits in the calorimeter towers (see *Section* 2.5). The efficiency of the LAr_electron_1 trigger element ϵ_{LAREL1} as a function of the impact position of the scattered electron on the surface of the LAr calorimeter is useful in identifying physical regions of the detector in which the trigger element and hence the trigger efficiency is comparatively low. The impact position is calculated using a helix trajectory with input parameters of reconstructed z-vertex position, energy and polar angle (taken from the calorimeter), phi (taken from the track) and the calorimeter geometry. The z-coordinate and azimuthal angle of the impact position are denoted by z_i and ϕ_i repectively. The regions of the detector not consistent with 100% efficiency are shown shaded in Figure 5.3 and are removed from the analysis; the so called *fiducial volume cut*[2].

[2]The fiducial volume cut was obtained from the nELAN Group, and represents the best available

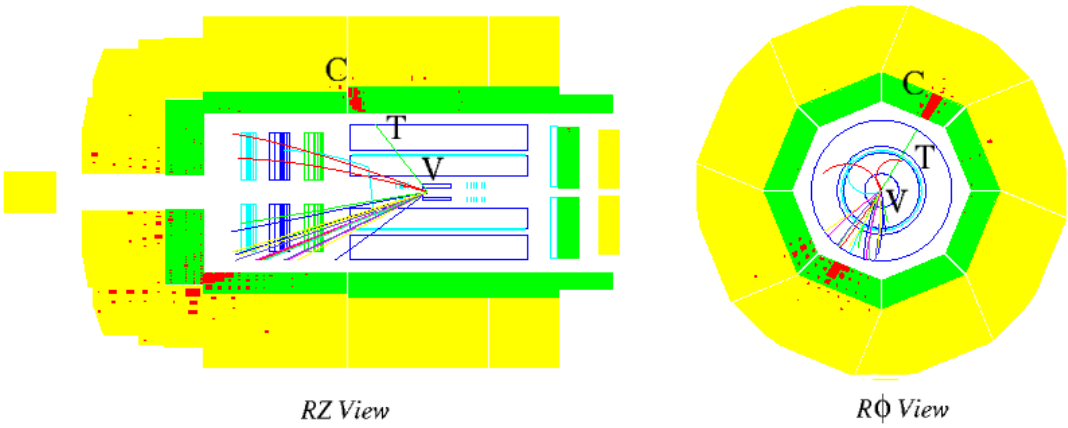

Figure 5.2: *Visual display of a signal event.*

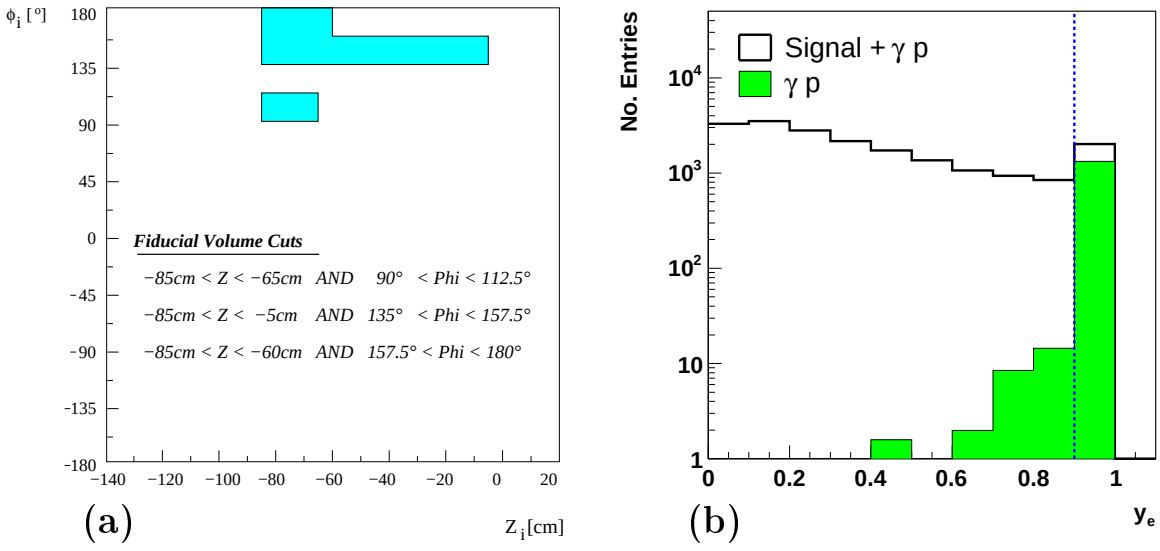

Figure 5.3: *(a)Fiducial volume cut (shaded) based on inefficency of the LAr_electron_1 trigger element. (b)Distribution of y_e for signal MC and γp MC.*

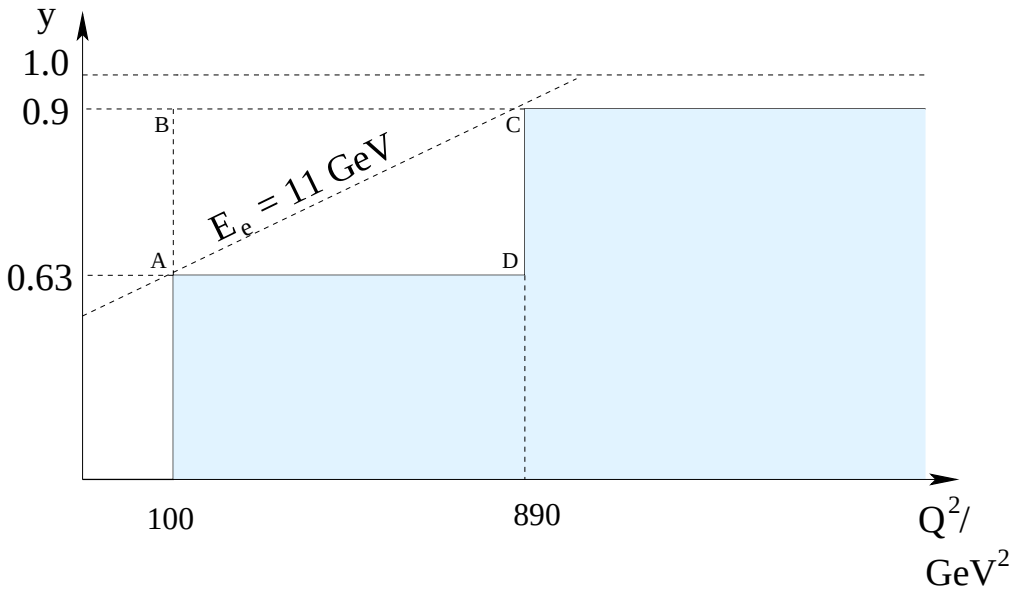

Figure 5.4: *Kinematic cuts on Q^2 and y (not to scale).*

Range of Q^2 /GeV^2	y_{max}
$0 < Q^2 < 100$	0
$100 < Q^2 < 890$	0.63
$890 < Q^2 < s$	0.9

Table 5.1: *Cut on y for different Q^2 ranges.*

As a function of scattered electron energy, ϵ_{LAREL1} is expected to be 100% [15] for $E_{e'}$ greater than 11 GeV. Below 11 GeV the efficiency drops. This inefficient region is therefore effectively avoided by removing the kinematic region denoted by ABCD as shown in Figure 5.4. The cuts are made using Q^2 and y as determined from the electron method which has the best resolution in this kinematic region (see *Chapter* 4).

A further kinematic cut on Q^2 and y is made after considering the distribution of y_e using signal and γp MCs, shown in Figure 5.3 with the γp MC contribution highlighted (shaded). Since at values of $y_e > 0.9$ the photoproduction contribution dominates ($\approx$ 65%), this kinematic region is also removed from the analysis.

With the minimum Q^2 considered in this analysis chosen to be 100 GeV^2, the kinematic cuts are summarized in Table 5.1 and the corresponding kinematic region where the cross section is measured is shown shaded in Figure 5.4.

information at the time of the analysis.

Electron Finder

Many types of particles deposit energy in the electromagnetic calorimeter, not just electrons. Therefore an algorithm which is sensitive to the properties of an electron shower is used to identify electron candidates [7]. The algorithm used in this analysis is QECFWD [7] and uses the following procedure. An electron envelope is associated to a preselected calorimeter cluster which acts as a seed. The envelope takes the form of a 7.5° cone with axis defined by the line joining the barycenter of the seed to the interaction vertex. The tip of the cone is 1m away from the seed and the cone is truncated at the end of the first hadronic layer. Neighbouring clusters are merged to the seed if at least half of their energy falls inside the cone. This produces a cluster candidate. The cluster candidate is then tested for compactness and isolation using estimators based on its size, shape and position in the detector. The cluster candidate must also meet minimum energy and P_t requirements of 5 GeV and 3 GeV/c respectively. Having survived all the required cuts, the cluster candidate is then classified as an electron candidate. The electron candidate with the highes P_t in the event is taken as the scattered electron.

The efficiency of identifying electrons ϵ_{ELEC} was calculated using an independent track-based electron finder. Thus:

$$\epsilon_{ELEC} = \frac{\text{No. of events found by calorimeter } \textbf{\textit{and}} \text{ track} - \text{based finder}}{\text{No. of events found by track} - \text{based finder}}$$

The efficiency as a function of the electron impact position is shown in Figures 5.5(a) and (b) for ϕ_{wheel}[3] and z_i respectively. It can be seen from Figure 5.5(a) that ϵ_{ELEC} drops in the region of the ϕ-cracks between the calorimeter wheels. As a function of z_i the efficiency also drops in MC at the z-crack between the calorimeter wheels CB2 and CB3 ($z_i \approx 20$ cm) situated just forward of the nominal interaction point. The statistical error in data is large. However, there is known to be large inefficiency [15] in these regions as the electron can pass through the electromagnetic part of the calorimeter without interacting after which it deposits its energy directly into the hadronic part; thus rendering it irrecognisable to the electron finder. Since there is also an energy dependence of ϵ_{ELEC} in these crack areas [15] and the energy resolution is significantly worse here compared to the other parts of the calorimeter [15], experimental control becomes difficult. The cracks are therefore avoided by cutting on ϕ_{wheel} and z_i as outlined in Table 5.2. The region $z_i < -190$ cm is also removed because of dropping efficiency and poor energy resolution due to leakage.

[3] ϕ_{wheel} is defined as the phi coordinate of the impact position relative to the phi-coordinate of the center of the ϕ-crack.

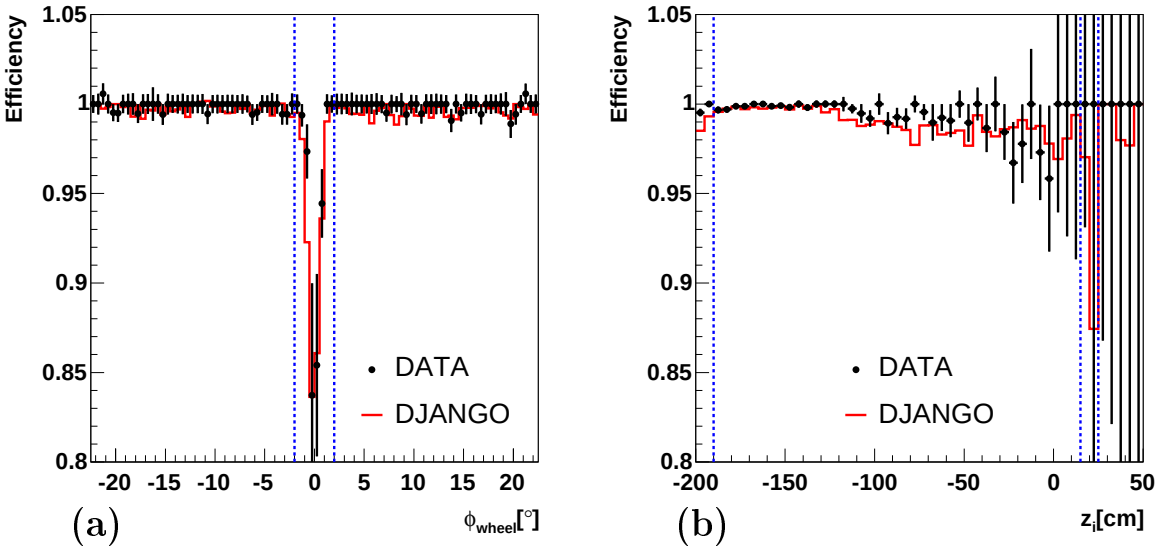

Figure 5.5: *Electron efficiency ϵ_{ELEC} as a function of (a) ϕ_{wheel} and (b) z_i .*

Electron Impact Position Removed from Analysis	Comments
$\phi_{wheel} \notin [-2°, +2°]$	ϕ-cracks
$15cm < z_i < 25cm$	z-crack between CB2 and CB3
$z_i < -190cm$	Very Backward Region of BBE

Table 5.2: *Cuts on Electron Impact Position.*

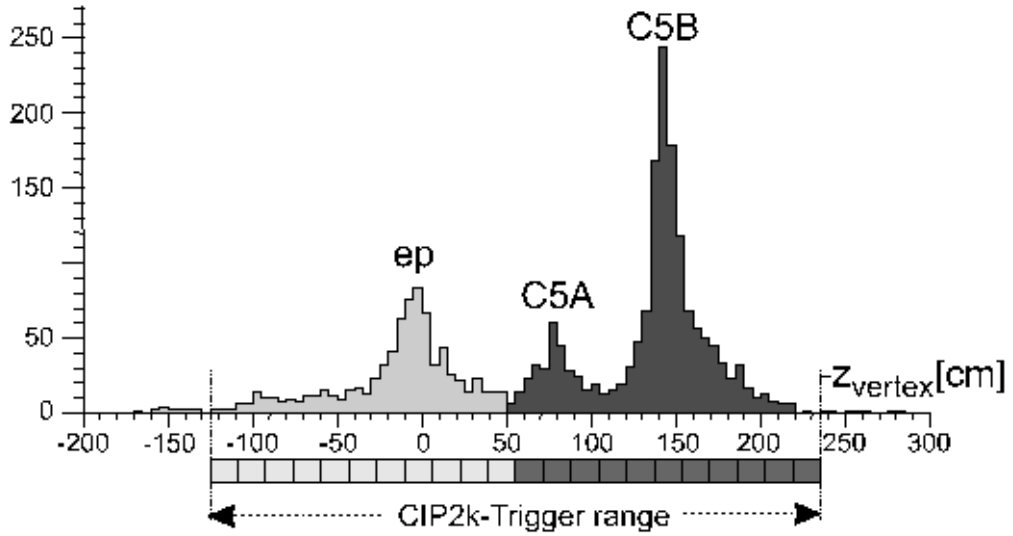

Figure 5.6: *Distribution of the reconstructed z-position of the interaction vertex (Z_{vtx}) for a luminosity run[27].*

5.3 Vertex & Track Link Requirement

Vertex Requirement and Efficiency

The Z_{vtx} distribution of reconstructed vertices for a particular luminosity run is shown in Figure 5.6[27]. Peaks appear at the nominal interaction point (corresponding to *ep* physics), as well as at the collimators C5A and C5B (corrseponding to secondary interactions between particles produced by beam-gas collisions and the collimator) which are used to reduce synchrotron radiation exposure of the H1 detector [27]. These secondary interactions constitute non *ep* background and are effectively reduced by the requirement of a reconstructed vertex close to the nominal interaction point. Thus a primary interaction vertex in the central part of the detector CV within 35cm of the mean Z_{vtx} must be satisfied by all events entering the final sample.

The efficiency with which the CV is reconstructed ϵ_{CV} was studied using a clean sample made by removing the vertex and track link requirements and tightening *ep* physics and DIS characteristics. Specifically the additional requirements are:

- Require[4] $0.6 < P_t^{bal} < 1.2$,
- Require $45 < E - P_z < 65$ GeV/c,

[4] P_t^{bal} is defined as the ratio between the P_t of the hadronic final state to that of the scattered electron: $P_t^{bal} \equiv P_{th}/P_{te'}$.

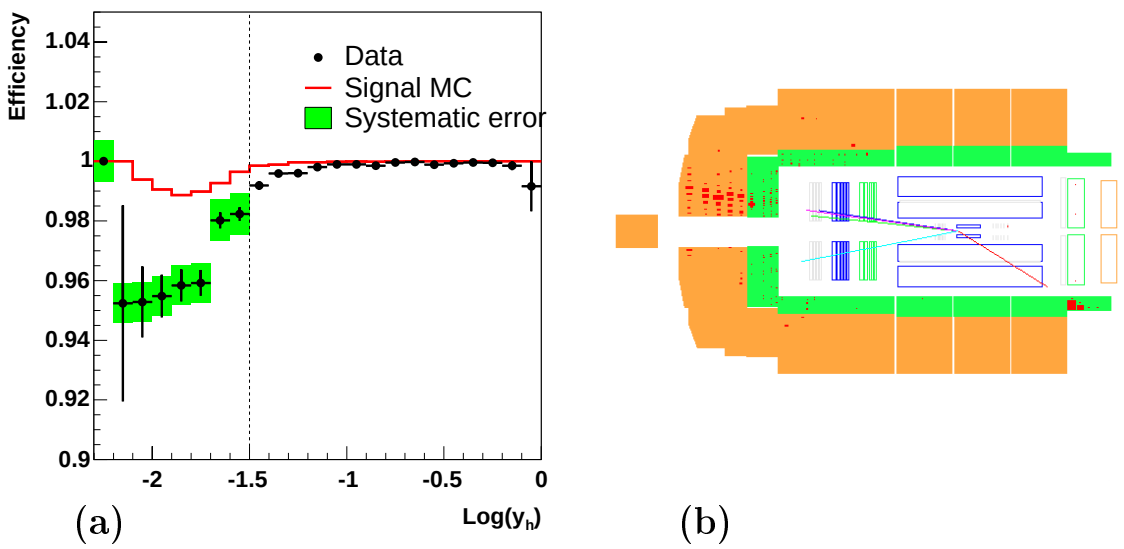

Figure 5.7: *(a) The central vertex efficiency ϵ_{CV} as a function of y_h. Also shown is the quoted systematic uncertainty $\Delta\epsilon_{CV}/\epsilon_{CV}$ = 0.7 % for the region log(y) < -1.5. For log(y) ≥ -1.5 the uncertainty in ϵ_{CV} is considered negligible. The disagreement between ϵ_{CV}^{DATA} and ϵ_{CV}^{MC} is corrected for in Section 5.3. (b) A low y_h event (Log(y_h) = -1.64).*

- Require $\eta_{max} > 3$,
- Require only one electromagnetic particle candidate in the event,
- Require verified physics subtriggers (ST67 or ST77).

Figure 5.7(a) shows ϵ_{CV} as a function of y_h, the inelasticity measured using the hadronic final state. It can be seen that the efficiency in both data and MC falls with y_h. At low y_h ($\lesssim 0.1$) the hadronic final state is scattered in the very forward direction and so there are less tracks in the central part of the detector from which the vertex can be reconstructed. One such event is shown in Figure 5.7(b). Events such as these can have a vertex reconstructed from the track of the scattered electron alone; it can be shown that the vertex efficiency drops if the quality of the reconstructed scattered electron track is poor.

Figure 5.7(a) also shows that MC efficiency is significantly higher than the efficiency in data for $\log(y_h) \lesssim -1$. A correction is therefore applied to the MC (see *Section* 5.3).

Track Link Requirement and Efficiency

Events entering the final sample are required to have a track *linked* to the scatterd electron candidate. This track-link reduces the possibility of a photon or neutral hadron (eg. π^0) faking the electron. The reconstructed track is also required to come from (or be near to) the central vertex, thus ensuring that the electron *did* come from an interaction in the central part of the detector.

The closeness of the track to the cluster is quantified by the quantity DCA (Distance of Closest Approach). Figure 5.8(a) shows the DCA plotted for signal and photoproduction MC (γp MC) events using the final selection criteria save the track link requirement. As can be seen, in signal events the DCA is peaked much closer to zero, while in photoproduction the distribution is almost flat. Thus DCA can be used to distinguish between scattered electrons from high Q^2 events, and final state particles from photoproduction that fake the scattered electron.

The shape of the DCA distributions in Figure 5.8(a) suggest that by increasing the maximum DCA allowed for a track to be considered linked to the cluster, the acceptance of both signal and photproduction background increases. Figure 5.8(b) shows the efficiency of linking a DTRA track (i.e. vertex fitted) for data, signal and photoproduction MC events for different cuts on DCA (The track linking efficiency was studied using the same clean sample used to calculate vertex efficiencies, but only with events having a vertex). As can be seen, the increase in ϵ_{DTRA} for both data and signal MC does not compare favourably with the corresponding increase for photoproduction when the DCA is increased beyond 12cm. Thus to have a high selection efficiency as well as to keep a handle on photoproduction background, the maximum allowed DCA for any track to be linked to the cluster was kept at 12cm. The DCA distribution of data and signal plus photoproduction MC is shown in Figure 5.8(c).

The efficiency of linking a DTRA track ϵ_{DTRA} as a function of the polar angle of the scattered $\theta_{e'}$ is shown in Figure 5.9(a). The efficiency falls as $\theta_{e'}$ departs from vertical. In the forward direction the efficiency drops below 85% in data (from an average of 94.55%) for $\theta_{e'}$ between 0° and 30°. This inefficiency is attributed to dead material at the end of the inner CJC which causes the electron to shower, and so track reconstruction is not optimum. To maintain a high efficiency in this high Q^2 region, no track link is required.

To further increase the track linking efficiency and reduce the disagreement between the efficiency in data and MC, non-vertex fitted (DTNV) tracks are used. The track is still required to be near the vertex, with a distance of not more than 5cm in the $r\phi$-plane. The same DCA requirement is applied as for DTRA tracks. The efficiency by which DTNV tracks are linked to the electron ϵ_{DTNV} providing no DTRAs can be linked is shown in Figure 5.9(b).

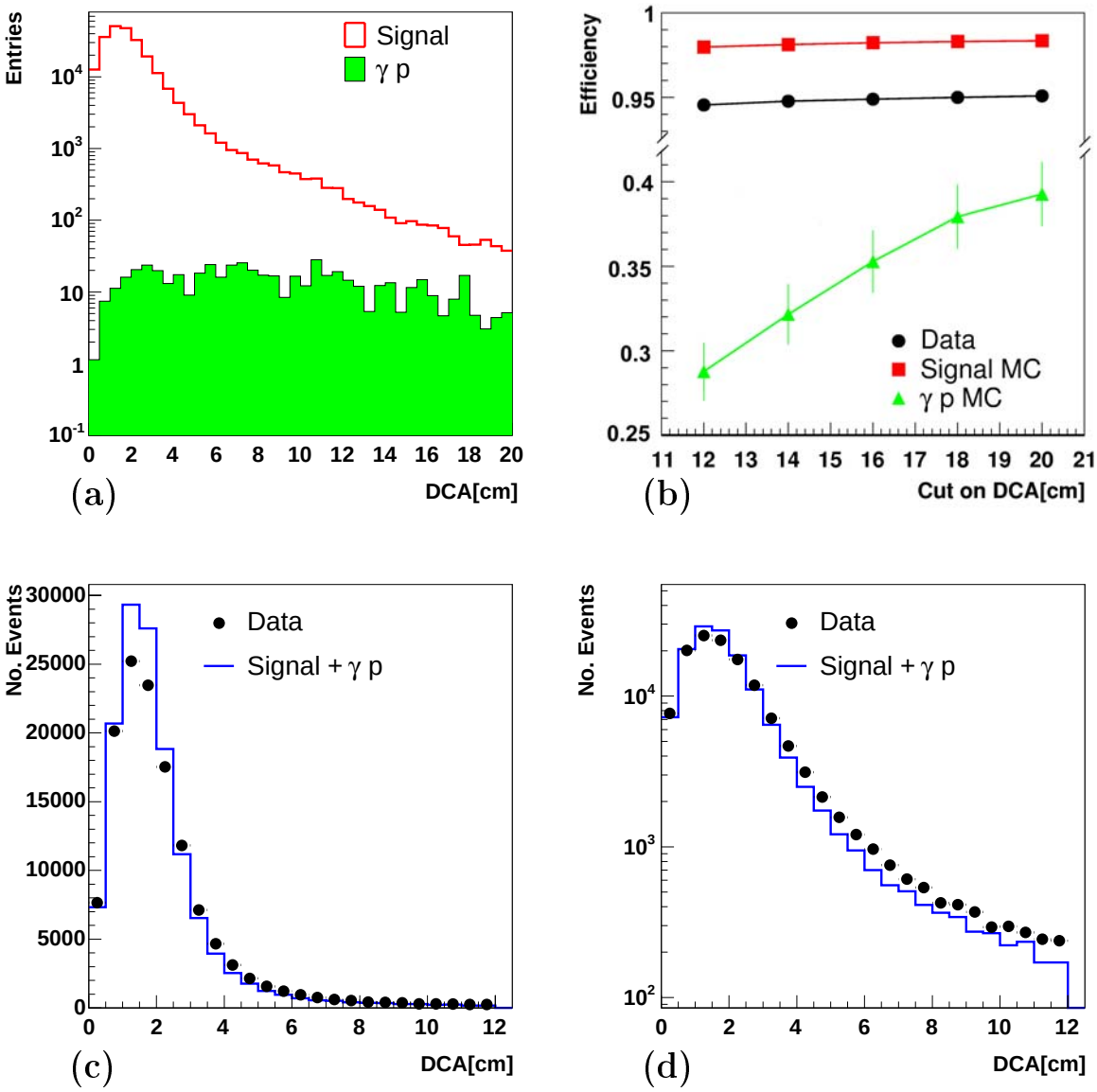

Figure 5.8: *(a)The DCA distribution of signal and photoproduction MC events. (b) The total DTRA efficiency ϵ_{DTRA} as a function of cut on the DCA. The DCA distribution for data and signal + photoproduction MCs in (c) linear and (d) log scale.*

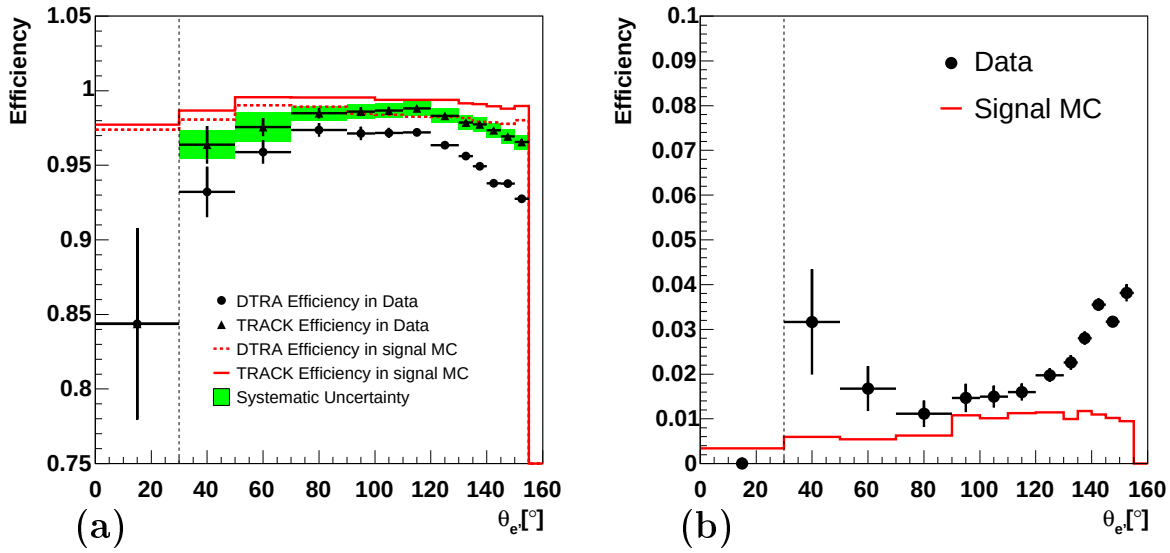

Figure 5.9: *(a)DTRA and Track efficiency and (b)DTNV efficiency as a function of* $\theta_{e'}$. *In (a) the quoted uncertainty of* ϵ_{TRACK} *is also shown.*

Range of $\theta_{e'}$ [°]	Track Link Requirement
$\theta_{e'} < 30$	No Track Required
$\theta_{e'} \geq 30$	DTRA with DCA $<$ 12cm
	OR
	DTNV 5cm from Vertex and with DCA $<$ 12cm

Table 5.3: *Final Track Linking Requirements.*

Finally ϵ_{TRACK} the efficiency of linking either a DTRA or DTNV is shown as a function of $\theta_{e'}$ in Figure 5.9(a) showing that there is less disagreement between data and MC when DTNV tracks are included in the track-linking criteria.

Table 5.3 summarizes the track linking requirement.

MC Correction

One can conclude that the MC tracker is more efficient than the actual tracker since it has a larger central vertex efficiency (Figure 5.7), larger track-linking efficiency (Figure 5.9) and as well produces tracks closer to the cluster candidates (Figure 5.8). That is, MC tracks are in general better than actual tracks. To correct for this a vertex efficiency correction factor f_{CV} is applied to MC events based on the elasticity y, and a track-linking correction factor f_{TRACK} is applied based on the scattered electron angle $\theta_{e'}$ of the MC

event. Here y and $\theta_{e'}$ refer to generator level quantities. f_{CV} is defined as:

$$f_{CV}(y) \equiv \frac{\epsilon_{CV}^{DATA}}{\epsilon_{CV}^{MC}}\Big|_{y} \tag{5.1}$$

and f_{TRACK} as

$$f_{TRACK}(\theta_{e'}) \equiv \frac{\epsilon_{TRACK}^{DATA}}{\epsilon_{TRACK}^{MC}}\Big|_{\theta_{e'}}. \tag{5.2}$$

$f_{TRACK}(\theta_{e'})$ is only applied for $\theta_{e'} > 30°$.

After correcting the MC efficiencies to match the data, systematic uncertainties are attributed to ϵ_{CV} and ϵ_{TRACK} as seen in Figures 5.7 and 5.9 and described in Section 6.4.

Z-Vertex Reweight

The z-position of beam interactions has a distribution that is run dependent. Hence it is not possible to know what Z_{vtx} distribution should be used to generate the MC until the final sample is selected. What *is* known from years of experience of running the collider is that the Z_{vtx} distribution of ep physics is approximately Gaussian in shape with mean close to the nominal interaction point and with width of approximately 11 cm. Therefore the MC is generated using a Gaussian Z_{vtx} distribution with mean 0 and width 13cm. It is then reweighted to match the distribution observed in data. A width of 13 cm is used so that more statistics can be obtained at the tails of the distribution.

Figure 5.10(a) shows the Z_{vtx} distribution in data, and the fit used to parametrize it. The assumption made is that the actual Z_{vtx} distribution of ep physics is made up of a sum of Gaussians. Therefore the fit comprises of three Gaussians $g_i(Z_{vtx})$, each with free parameters of mean μ_i, width σ_i and weight w_i; $i = 1, 2, 3$. The three Gaussian components are also presented to show their relative weights, means and widths. Figure 5.10(b) shows the Z_{vtx} distribution in signal MC before and after reweighting; also shown in log scale in Figure 5.10(c) to emphasize the tails. As can be seen, the distribution in MC agrees reasonably well with data after applying the reweight.

The maximum polar angle of the scattered electron that can be measured by the LAr electromagnetic calorimeter depends on the Z_{vtx} of the interaction; as Z_{vtx} increases, so does $\theta_{e'}^{max}$. That is, the angular acceptance is Z_{vtx} dependent. In this way, reweighting the Z_{vtx} *generated* by the MC directly influences the distribution of $\theta_{e'}$ *reconstructed* by the MC. Figure 5.10(d) shows the distribution of $\theta_{e'}^{MC}$ before and after Z_{vtx} reweighting for signal MC ; the distribution for data is also shown. As can be observed, there is better agreement between data and MC after reweight.

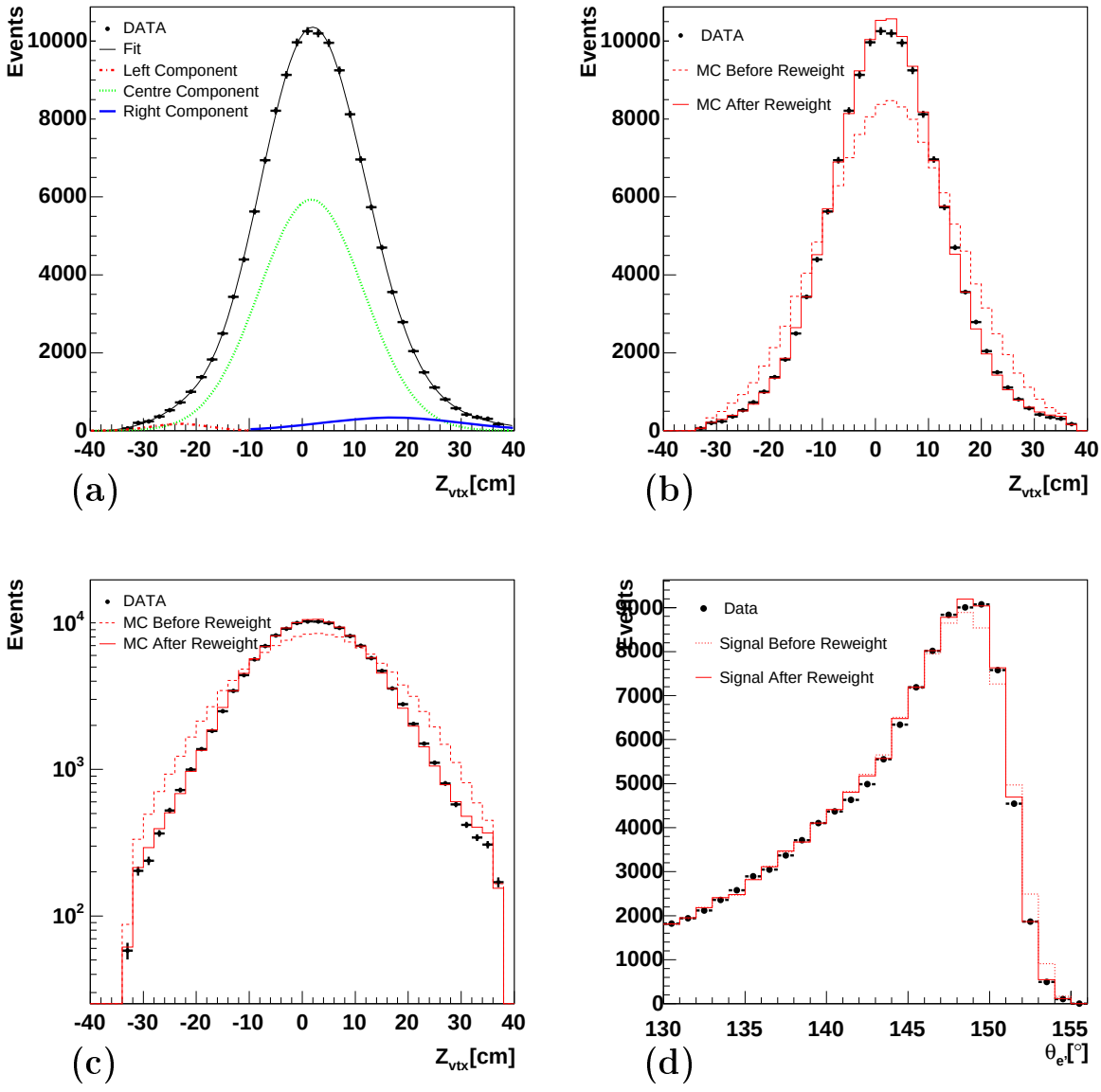

Figure 5.10: *(a) distribution of the data and the corresponding fit. (b)Z_{vtx} Distribution in data and signal MC before and after Z_{vtx} reweight and in (c) log scale. (d) $\theta_{e'}$ distribution before and after Z_{vtx} reweight.*

5.4 Initial State Radiation

Electron-proton interactions are often accompanied by Bremstrahlung processes where a photon is emitted from either the lepton or proton line (see *Section 6.3*). These processes skew the reconstruction of the event kinematics and so must be corrected for. The largest part of the correction is due to the emission of the photon from the incoming lepton, known as *Initial State Radiation* (ISR).

ISR photons are usually emitted in the direction of the incoming lepton (the negative z direction at H1), and so these events are usually characterised by missing longitudinal momentum, $(E-P_z)^{miss}$ $(= 2E_e - (E-P_z))$ as the photon escapes undetected through the beam pipe. Figure 5.11(a) shows the fraction ξ of missing $E-P_z$ for signal MC due to the radiated photon; ξ is defined by:

$$\xi \equiv \frac{(E-P_z)^{\gamma}}{(E-P_z)^{miss}}$$

where:

γ *denotes the ISR photon*

$(E-P_z)^{\gamma} = E^{\gamma}_{gen}(1 - cos(\theta^{\gamma}_{gen}))$

The distribution of ξ for events where $E-P_z < 35$ GeV is also shown (shaded) in Figure 5.11(a). For these events in particular, the large missing momentum is due mainly to the radiated photon demonstrated by a sharp peak at $\xi = 1.0$. This is in contrast to the remainder of the sample which is characterized by large tails to the left (shown in non-logarithmic scale in the inset of Figure 5.11(a)) perhaps due to missing particles from the hadronic final, and a large number of non-ISR events.

The size of the radiative correction can be significantly reduced by restricting $(E-P_z)^{miss}$ to no more than 20 GeV, that is, requiring $E-P_z > 35$GeV, thus allowing a maximum radiated photon energy of 10 GeV. This is shown in Figure 5.12.

The $E-P_z$ requirement also suppresses photoproduction background where the scattered electron goes down the beam-pipe and carries a large amount of the $E-P_z$ with it.

5.5 Background Rejection

Whatever the detector observes can be regarded as either coming from *ep* or non-*ep* interactions, each producing its own variety of backgrounds which can enter into the final sample. Some selections have already been mentioned which help to reduce the final background contribution; the cut on y_e and DCA for example (*Sections 5.2 and 5.3*) reduces photoproduction while the vertex and track link requirements help to reduce the number

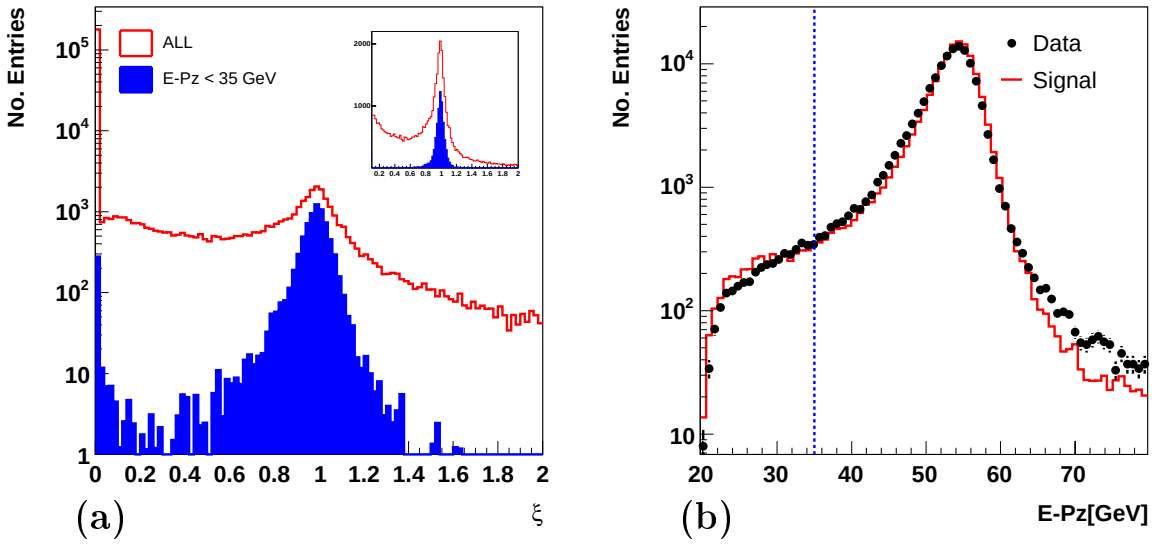

Figure 5.11: (a) ξ, the fraction of missing $E - P_z$ due to ISR. (b) The $E - P_z$ distribution.

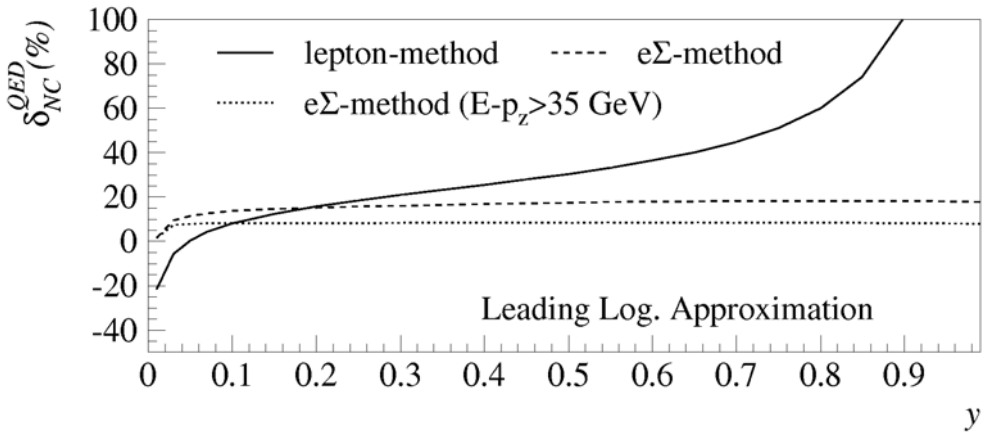

Figure 5.12: Radiative corrections for NC ep scattering versus y for $Q^2 = 500$ GeV^2. The corrections are shown for the lepton-method (e-method) and the $e\Sigma$-method (with and without the analysis cut $E - P_z > 35$ GeV)[15].

of non-ep events. This section will outline the final set of cuts used to clean up the sample. Estimates of the background contribution in the final sample for the various processes are also given.

Background from ep sources

The main sources of ep background are photoproduction (γp), elastic QED Compton and lepton pair production (l^+l^-) as described in Section 3.2. In these events, another particle apart from the scattered electron may enter the LAr and produce an electron particle candidate, which is subsequently misinterpreted as the scattered electron.

After the y_e and DCA cuts, the number of events in the final sample due to photoproduction is estimated to be ≈ 255 using MC simulations (Table 5.5). This can be considered acceptable, and so no further cuts to reduce the photoproduction contribution are made.

Elastic QED Compton and lepton pair production share a few traits not characteristic of DIS events; traits that can be used to separate these events from the signal. In particular, the distribution of the number of tracks N_{trk} , the fraction of the total energy (hadronic final state clusters + scattered electron energy) due to hadronic final state LAr clusters $E_{had}^{LArClus}/E_{tot}$ and the maximum pseudorapidity of the set of clusters in the event η_{max} [5] for background and sigal MC are shown in Figures 5.13(a), (b) and (c) with the ep background distributions normalized to the number of entries in the signal. From Figures 5.13(a), (b) and (c) it can be observed that signal events are more likely to have a greater number of tracks and hadronic final state activity, as well as produce clusters closer to the beam pipe (large η_{max}) compared to background events. Thus by restricting the minimum value of these quantities, the amount of background in the sample can be substantially reduced.

Figure 5.14 shows the progressive reduction in the amount of ep background and signal when the cuts shown in Figure 5.13 are applied. In Figure 5.14(a) the $E_{had}^{LArClus}/E_{tot}$ distribution is shown for events with 3 or less tracks. In Figure 5.14(b) the η_{max} distribution is shown when the additional cut is made: $E_{had}^{LArClus}/E_{tot} < 0.1$. It can be observed from Figure 5.14(b) that a large number of Compton and pair production events remain in the region $\eta_{max} < 3$ as opposed to the signal. Table 5.4 summarizes the inefficiency of the conbined cut: $N_{trk} < 4$ *and* $E_{had}^{LArClus}/E_{tot} < 0.1$ *and* $\eta_{max} < 3$. The inefficiency is large for ep background (73.0 % for Compton, 19.0% for pair production) compared to the signal. After applying this cut, the number of Compton and pair-production events estimated in the final sample is 128.0 ± 4.0 and 227.7 ± 2.5 respectively, which is acceptable. No further cuts against these background processes are considered.

[5] η_{max} is the maximum value of the pseudorapidity ($=ln(tan(\theta/2))$)of any cluster with energy > 0.4 GeV.

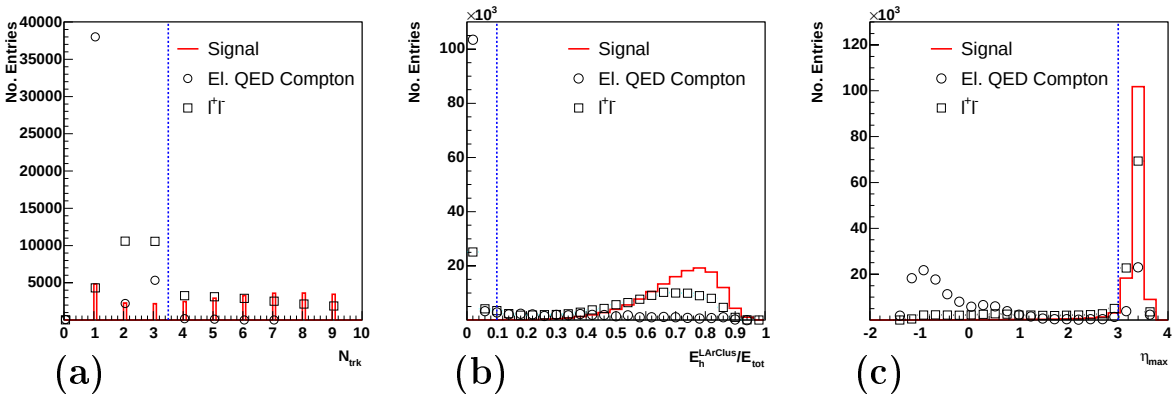

Figure 5.13: *Distribution of (a) the number of tracks N_{trk} , (b) the maximum pseudorapidity η_{max} and (c) the hadronic final state fraction $E_{had}^{LArClus}/E_{tot}$ in signal, elastic Compton and lepton pair production MC events.*

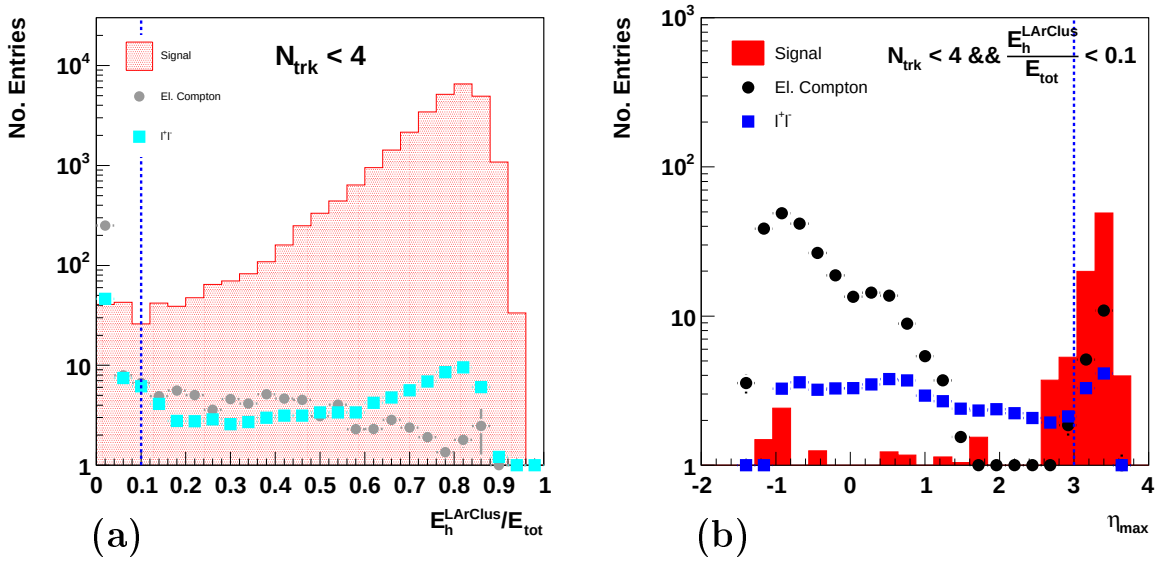

Figure 5.14: *Progressive reduction in MC events as a function on (a) $E_{had}^{LArClus}/E_{tot}$ and (b)η_{max} when the cuts in Figure 5.13 are applied.*

ep Process	Inefficiency(%)
Signal	0.02
Elastic Compton	73.0
Lepton Pair Production	19.0

Table 5.4: *Inefficiency of the combined cut: $N_{trk} < 4$ and $E_{had}^{LArClus}/E_{tot} < 0.1$ and $\eta_{max} < 3$ for signal, elastic Compton and lepton pair production.*

Background from non-ep sources

Background from non-ep interactions are removed on the basis of topological and timing information. The topological background finders use track and cluster pattern recognition to flag events as having cosmic particles or halo particles (arising of beam-gas or beam-wall collisions). Details can be found in [28]. In this analysis a selected set of the background finders are used to reject events if they are already poorly balanced in tranverse momentum ($P_t^{bal} < 0.5$ *or* $P_t^{bal} > 2.0$, *where* $P_t^{bal} = P_{th}$/) or show no calorimeter activity near the beampipe ($\eta_{max} < 3$). This constitutes the topological cut.

Background rejection by timing uses the fact that electron and proton bunches meet at the interaction point of the experiment at regular, known times (once every 96ns) whereas non-ep interactions occur irrespective of time. By measuring the time of an event with respect to that of the expected bunch collision, denoted here by CJC-T0 (measured using the tracker), and choosing only events that occur within a given time window, non-ep background can be further reduced. In this analysis, if an event has a CJC-T0 of more than $\pm$4.8ns and $\eta_{max} < 3$ then it is rejected. This constitutes the timing cut.

The ability of MCs to simulate non-ep interactions is very limited, and so the contribution from these processes to the final sample must be estimated by other means. Figure 5.15 shows the distribution of the events that are obtained using the full selection minus the non-ep cuts previously described. There are 136 229 events with 429 failing the topoligical, 109 failing the timing and 29 failing both the topological and timing cuts. The efficiency of the topological cut in selecting non-ep background ϵ_{top}^{non-ep} was determined by scanning the 109 events that failed the timing cut. It was found that out of these, 25 $\pm$ 1 were non-ep events (here the 1 represents the uncertainty in identifying an event as non-ep). Out of this 25, 24 were selected by the topological cut. This gave an efficiency $\epsilon_{top}^{non-ep} = 0.95 \pm 0.05$. The inefficiency of the topological cut was determined using signal MC and found to be $\epsilon_{top}^{ep} = 0.001327 \pm 0.000085$. Hence using:

$$\mathrm{N}^{ep} + \mathrm{N}^{non-ep} = 136229 \tag{5.3}$$

$$\epsilon_{top}^{ep}\mathrm{N}^{ep} + \epsilon_{top}^{non-ep}\mathrm{N}^{non-ep} = 429 \tag{5.4}$$

where: N^{ep} and N^{non-ep} is the number of ep and non-ep events respectively before the non-ep rejection cut it can be shown that $\mathrm{N}^{non-ep} = 261.65 \pm 25.82$ events.

Therefore the number of remaining non-ep events in the final sample $\mathrm{N}_{final\ sample}^{non-ep}$ can be estimated using:

$$\mathrm{N}_{final\ sample}^{non-ep} = \mathrm{N}^{non-ep} - \epsilon_{top}^{non-ep}\mathrm{N}^{non-ep} - \mathrm{N}_{timing\ only}^{non-ep} \tag{5.5}$$

where: $\mathrm{N}_{timing\ only}^{non-ep}$ is the number of events rejected by the timing cut *only* ($= 1 \pm 1$ events).

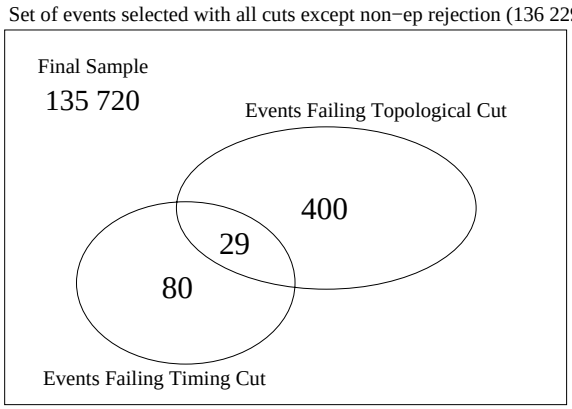

Figure 5.15: *Distribution of events prior to non-ep background cut.*

Source	No. Events in Final Sample	Contribution (%)
Photoproduction	255.2 ± 16.7	0.19
Elastic Compton	128.0 ± 4.0	0.09
Lepton Pair Production	227.7 ± 2.5	0.17
Non-*ep*	12 ± 2	$\simeq 0$
TOTAL	622.9 ± 17.5	0.46 ± 0.01

Table 5.5: *The estimated contribution of background processes to the final sample (after central vertex f_{CV} and track-linking f_{TRACK} corrections).*

In this way the number of events remaining in the final sample was found to be 12 ± 2 events.

Table 5.5 summarizes the estimated contribution of each type of background process to the final sample as number of events and percentage contribution. The total background in the sample is therefore expected to be less than 0.5 % with the non-*ep* component being negligible.

5.6 The Final Sample

The cuts implemented in the analysis are summarized in Table 5.6. When applied to the dataset, the *final sample* was produced, upon which the cross section measurement was made.

To gain confidence that the MC is doing a satisfactory job in modelling the detector´s response to expected physics, control plots are shown in Figure 5.16 for data, all MCs (signal + *ep* background) and *ep* background MCs only, binned in several quantities. Figure 5.16 includes the central vertex and track-linking efficiency corrections. In Figure 5.16 (b), (c) and (d) the *ep* background MC contribution is scaled by a factor ×5. As can be seen,

Cut	Selection Criteria
Run Selection	Require CJC1,CJC2,CIP,LAr,SPACAL,ToF,Luminosity Require runs with subtriggers ST67 and ST77
Trigger	Require ST67 or ST77 Fiducial Cuts. Reject: $-85cm < z_i < -65cm$ *and* $90° < \phi_i < 112.5°$ $-85cm < z_i < -5cm$ *and* $135° < \phi_i < 157.5°$ $-85cm < z_i < -60cm$ *and* $157.5° < \phi_i < 180.5°$
LAr Electron	Require electron candidate in LAr Reject: $\phi_{wheel} \notin [-2°, +2°]$ $15cm < z_i < 25cm$ $z_i < -190cm$
Vertex	Require Central Vertex Require $Z_{vtx} \in [2.2 - 35.0, 2.2 + 35.0]cm$
Track-Link	For $\theta_{e'} < 30$, No Track Required For $\theta_{e'} \geq 30$, Require: DTRA with DCA $<$ 12cm OR DTNV 5cm from Vertex and with DCA $<$ 12cm
Kinematic	For: $0 < Q^2 < 100$GeV , Require $y_{max} = 0$ $100 < Q^2 < 890$GeV , Require $y_{max} = 0.63$ $890 < Q^2 < s$ GeV , Require $y_{max} = 0.9$
ISR	$E - P_z > 35GeV$
ep Background Photproduction El. Compton and Pair Production	 Require DCA and y_{max} as mentioned above Reject if $N_{trk} < 4$ *and* $E_{had}^{LArClus}/E_{tot} < 0.1$ *and* $\eta_{max} < 3$
non-*ep* Background	Reject if: ($P_t^{bal} < 0.5$ *or* $P_t^{bal} > 2.0$ *or* $\eta_{max} < 3$) and topological finders fire ($\eta_{max} < 3$) and CJCT0 $\notin \pm 4.8ns$ of bunch crossing time

Table 5.6: *Summary of the cuts used to obtain the final sample.*

there is good agreement between data and simulation for all quantities plotted over the relevant ranges shown.

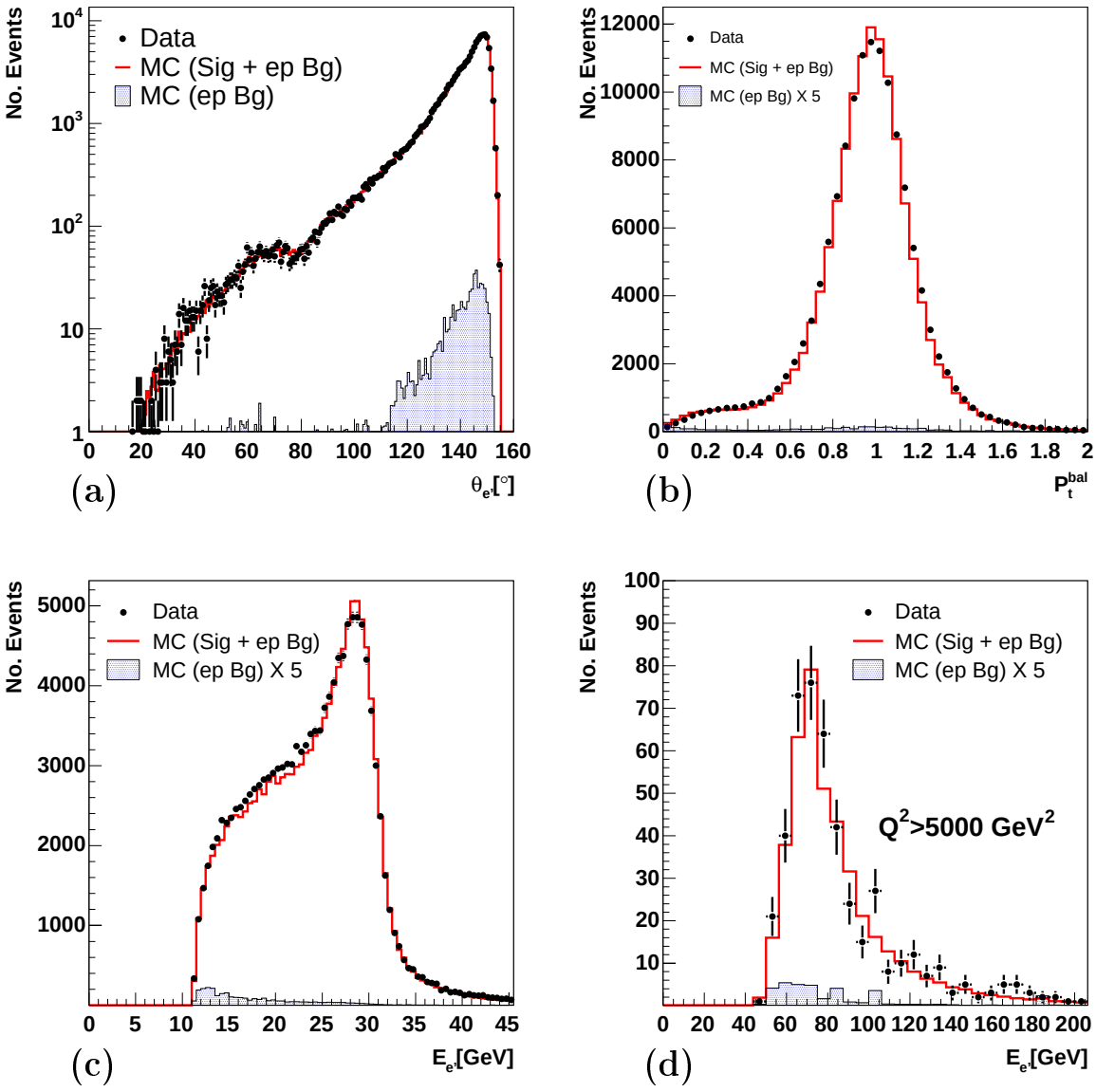

Figure 5.16: *Control plots for (a) scattered electron angle $\theta_{e'}$ (b) P_t^{bal} and (c) scattered electron energy $E_{e'}$ for data, all MCs (signal + ep background) and ep background MCs only. In (d) the $E_{e'}$ distribution is shown for events where $Q^2 > 5000\ GeV^2$. In (b), (c) and (d) the ep background MC contribution is scaled by a factor $\times 5$. Central vertex and track-linking corrections are included.*

Chapter 6

Extracting the Cross Section

Having obtained a NC sample known to have negligible background, the actual process of extracting the differential cross section can begin. This chapter explains that process. This first involves plotting the Q^2 and xQ^2 distributions of the events using the chosen reconstruction method. A suitable binning needs to be chosen, and this is done based on detector resolution as well as taking into account event statistics. Corrections are then applied for detector as well as radiative effects using Monte Carlo simulations. Finally the measurement is made by using as a starting point previous measurements done at H1 embodied in the H1PDF2000 Fit. The results are then presented and comparisons with previous results and Standard Model expectations are made.

6.1 Differential Cross Section Extraction

In this analysis the differential cross section $\mathrm{d}^2\sigma/\mathrm{d}x\mathrm{d}Q^2$ is measured at specific *points* in the x-Q^2 plane. These points are called *bin centres* (x_c, y_c). Each bin centre has an associated 2-dimensional bin defined around it. The bin centres are shown in Figure 6.1. The number of events inside each of these bins are used to calculate $\mathrm{d}^2\sigma/\mathrm{d}x\mathrm{d}Q^2$ according to the following formula:

$$\frac{d^2\sigma}{dxdQ^2} = \frac{N^{data} - N^{bg}}{\mathcal{LA}} \cdot \delta^{bc} \tag{6.1}$$

where:

- N^{data} is the number of data events in the final sample in the bin,
- N^{bg} is the number of background events in the bin estimated from the Monte Carlo simulations described in Section 5.5[1],

[1] Non-ep contribution to the background is negligible (see Table 5.5).

- $\mathcal{A}$ is the acceptance, correcting for both detector as well as radiative effects. $\mathcal{A}$ is defined as :

$$\mathcal{A} = N_{rec}^{MC}/N_{gen}^{MC} \tag{6.2}$$

  where MC refers to the signal Monte Carlo (DJANGO), N_{gen}^{MC} refers to number of events generated and binned using generated event kinematics and N_{rec}^{MC} refers to the number of events reconstructed and binned using the eΣ method of reconstruction. The MC used in this analysis was reweighted to the H1PDF2000 Fit and was unpolarized.

- δ^{bc} is the bin centre correction, correcting from the total cross section in a bin of finite size $\Delta x = x_{max} - x_{min}$ and $\Delta Q^2 = Q^2_{max} - Q^2_{min}$ to the differential cross section at the bin centre. δ^{bc} is defined by:

$$\delta^{bc} = \frac{\frac{d^2\sigma^{MC}}{dxdQ^2}\,|_{x=x_c,y=y_c}}{\int_{x_{min}}^{x_{max}}\int_{Q^2_{min}}^{Q^2_{max}}\frac{d^2\sigma^{MC}}{dxdQ^2}dxdQ^2}$$

- $\mathcal{L}$ is the data luminosity

The acceptance and bin centre corrections are taken from DJANGO, so that

$$N_{gen}^{MC} = \mathcal{L}^{MC}\int_{x_{min}}^{x_{max}}\int_{Q^2_{min}}^{Q^2_{max}}\frac{d^2\sigma^{MC}}{dxdQ^2}dxdQ^2$$

and equation 6.1 can be simplified to:

$$\frac{d^2\sigma}{dxdQ^2} = \frac{N^{data} - N^{bg}}{N_{rec}^{MC}}\cdot\frac{\mathcal{L}^{MC}}{\mathcal{L}}\cdot\frac{d^2\sigma^{MC}}{dxdQ^2} \tag{6.3}$$

The single differential cross section $\mathrm{d}\sigma_{NC}/\mathrm{d}Q^2$ is calculated in a similar way.

6.2 Bin Selection

The bin boundaries used in this analysis are those used by the nElan group [20], outlined below and shown in Figure 6.1:

$\lg(Q^2/GeV^2)$ Bin Boundaries

1.95	2.05	2.15	2.25	2.35	2.45	2.55	2.65	2.75	2.85	2.95	3.05
3.15	3.25	3.35	3.55	3.7782	4.0	4.2222	4.4437	4.6659	4.8881		

lg(x) Bin Boundaries for lg(Q^2) < 2.65

-3.0	-2.8	-2.6	-2.4	-2.2	-2.0	-1.8	-1.6
-1.4	-1.2	-1.0	-0.767	-0.5	0		

lg(x) Bin Boundaries for lg(Q^2) > 2.65

-3.0	-2.8	-2.6	-2.4	-2.2	-2.0	-1.8	-1.6
-1.4	-1.2	-1.0	-0.8386	-0.68	-0.5	-0.3	0

In order to maximise the usage of the integrated luminosity, the binning is made as fine as possible so that the differential cross section can be measured at many points. However, the binning cannot be made too fine, as statistics and limited detector resolution will degrade the quality of the measurement and introduce large errors and correlations between bins.

Figure 6.1 shows the $x - Q^2$ plane with the chosen bin boundaries. Here the circles represent the bin centers which are not necessarily in the center of the bin. The average reconstruction of the bin center is indicated by a cross; the horizontal bar corresponds to the Q^2 resolution and the vertical bar corresponds to the x resolution. The offset of the cross from the bin centre indicates the average shift due to reconstruction. In all bins the chosen horizontal bin width is larger than the Q^2 resolution. However at low y (high x), the x resolution worsens (see *Chapter* 4, Figure 4.3). For this as well as statistical reasons the size of the bins increases as x increases in each Q^2 bin. The bin centres are given below.

Q^2 Bin centres

100	120	150	200	250	300	400	500	650	800	1000	1200
1500	2000	3000	5000	8000	12000	20000	30000	50000			

x Bin Centres for lg(Q^2) < 2.65

0.0013	0.0020	0.0032	0.0050	0.0080	0.0130	0.0200	0.0320
0.0500	0.0800	0.1300	0.2500	0.400			

x Bin Centres for lg(Q^2) > 2.65

0.0013	0.0020	0.0032	0.0050	0.0080	0.0130	0.0200	0.0320
0.0500	0.0800	0.1300	0.1800	0.2500	0.400	0.6500	

As a quantitative measure that any bin i justifies its usage in performing the measurement, it is useful to define the stability $\mathcal{S}$ and purity $\mathcal{P}$ in the following way:

$\mathcal{S} = \mathrm{N}^{MC}_{gen+rec}(i)/N^{MC}_{gen+sel}(i)$

$\mathcal{P} = N^{MC}_{gen+rec}(i)/N^{MC}_{rec}(i)$

where:

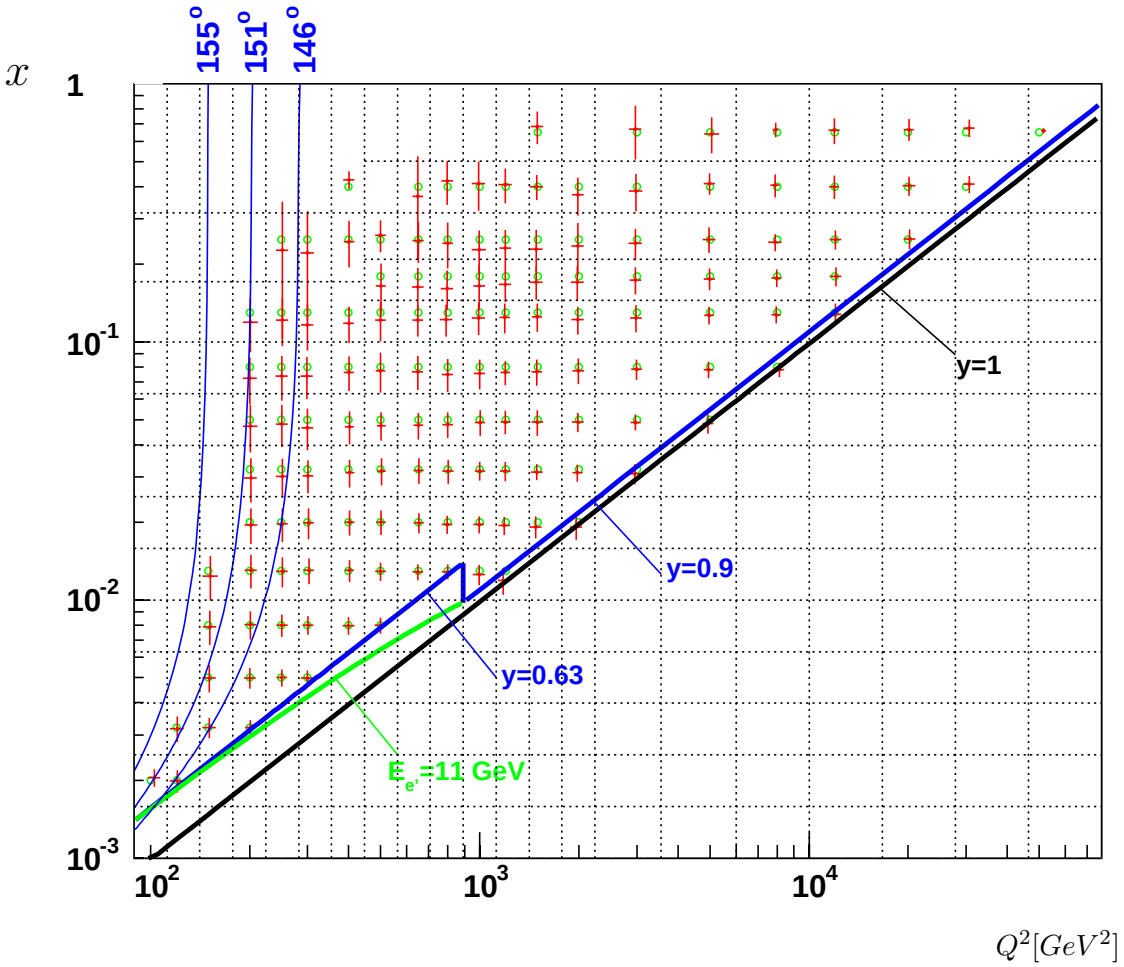

Figure 6.1: *The $x-Q^2$ Kinematic Plane with the kinematic limit y=1 shown . The vertical and horizontal lines show the Q^2 and x bin boundaries respectively. Also shown are the cuts y=0.9 and y=0.63 and the constant energy line $E_{e'}$= 11 GeV. The approximate maximum polar angle acceptance due to the Z-vertex cuts and the minimum z-impact cut are also shown (141^o, 151^o, 155^o). The bin centres are marked by circles. Crosses represent the reconstruction with horizontal and vertical bars being the Q^2 and x resolution respectively. The offset of the cross from its bin centre (Q^2_c, x_c) depicts the average systematic shift due to reconstruction. Only good bins are shown (see Section 6.2). Note however that no cross section measurement is quoted for the bin centres (1200,0.013), (2000,0.02), (3000,0.032), (5000,0.05), (8000,0.08) and (12 000, 0.13) since the inelasticity y of each of these points is greater than the maximum reconstructed inelasticiy of 0.9. See Appendix B for resolution plots.*

- $N^{MC}_{gen+rec}(i)$ is the number of events generated *and* reconstructed in the bin
- $N^{MC}_{gen+sel}(i)$ is the number of events generated in the bin and reconstructed anywhere.

Other quantities were defined in the preceding section.

As an example suppose that 100 events were generated in a particular bin. Out of the 100, 80 were reconstructed. And out of the 80, 55 remained in the bin (so that 25 migrated out). Also, 65 events were reconstructed in total in the bin (that is, 10 migrated in from neighbouring bins). Then:

$N^{MC}_{gen}(i) = 100,$

$N^{MC}_{gen+rec}(i) = 55,$

$N^{MC}_{gen+sel}(i) = 80,$

$N^{MC}_{rec}(i) = 65,$

$\mathcal{S} = 55/80\ (68.75\%),$

$\mathcal{P} = 55/65\ (\approx 85\%),$

$\mathcal{A} = 65/100\ (65\%).$

Figure 6.2 shows the distributions of stability, purity, and acceptance for bins of constant Q^2 as a function of x. It can be seen that for any Q^2 bin, the purity and stability drops as x increases since the resolution in x gets worse. As Q^2 increases beyond 1500 GeV^2 , $\mathcal{P}$ and $\mathcal{S}$ increase to $\approx 70\%$. The acceptance is better than 70% in most bins.

In this analysis, the stability and purity are required to be better than 30% and the acceptance more than 20% [15] for a bin to be considered *good*. These cuts are shown in Figure 6.2. A good bin is used for the cross section measurement. Note however that no cross section measurement is quoted for the bin centres (1200,0.013), (2000,0.02), (3000,0.032), (5000,0.05), (8000,0.08) and (12 000, 0.13) since the inelasticity y of each of these points is greater than the maximum reconstructed inelasticity of 0.9, see Figure 6.1.

Background Correction

Figure 6.3 shows the amount of background as a percentage of events in the data for the bins where a cross section is quoted. In most bins the percentage background is between 0.1 to 0.5%. The highest percentage background is less than 3%. The photoproduction background contribution increases at high y; elastic Compton and lepton pair-production have larger contributions in the low y high Q^2 bins.

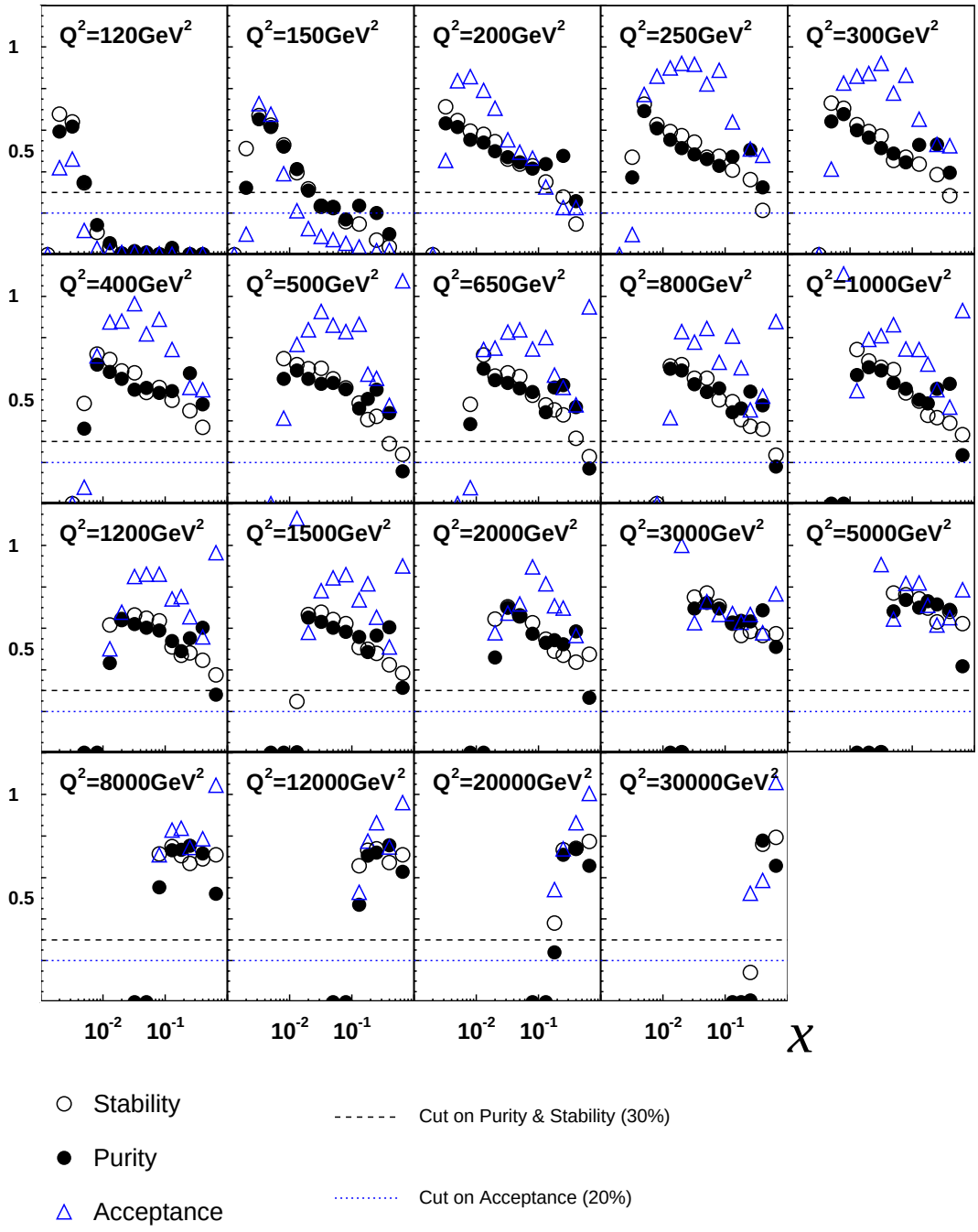

Figure 6.2: *Stability $\mathcal{S}$, purity $\mathcal{P}$ and acceptance $\mathcal{A}$ for the binning scheme, shown for constant Q^2 bins as a function of x. The cuts used to define a good bin are also shown.*

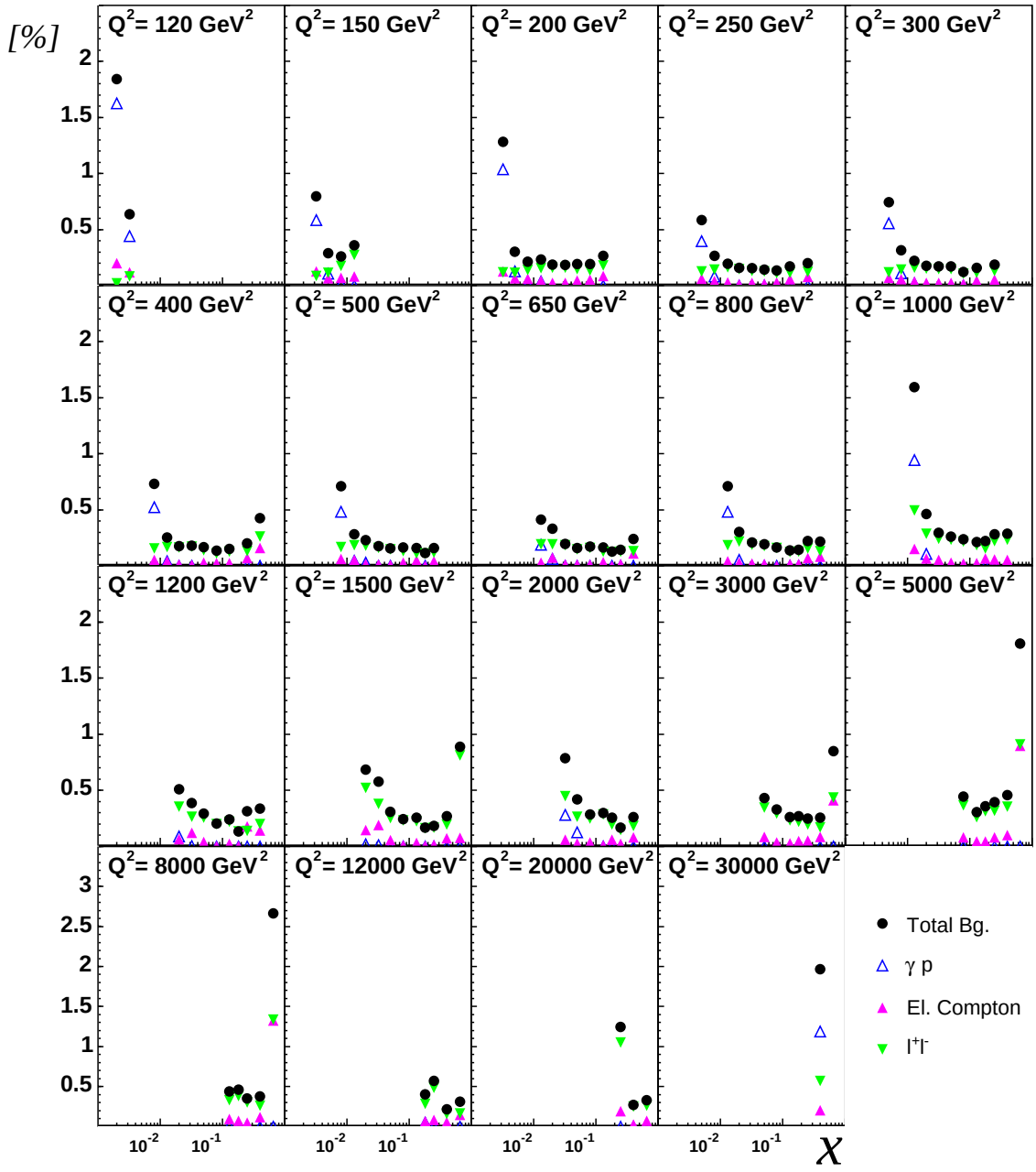

Figure 6.3: *Background estimate as a percentage of the number of data events for bins where a cross sectioin is quoted. The last x bin for $Q^2 = 30000\ GeV^2$ has no events in data.*

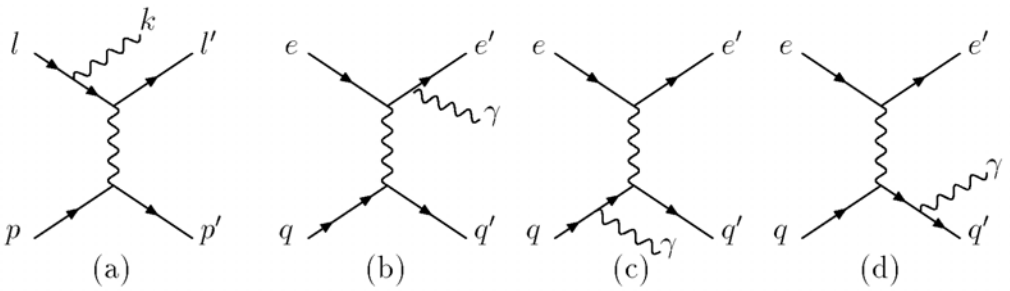

Figure 6.4: *Feynman diagrams for radiative NC scattering. In (a) the 4-momenta of the particles are denoted; the other figures indicate the particle types [15].*

6.3 Radiative Corrections

Radiative corrections in DIS arise from higher order processes and from the self-energies of the exchanged bosons. The processes are suppresssed by the coupling strength, the fine structure constant α in the case of photon radiation.

In Figure Figure 6.4, Feynman diagrams for Bremsstrahlung processes where the photon is emitted either from the lepton line (*leptonic* photon radiation, (a) and (b)) or the quark line (*quarkonic* photon radiation, (c) and (d)) are presented.

Leptonic contributions can be divided into initital state radiation (ISR, Figure 6.4(a)) and final state radiation (FSR, Figure 6.4(b)) depending on whether the photon in emitted from the incoming or scattered lepton. In ISR the photon is emitted predominantly colinear with the incoming lepton (negative z direction at H1) and has the greatest effect on the reconstructed kinematics (see *Chapter* 4), and so leads to the largest corrections. In FSR, the photon is emitted mainly in the direction of the outgoing electron. Both the photon and scattered electron are usually reconstructed as one cluster, so these events give rise to smaller corrections.

Quarkonic contributions are suppressed by the fractional charge of the quarks squared and the quark mass squared. Numerical estimates [15] show that the quarkonic radiative correction is very small, reaching less than a percent at high x and Q^2 .

The self-energy of the exchanged photon is taken into account by the running of α.

Events in the data correspond to all orders of electroweak interaction diagrams. The measured cross section is corrected implicitly using the MC for QED radiation.

6.4 Systematic Uncertainties

The systematics uncertainties of quantities that are used to reconstruct the kinematics (eg. electron energy $E_{e'}$), as well as the uncertainty of the various efficiencies (eg. trigger

efficiency) propagate to the measured cross section. Theoretical uncertaintites (eg. the theoretical uncertainty on the Bethe-Heitler cross section σ_{BH} is 0.5% [14]) also contribute. In the following discussion, a distinction between bin-to-bin *correlated* and *uncorrelated* errors is made. Correlated errors refer to those that are irrespective of the bins, for example, the error on the luminosity is universal. Uncorrelated errors refer to uncertainties that are localized, such as the electron energy uncertainty in the different wheels. The total systematic error is found by adding the individual errors in quadrature.

- Luminosity - The luminosity is determined using the Bethe-Heitler process ($ep \rightarrow ep\gamma$) as the reference cross section. Bethe-Heitler processes are reconstructed by tagging the photon at the photon detector (PD) located at z = -102.9 m. The uncertainty of the luminosity $\Delta\mathcal{L}/\mathcal{L}$ is presently estimated to be 2.4%.

- Background subtraction - The background estimated using MC is given an uncertainty of 30%. This is the uncertainty attributed to photoproduction MC in [14], and is assumed to be a reasonable estimate for the uncertainties in the elastic Compton and lepton pair-production simulations. The resulting uncertainty on the cross section δ^B is shown in Figure 6.5. δ^B increases in bins where the contribution of ep background is relatively large (see *Section* 6.2). The systematic error on the cross section due to background is at most 0.83 % which is negligible compared to the total error on the cross section.

- Trigger efficiency - The uncertainty in the trigger efficiency is quoted conservatively at 1%. Further studies are needed for a more precise estimation.

- Electron finding efficiency - The uncertainty in ϵ_{ELEC} is taken to be 2%. This represents a conservative value until more in depth studies can be done.

- Vertex efficiency - The uncertainty in the efficiency of reconstructing a central vertex is taken as 0.7% for $\log(y) <$ -1.5 and considered negligible elsewhere (see *Section* 5.3). The application of the uncertainty is done on a bin by bin (not event by event) basis. Bins in which there can exist events having $\log(y) <$ -1.5 as well as events having $\log(y) \geq$ -1.5 are conservatively given the maximum uncertainty, as shown in Figures 6.6 and 6.5.

- Track-linking efficiency - The track-linking efficiency is given a 1% uncertainty for $\theta_{e'} < 70^\circ$ and 0.5% elsewhere (see *Section* 5.3). The efficiency is applied on a bin by bin basis, as in the case of the central vertex efficiency and is shown in Figures 6.6 and 6.5.

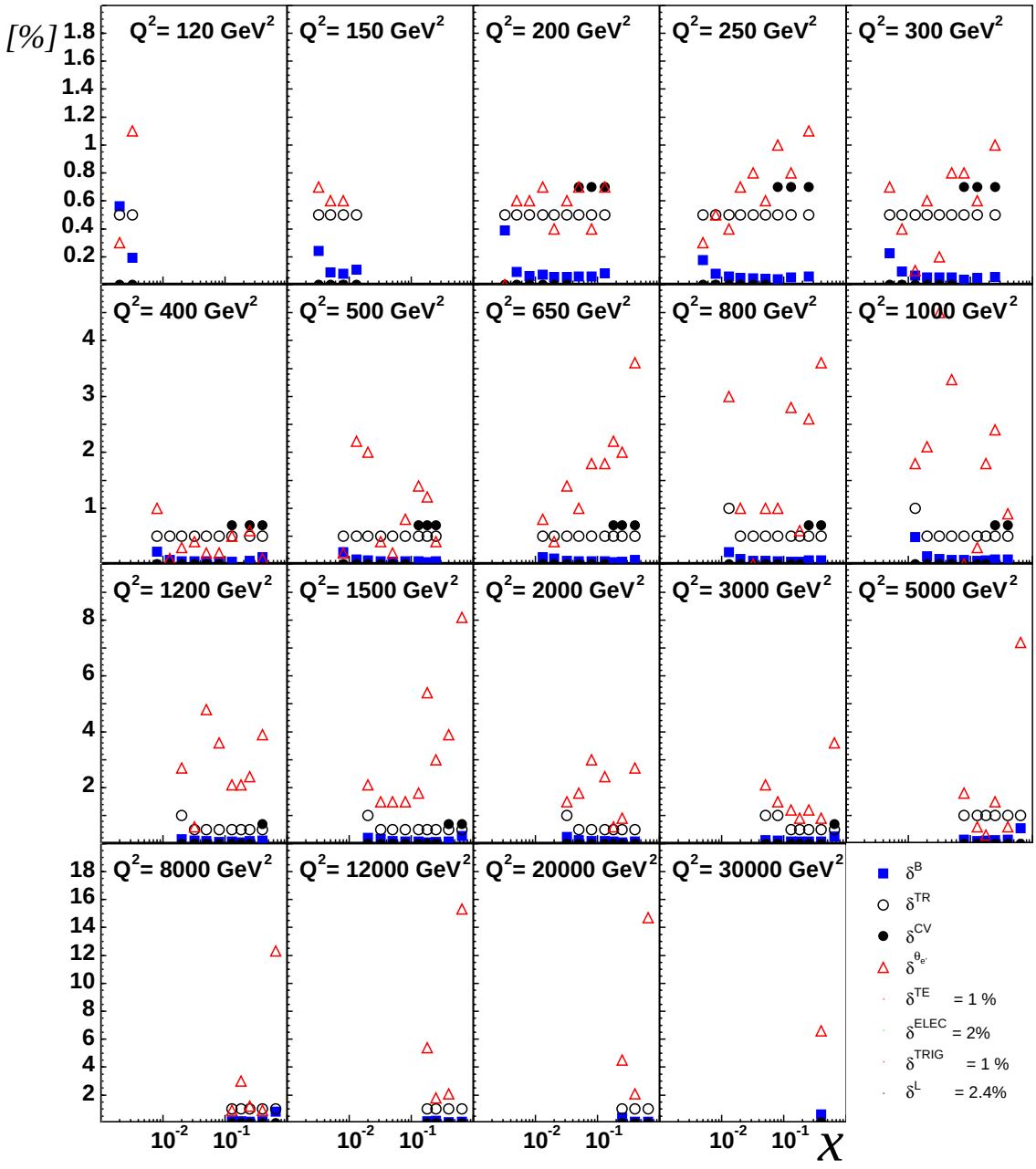

Figure 6.5: *Systematic errors given as a percentage of the measured cross section. Shown are the errors due to uncertainties on luminosity, trigger efficiency, electron identification efficiency, CV efficiency, track-linking efficiency, electron polar angle and background subtraction.*

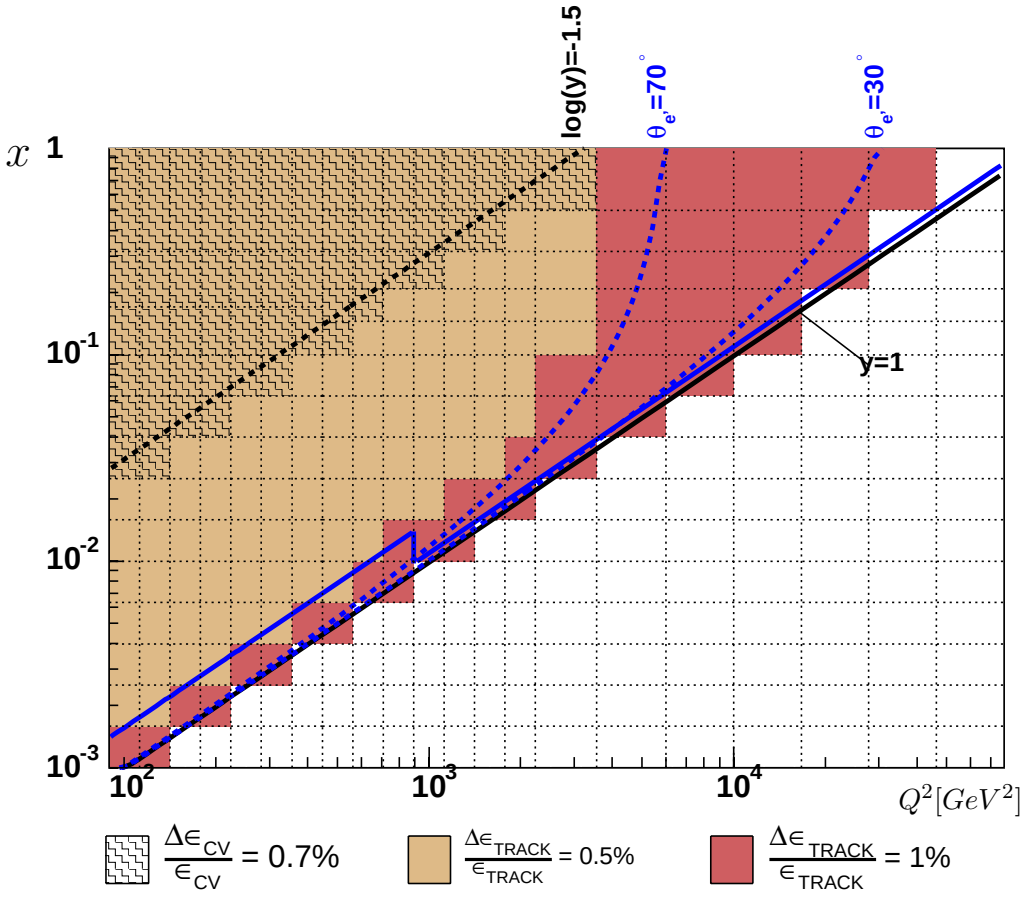

Figure 6.6: *The systematic uncertainties quoted for the central vertex ($\Delta\epsilon_{CV}/\epsilon_{CV}$) and track-linking($\Delta\epsilon_{TRACK}/\epsilon_{TRACK}$) efficiencies. The correction is done bin by bin. The maximum uncertainty is used for each bin.*

The systematic uncertainties quoted in the following are taken from [14] which corresponds to HERAI data. Comments and corrections have been made where appropriate.

- Electron energy - The electron energy calibration was checked using as the reference scale the energy determined by the *double angle* method E_{DA} which uses the scattered electron polar angle $\theta_{e'}$ as well as the *jet angle* of the hadronic final state γ_h defined by:

$$\tan\frac{\gamma_h}{2} = \frac{\Sigma_h}{P_{th}} \tag{6.3}$$

and

$$E_{DA} = \frac{2E_e \sin\gamma_h}{\sin\gamma_h + \sin\theta_{e'} - \sin(\gamma_h + \theta_{e'})}. \tag{6.4}$$

This method of reconstruction of the electron energy is thus independent of the calibration of the electromagnetic section of the calorimeter. The sample used for the study was the final sample with the additional requirements [10, 15]:

  - Require $44 < E - P_z < 66$ GeV to reduce radiative effects on E_{DA},
  - Require $\gamma_h > 8^\circ$ thus ensuring that the hadronic final state angle is well contained in the calorimeter,
  - Require $y_\Sigma < 0.5$ for $\theta_{e'} < 80^\circ$ and $y_\Sigma < 0.3$ otherwise. This requirement ensures a precise reconstruction and good resolution of the DA energy since for this kinematic range $E_{DA} \gtrsim 25$ GeV.

Figure 6.7(a) shows the resolution $\sigma(E_{e'}/E_{DA})$ for data and signal MC as a function of the z-coordinate of the impact position of the electron z_i. The resolution is best ($\lesssim 4\%$) in the CB1 wheel and worsens towards the backward direction in the BBE wheel to about 7%. The z-cracks at $\approx$ -150 cm and $\approx$-60 cm lead to poorer resolution. Generally there is good agreement between data and MC. Statistics in the data are low in the forward direction leading to larger uncertainties.

Figure 6.7(b) shows the mean $\langle E_{e'}/E_{DA}\rangle$ as a function of z_i for data and signal MC. The best agreement between data and MC occurs in the CB1 wheel. However in the BBE there is a systematic disagreement as the MC overestimates compared to data. The situation is reversed in the forward direction as the MC underestimates.

The ratio $\langle E_{e'}/E_{DA}\rangle_{MC}/\langle E_{e'}/E_{DA}\rangle_{DATA}$ expressed as a percent is shown in Figure 6.8(a), together with the systematic uncertainties used in the analysis. As can be seen, the uncertainties quoted agree with the current data except for the region $-70 < z_i < 20$ cm. For this region the $\Delta E_{e'}/E_{e'}$ is quoted at 0.7% but is closer to $\approx$

Range of $\theta_{e'}$[°]	$\Delta\theta_{e'}$ [mrad]	Q^2 Bin Centre Range	$f_{\theta_{e'}}$
$(0, 120)$	± 3	(100,400)	$\times 1$
$(120, 135)$	± 2	(500,800)	$\times 2$
$(135, 155)$	± 1	(1000,30000)	$\times 3$

Table 6.1: *The electron polar angle uncertainty.*

5%. Those bins that are most affected are shown in Figure 6.8(b) and correspond to the range $890 \lesssim Q^2 \lesssim 355$ GeV^2. For these these points then, the error on the cross section due to electron energy uncertainty is underestimated[2].

- Electron polar angle - If the electron track produces hits in the outer z chamber (COZ), then the polar angle from the reconstructed track provides a means to estimate the resolution of $\theta_{e'}$ measured exclusively by the calorimeter in this analysis. The resolution is dependent on $\theta_{e'}$ and given in Table 6.1.

  In this analysis the error on the cross section due to the electron polar angle measurement $\delta^{\theta_{e'}}$ is conservatively increased by a factor $f_{\theta_{e'}}$ based on the Q^2 binning, as given in Table 6.1. Figure 6.5 shows $\delta^{\theta_{e'}}$ for the various bins where the measurement is made.

- Hadronic energy - The uncertainty quoted for the hadronic energy measured in the LAr calorimeter is 1.4% for $12 < P_{th} < 50$ GeV and $\gamma_h > 15°$ and 2% otherwise. This can be considered reasonably consistent with HERA II. The uncertainty on the hadronic energy scale of the SPACAL is 5%. The uncertainty of hadronic energy using tracks is quoted to be 3%. The three contributions (LAr, SPACAL, tracks) result in a correlated error on the cross section which is typically $< 1\%$ but increases at low y to $\sim 5\%$.

- Noise - An uncertainty of 25 % is given to the amount of energy in the LAr calorimeter attributed to noise. This gives rise to a sizeable correlated systematic error at low y, reaching ~ 10 % at $x = 0.65$ and $Q^2 \lesssim 2000$ GeV^2 .

- Radiative correction - An uncorrelated error of 1% is assigned to the QED radiative corrections.

Typically, the systematic uncertainty on the cross section is between 4 to 5% and can be expected to improve subsequent to further study.

[2]Subsequent to this analysis, the electron energy calibration was improved so that the uncertainty at present is better than 1% in the region $-70 < z_i < 20$ cm [22].

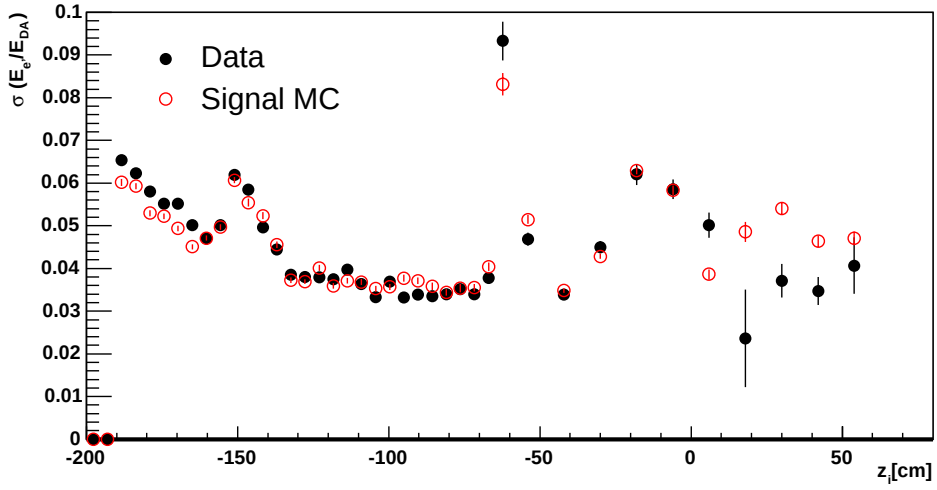

(a)

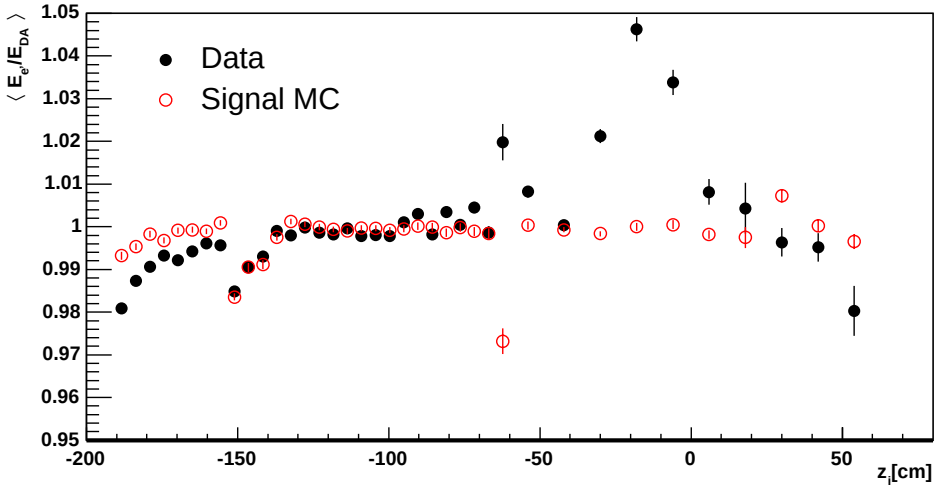

(b)

Figure 6.7: *The electron energy from the LAr calorimeter $E_{e'}$ is compared to its reconstructed value using the double angle method E_{DA} for data and signal MC. In (a) the resolution σ and (b) the mean of $E_{e'}/E_{DA}$ is plotted as a function of z_i. The effects of the z-cracks at $\approx$ -150 cm and ≈ -60 cm are visible as the resolution worsens. See Appendix B for resolution plots.*

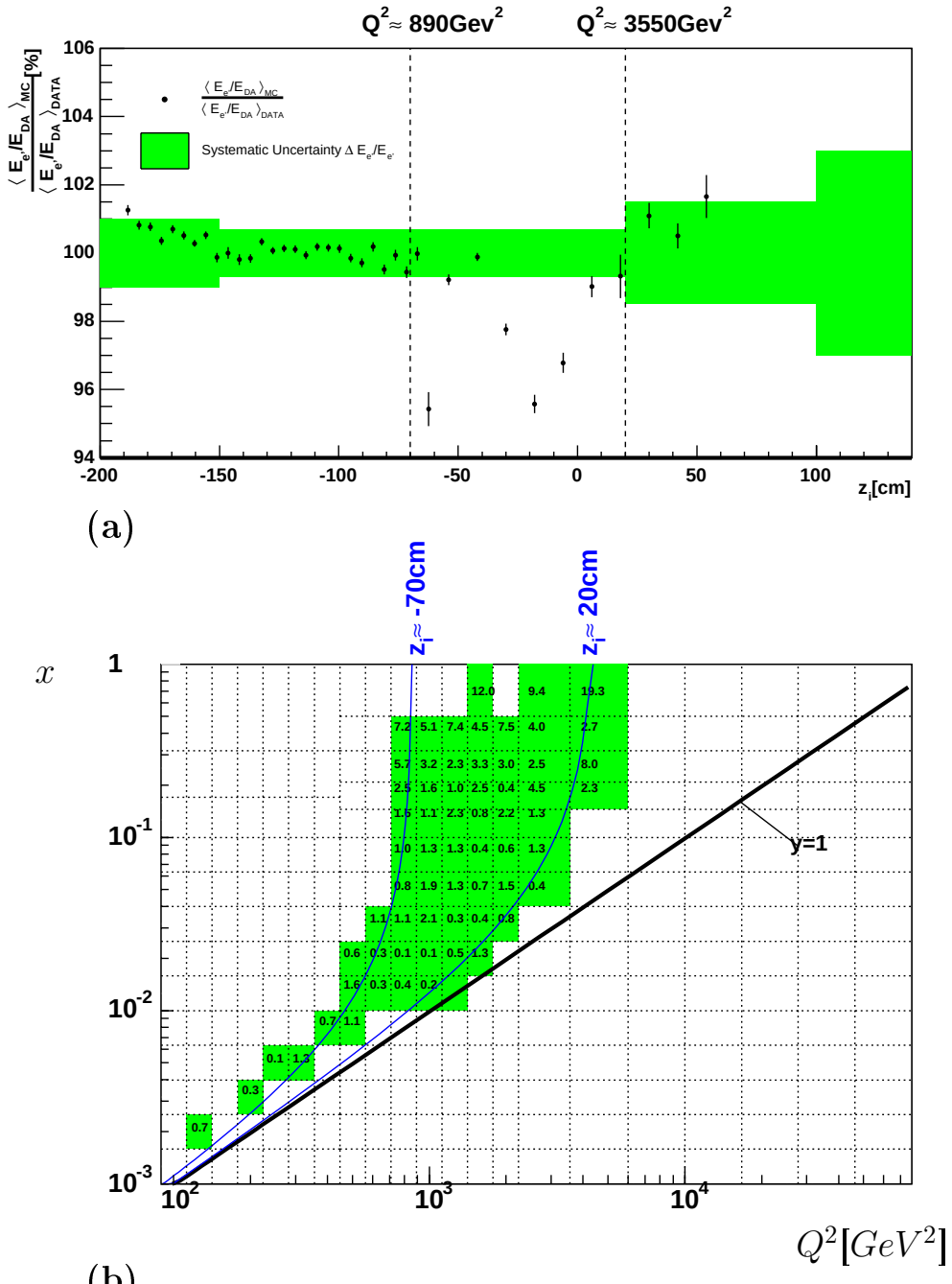

Figure 6.8: *(a) The systematic uncertainty for the electron energy as a function of z_i. For the region $-70 < z_i < 20$ cm the quoted uncertainty is less than that of the present data. Those bins that are affected are shown in (b) together with the percentage error on the measured cross section ($\delta^{E_{e'}}$)due to the energy uncertainty. For these bins, the cross section error is underestimated.*

Range of Q^2 [GeV^2]	Integrated Luminosity of Signal MC [pb^{-1}]
$(60, 100)$	50.65
$(100, 1000)$	82.05
$(1000, 10000)$	366.52
$(10000, s)$	35466.15

Table 6.2: *The integrated luminosity of signal MC events used for various Q^2 ranges.*

Statistical Uncertainties

The two main contributions to the statistical error originate from N^{Data} and N^{MC}_{rec} in equation 6.3:

- Statistical error due to data, δ^{data}_{stat} - This refers to the error on the cross section due to the statistical uncertainty on the number of data events.

- Monte Carlo statistical error, δ^{MC}_{stat} - This refers to the error on the cross section due to the statistical uncertainty on the number of signal MC events reconstructed, that is:

$$\delta^{MC}_{stat} = \frac{\Delta N^{MC}_{rec}}{N^{MC}_{rec}} \tag{6.5}$$

  where ΔN^{MC}_{rec} is the square root of the sum of squares of the weights.

The total statistical error on the cross section is denoted by δ_{stat} which is calculated by adding δ^{data}_{stat} and δ^{MC}_{stat} in quadrature. Figure 6.9 shows δ_{stat}, δ^{data}_{stat} and δ^{MC}_{stat} as a percentage. It can be seen that δ^{data}_{stat} increases with Q^2 due to the $\sim 1/Q^4$ dependence of the cross section. To reduce this effect in MC, more integrated luminosity is used to generate events for the higher Q^2 regions, and this is shown in Table 6.2. The MC contribution to the statistical error at larger Q^2 is therefore significantly less than the data compared to the lower Q^2 regions.

Since the cross section decreases with x, the statistical error increases with x, as seen in Figure 6.9 for constant Q^2 bins.

Figure 6.10 shows the total error δ_{tot} for constant Q^2 as a function of x, along with the statistical and systematic contributions. For $Q^2 \lesssim 400$ GeV^2 the total uncertainty is dominated by systematic errors; at larger Q^2 statistical uncertainties begin to dominate. Note that at the point $Q^2 = 150$ GeV^2, $x = 0.013$ which lies close to the edge of the LAr acceptance, Figure 6.1, there is no cross section measurement quoted in the publication, therefore only the statistical error given.

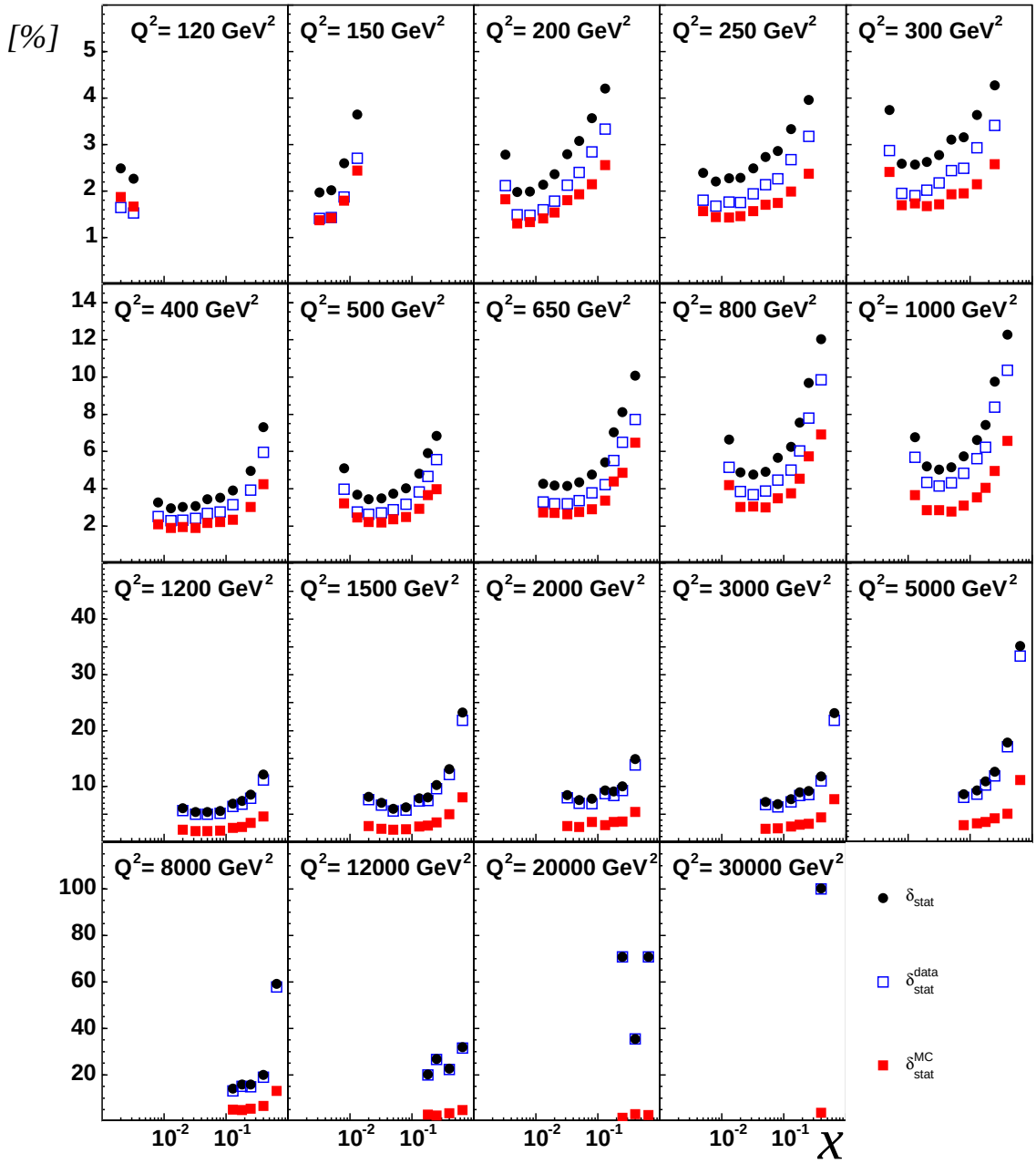

Figure 6.9: *Statistical error on the cross section given as a percentage. Contributions from the data δ_{stat}^{data} and signal MC δ_{stat}^{MC} are given, together with the total statistical error δ_{stat}.*

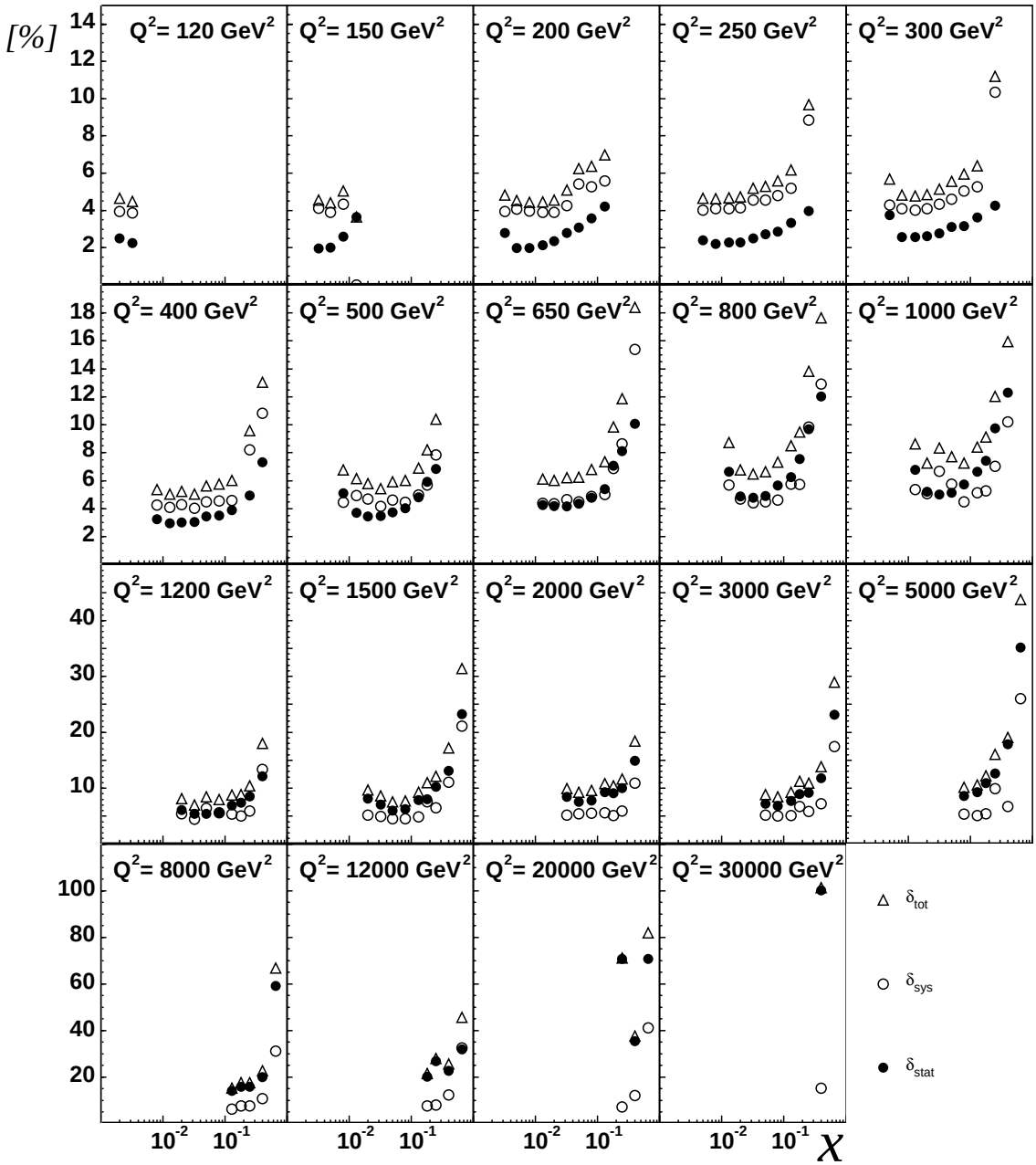

Figure 6.10: *Statistical, systematic and total error as a percentage of the measured cross section.*

6.5 Results

The Reduced Cross Section $\tilde{\sigma}_{NC}$

It is customary to present the double differential NC cross section as a *reduced cross section* $\tilde{\sigma}_{NC}$ defined by:

$$\tilde{\sigma}_{NC} \equiv \frac{xQ^4}{2\pi\alpha^2}\frac{1}{Y_+}\frac{d^2\sigma}{dxdQ^2} \tag{6.6}$$

The reduced cross section is closely related to the structure function $\tilde{F}_2$ since the coefficients of $\tilde{F}_L$ and $\tilde{F}_3$ are second order in x and y (see *Section* 1.2).

The reduced cross section is shown in Figure 6.11 as a function of x for fixed Q^2 . It covers the range $120 \leq Q^2 \leq 30\ 000$ GeV^2 and $0.002 \leq x \leq 0.65$. Also shown in Figure 6.11 is the the Standard Model (SM) expectation given by the H1PDF2000 fit [14] as well as data published in [14]. As can be seen, there is good agreement between the data and published measurements.

The ratio of the $\tilde{\sigma}_{NC}$ as determined from data divided by the $\tilde{\sigma}_{NC}$ as given by the fit is plotted in Figure 6.12. The SM expectation was not taken into account, so that the comparison can viewed as a conservative measure of agreement. From Figure 6.12 it can be seen that there is good agreement between data and the fit over the full Q^2 range within the uncertainties quoted.

Finally Figure 6.13 shows $\tilde{\sigma}_{NC}$ at fixed x as a function of Q^2 for large values of x ($\geqslant 0.08$). The reduced cross section is scaled so that all points can be seen on the same plot.

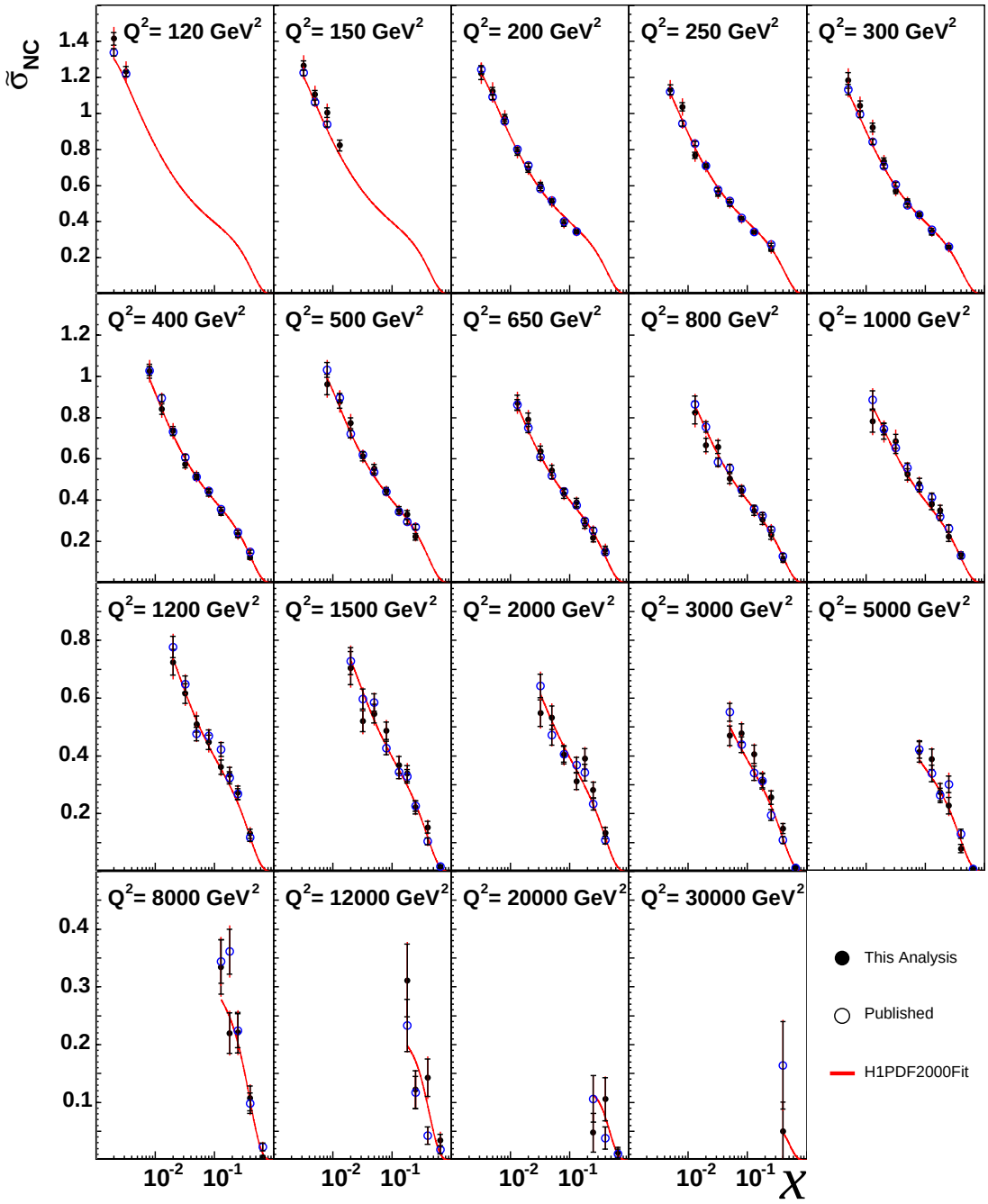

Figure 6.11: *The reduced cross section $\tilde{\sigma}_{NC}$ for fixed Q^2 as a function of x. Shown are the results from this analysis, the publication [14] and the Standard Model expectations determined from the H1PDF2000Fit. The inner error bars represent the statistical error. The full error line represents the statistical and systematic errors added in quadrature.*

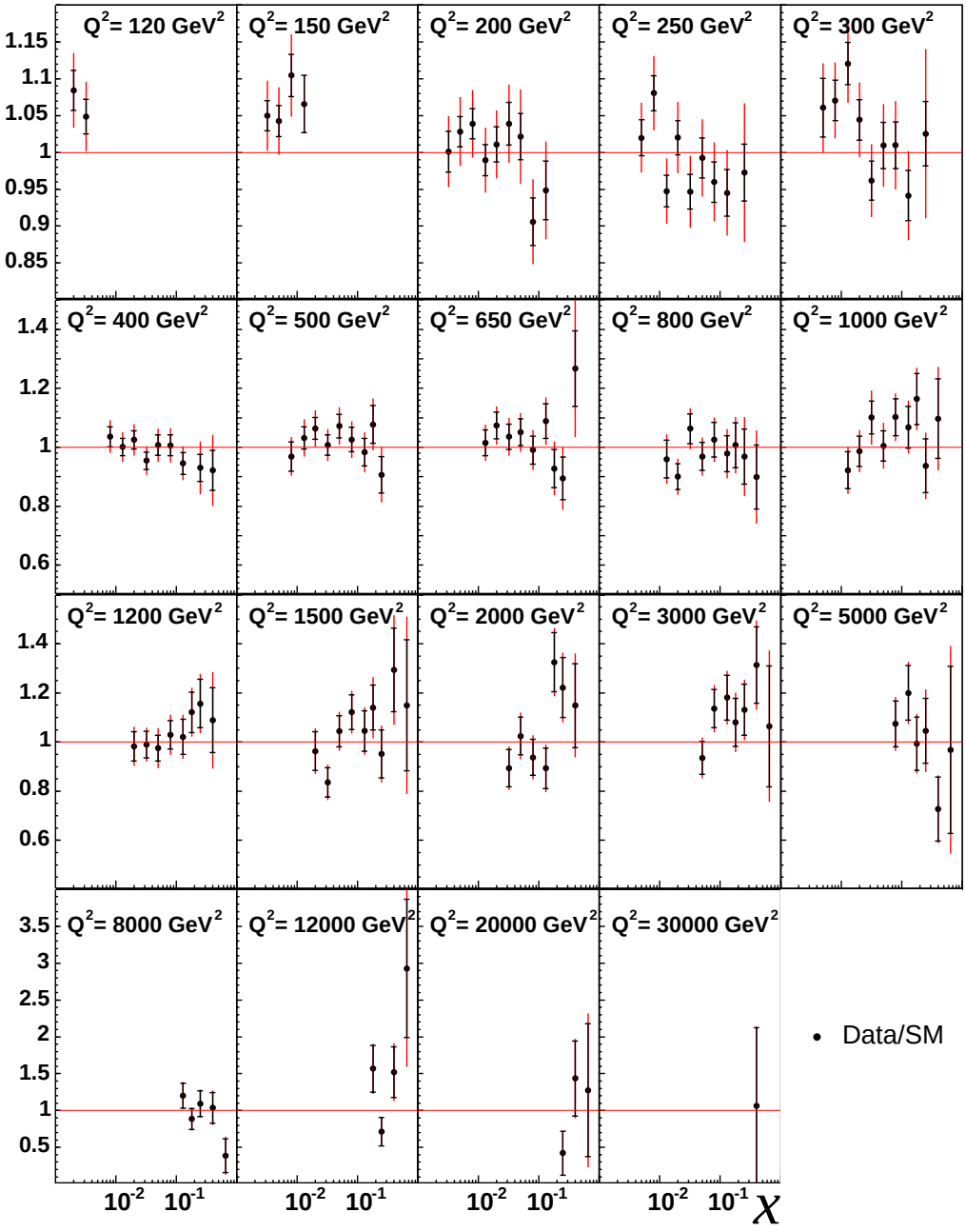

Figure 6.12: *The reduced cross section $\tilde{\sigma}_{NC}$ from this analysis divided by the Standard Model expectation as determined from the H1PDF2000 Fit. The inner error bars represent the statistical error. The full error line represents the statistical and systematic errors added in quadrature. Note that the SM expectation error was not considered in the comparison, so that this represents a conservative measure of agreement between data and the fit.*

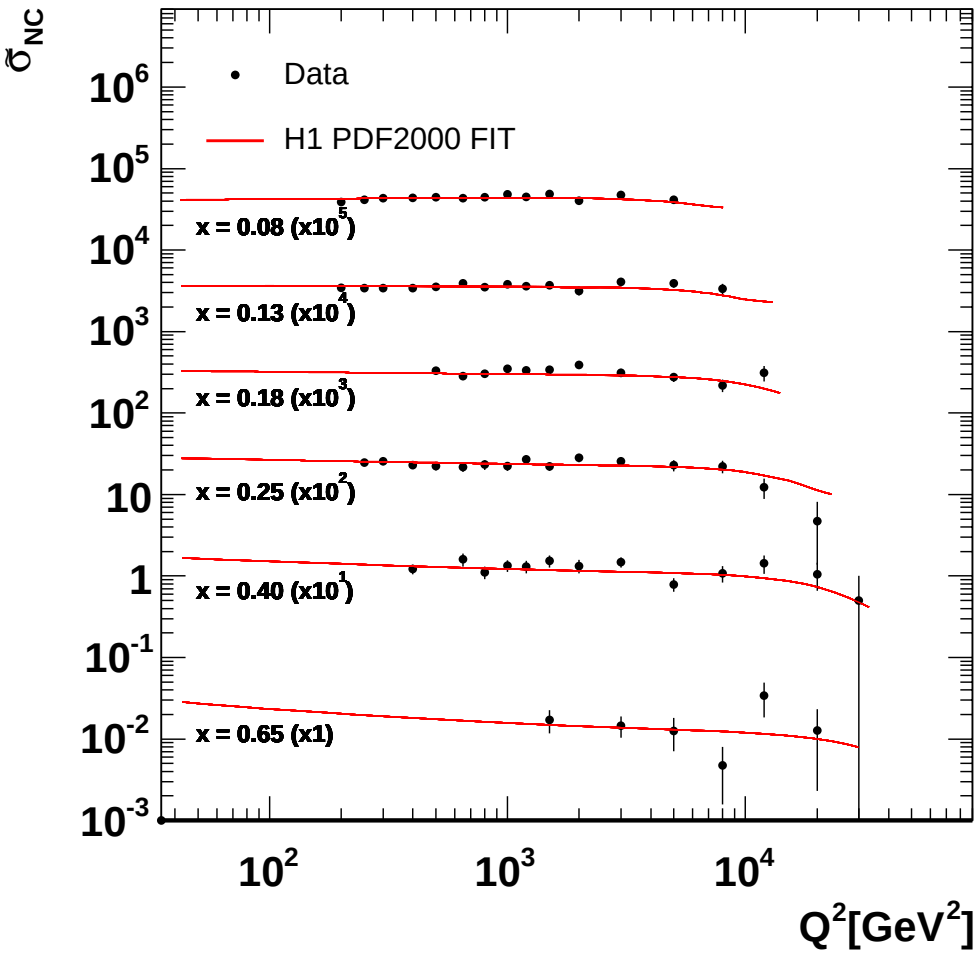

Figure 6.13: *The reduced cross section $\tilde{\sigma}_{NC}$ from this analysis and the H1PDF2000 Fit for fixed x as a function of Q^2. The cross section is scaled as indicated and error bars represent the total error on the measurement.*

The Single Differential Cross Section $\mathrm{d}\sigma_{NC}/\mathrm{d}Q^2$

Figure 6.14(a) shows the Q^2 binning (for only part of the $x - Q^2$ kinematic plane) used to measure the single differential cross section $\mathrm{d}\sigma_{NC}/\mathrm{d}Q^2$. All bins extend to $y = 0.9$ even though the reconstruction is limited to $y < 0.63$ for $Q^2 < 890$ GeV^2 (see *Section* 5.2). The purity, stability and acceptance are calculated and shown in Figure 6.14(b). It can be seen that both purity and stability are higher than in the 2 dimensional binning, Figure 6.2 since now events can only migrate in the Q^2 direction and the resolution of Q^2 is excellent (see *Chapter* 4).

It should be noted that for the case where $Q^2 < 890$ GeV^2, the measured cross section would have a greater dependence on the fit since only part of the bin is reconstructed (up to $y_e < 0.63$). However, the *fit* was made using *measurements* in the high y region bounded by $E_{e'} > 6$ GeV, $0.63 < y_e < 0.9$ and 90 GeV^2 $< Q^2 <$ 890 GeV^2 normally called the *high-y analysis*[14]. Therefore the measurement made here should not be viewed as purely an extrapolation into unmeasured kinematic regions, but rather a correction to an already made measurement.

Figure 6.15(a) shows the single differential cross section for data, publication and the H1PDF2000 Fit. It covers the range $150 \leq Q^2 \leq 30\,000$ GeV^2. Inner error bars represent statistical errors while the full error bar represents the total error given by adding the statistical and systematic errors in quadrature. Since there is no single differential cross section $\mathrm{d}\sigma_{NC}/\mathrm{d}Q^2$ quoted in the publication for $Q^2 = 150$ GeV^2 (close to the edge of the LAr acceptance), only the statistical error is shown. Also shown in Figure 6.15(b) is the data divided by the fit.

As can be seen there is excellent agreement between the data and the fit.

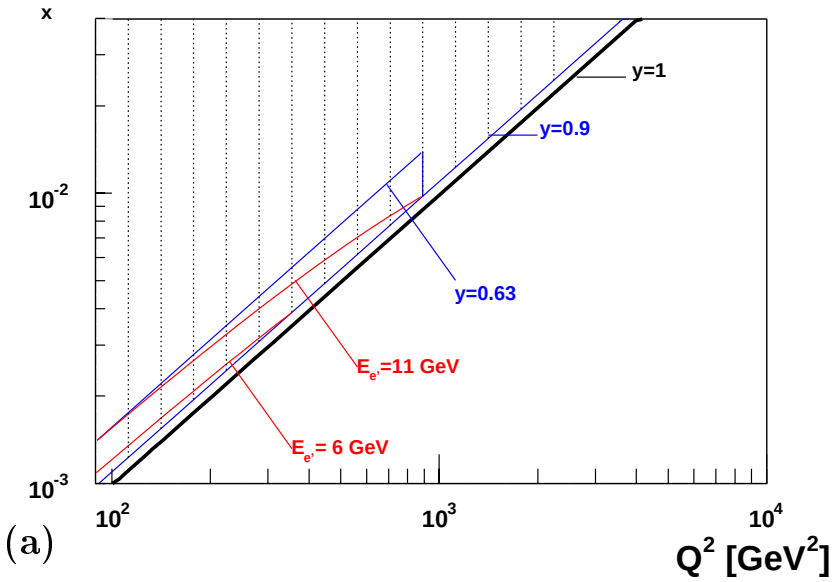

(a)

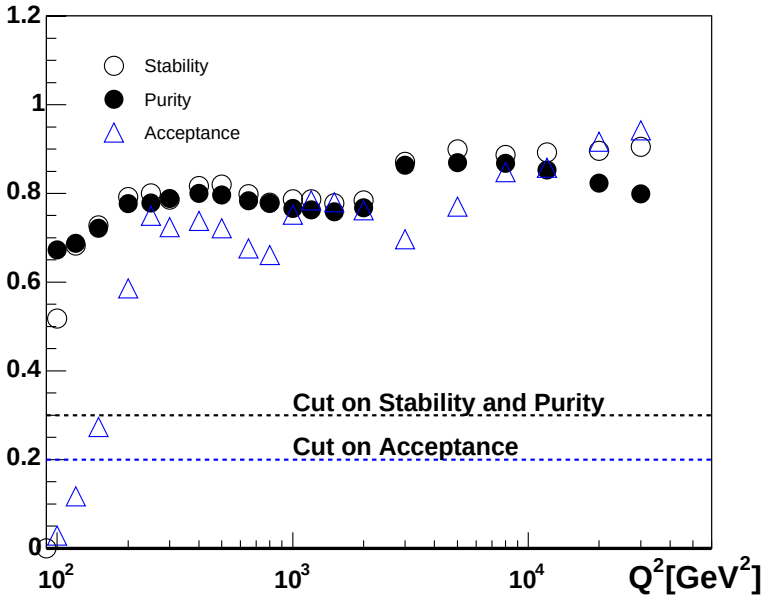

(b)

Figure 6.14: *(a) The Q^2 binning used to determine the single differential cross section $\mathrm{d}\sigma_{NC}/\mathrm{d}Q^2$ (shown for part of the kinematic plane). All Q^2 bins extend to $y = 0.9$. (b) The corresponding purity, stability and acceptence which are used to determine the good bins upon which the cross section measurement is made.*

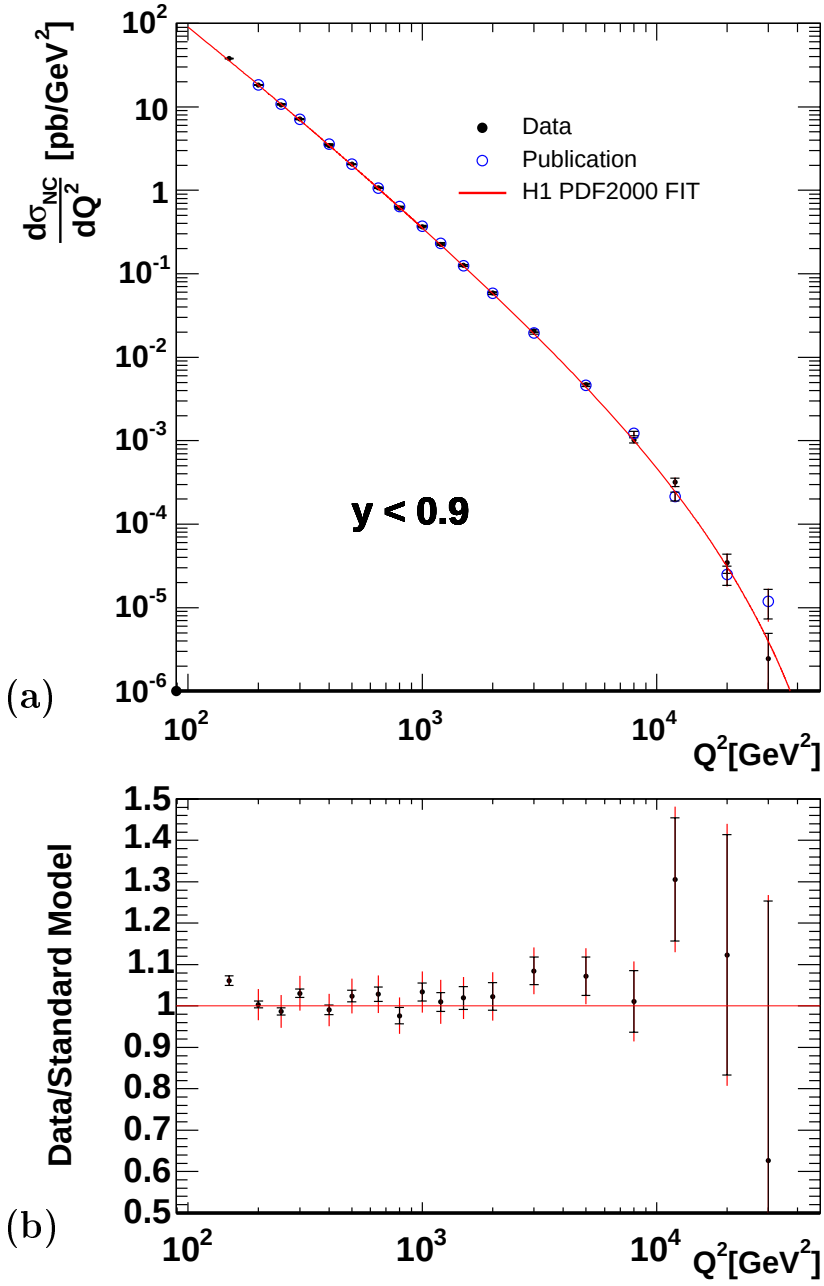

Figure 6.15: *(a) The single differential cross section* $\mathrm{d}\sigma_{NC}/\mathrm{d}Q^2$ *for data, publication and the Standard Model expectation as determined by the H1PDF2000 Fit. Also shown in (b) is the data divided by the SM expectation. Inner error bars represent the statistical error; the full error bars represent the total error obtained by adding the statistical and systematic errors in quadrature.*

Summary

New measurements of inclusive neutral current unpolarized e^+p cross sections have been made using HERAII data collected during the period September 2003 to August 2004. The single differential cross section in Q^2 and the reduced cross section have been presented with quoted systematic uncertainties. The single differential cross section is measured in the range $150 \leq Q^2 \leq 30\ 000$ GeV^2 and consists of 18 data points. The reduced cross section is measured in the range $120 \leq Q^2 \leq 30\ 000$ GeV^2 and $0.002 \leq x \leq 0.65$ and consists of 128 data points.

The results are found to agree with previously published data as well as Standard Model expectation within the uncertainties quoted.

The data selection process was explained and it was ensured that the amount of background in the final sample was kept to an acceptable level. Control plots were used to demonstrate the agreement between data and simulation. However, further study should be continued to understand the vertex reconstruction in both data and simulation.

In the forthcoming years HERA will continue to collect data, in the present mode of operation using an e^- beam, and in about a year's time an e^+ beam. The increase in the amount of collected data will not only reduce the size of the statistical errors in the the cross section measurement, but also lead to further understanding of detector behaviour especially in the forward region where statistics are low. This should help to reduce the systematic uncertainties.

No attempt was made in this thesis to study the dependence of the cross section on polarization. However, this analyis is underway, and will allow tests of the electroweak sector of the Standard Model to be made.

By the time HERA finishes scheduled data-taking in 2007, and the main analyses have finished, it will have provided us with the most complete picture we have of the proton. This knowledge will prove invaluable as the Large Hadron Collider (LHC), colliding proton beams, is scheduled to make its first collisions in 2007.

Appendix A

CIP2k Performance

Measurement of the Efficiency of the
Central Inner Proportonal Chamber (CIP2k) at H1, HERAII

Abstract

The efficiency of the new proportional chamber CIP2k detector was investigated using events where J/ψ candidates decay into two muons. It was found that at most 93.8 percent [1] of the muon tracks produced sufficient hits on the CIP2k to allow their z-Vertex to be reconstructed reliably. Results also indicate a possible misalignment of the CIP2k detector of the order of 0.5 cm in the negative z direction. Regions of the detector that were found to have either a relatively low efficiency or a relatively high noise level have been identified.

A.1 Introduction

The aim of the upgrade of HERA which took place during the years 2000–2002 was to increase the luminosity. However, the rate of background events increased also. To cope with such an anticipated increase in background events, the new Central Inner Proportonal Chamber (hereafter referred to as CIP2k) was installed in the H1 detector during the upgrade, and has replaced the old Central Inner Proportional Chamber (CIP) as well as the Central Inner z-Drift Chamber (CIZ).

CIP2k is used to reconstruct the z-position of the interaction vertex of an event in real time, which is then used in making a level one (L1) trigger decision.

The purpose of this analysis is to investigate the efficiency of the CIP2k detector in effectively identifying tracks for the purpose of making trigger decisions.

[1] Track Efficiency is defined later in the report

Layer	Radius[mm]	Pad Length [mm]	Number of Pads
0	157	18.250	119
1	166	19.322	112
2	175	20.531	106
3	184	21.900	99
4	193	23.464	93

Table A.1: *Radial location and length along the z-axis of the the anode pads. The last pad in Layer 0 (*$\hat{=}$*119), layer 2 (*$\hat{=}$*106) and Layer 4 (*$\hat{=}$*93) have only half the pad size. The total length of the active area is 2710mm.*

A.2 Structure of the CIP2k

The CIP2k is a Multiwire Proportional Chamber (MWPC) that is cylindrical in shape, and located between the Central Silicon Tracker (CST) and the inner Central Jet Chamber (CJC1). It consists of 5 separate layers, the innermost being layer0 and the outermost being layer4. Each layer can be regarded as a separate MWPC. The active length of the CIP2k is 2.2 m.

A sectional view of a typical layer is shown in Figure A.1, as projected onto the r-z plane. The chamber is formed between the inner and outer cathodes, and filled with argon-isobutane gas. The anode wire is kept at high voltage ($\approx$ 2 KV). When a charged particle crosses the chamber, the positive ions formed migrate towards the cathodes. The outer cathode, referred to hereafter as the Readout Cathode, is made of Capton-Foil sandwiched between a Carbon coating and Copper pads. These pads are the readout pads, which serve to transmit the accumulated postive charges to the readout electronics where a signal is registered. This signal can then constitute a hit corresponding to the specific pad.

Each of the 5 layers is divided into 16 equal ϕ-sectors (each subtending 22.5° at the detector axis). Each ϕ-sector is made up of the readout pads mentioned above, which are arranged in the z-directon. The CIP2k is designed such that the length of the pads in z increases with layer number (thus the *number* of pads per layer decreases with layer number). The pad dimensions and numbers are summarized in Table A.1.

A.3 Method

Data Set and Event Selection

The events used in this analysis are taken from 2004 data, specifically from the H1oo Data Set: acs/data/oo-2.5/online04/mods.2.5.10.dst1.c0401407-498.root

The following cuts were made on the events:

1. Number of Diffractive J/ψ 's = 1
2. Absolute value of z-Vertex less than 35 cm
3. Require at least 1 High Quality Muon[2]
4. Reject events with one track having High Muon Quality and the other having High Electron Quality
5. Number of Central Tracks = 2
6. Number of DTNV (Non-Vertex Fitted Tracks) Tracks = 2
7. Delta ϕ between the two tracks $\geqslant 90^\circ$
8. Reject Cosmic ray muons using the IsCosmic() function[3]. A candidate 2 muon event is classified as cosmic if one or more of the following is satisfied:

$$\chi^2 < 10 \tag{A.1}$$

$$|DCA_{Track1}| > 0.1cm \&\& |DCA_{Track2}| > 0.1cm \tag{A.2}$$

$$|TZero_{Track1} - TZero_{Track2}| > 12 \tag{A.3}$$

9. Invariant Mass of the J/ψ candidate measured between 2.9 GeV/c^2 and 3.3 GeV/c^2.

A total of 441 events survived the cuts.

Hit Association Algorithm

The CIP2k hits were associated to the tracks in the following way. The three closest ϕ-sectors to a given track were associated to the track, and were defined as Associated ϕ-sectors. If on a given layer a hit was found on any ϕ-sector directly adjacent to any Associated ϕ-sector, then that ϕ-sector became an Associated ϕ-sector as well. This procedure when repeated produced a Set of Associated ϕ-sectors on a particular layer for each track. Any hit found on a ϕ-sector in the Set of Associated ϕ-sectors was associated to the said track[4]. Note that if the two Sets of Associated ϕ-sectors for the two tracks on any layer

[2] *High* defined as Quality $\geqslant 2$ for Muon Quality

[3] See the *H1FindJPsi* class in H1oo

[4] For the moment no cut is applied in z to associate hits to tracks. *Good* hits will be defined later for the purpose of calculating efficiencies (see *Section* A.5)

overlapped, then the event (called an Unassociable Event) was not used in determining residuals (see *Section* A.4).

Using this algorithm, out of the 441 events that survived the cuts, 15 events were found to be Unassociable Events. Out of the remaining 426 events, there was a total of 17320 CIP2k hits, out of which 81.4 percent (14101) were associated to tracks.

Figure A.2 shows the hits associated to Track1 and hits associate to Track2, both relative to Track1 [5] for the 5 layers. As can be seen, the hits associated to Track1 and the hits associated to Track2 are quite separated, showing that there is very little chance of misassociating a hit to the wrong track.

Figure A.3 shows the distribution of Number of Associated Hits per track, for each layer.

A.4 Results

Residuals

The residual of each hit was calculated according to:

residual = (z-coordinate of Hit) - (z-coordinate of Track)

The distributions of the residuals for each layer were found. These were then used to generate the distribution of the residuals for the CIP2k detector. The results are shown in Figure A.4.

The residual distributions are fitted using a fit function comprising of a gaussian plus a constant. Explicitly the fit is of the form:

$$f(x; P_1, P_2, P_3, P_4) = \frac{P_1}{P_3\sqrt{2\pi}} e^{-\frac{1}{2}\left(\frac{x-P_2}{P_3}\right)^2} + P_4$$

where the P_is are 4 free parameters. The mean μ and width σ are then P_2 and P_3 respectively.

It can be seen that all of the layers have a positive mean of the order of 0.5 cm. One explanation for this shift is that the CIP2k detector is misaligned in the negative z-direction. The width σ is $\simeq 2$ cm for all layers.

Results show no indication of a misalignment in ϕ.

Layer Efficiency and Noise

In order to distinguish between a hit that came from a pad close to the track and one that may have originated from background, *good* hits are defined using the residual distribution

[5] The two tracks were labelled Track1 and Track2 by the H1oo JPsi Finder

of the detector. A good hit was chosen to be any hit whose residual was between 0.5696 $\pm$ 8.0 cm. Figure A.5 shows the distribution of number of good hits per track, for each layer.

The efficiency in ϕ and in z for each layer (defined as the percentage of tracks that pass through a given region with at least one good hit) was determined and is shown in Figure A.6. Also shown in Figure A.6 is the efficiency in ϕ. From these plots, it can be seen that several *holes* exist, i.e regions where the efficiency is very low or zero. These holes are closely associated to particular ϕ sectors of the various layers.

The residual distribution for the various layers taken over a much larger range in z is shown in Figure A.7. Compared to the other layers, Layer 2 had a much larger level of noise. It can be shown that the ϕ-sector corresponding to 281.25° of Layer 2 is largely responsible for the unusually heavy noise of that layer.

Detector Efficiency

For the purpose of defining and calculating the CIP2k Detector Efficiency η_{CIP2k}, a *good* layer for a particular track was defined as one where the track had at least 1 *good* hit associated to it. A track was then defined as *good* if it was associated to at least n good layers. The Detector Track Efficiency was defined as the percent of tracks that were good. This was found to be 93.8 percent (if n=3) and 66.0 percent (if n=4). Figure A.8 summarizes the distributions used to evaluate η_{CIP2k}.

Finally the efficiency of the CIP2k detector in θ and ϕ was calculated (defined as the percentage of tracks that pass through a given region that are good) and the results are shown in Figure A.8. These efficiencies were calculated using $n = 3$. It can be seen that the low efficiency in ϕ (centred at approximately 50° is mainly due to the individual layer efficiencies of layer 3 and layer 4 in that region).

A.5 Discussion

The residual plots (layer or detector) obtained in this analysis would appear to agree (in terms of direction of mean shift and width with that obtained by Max Christoph Urban for at least one of the ϕ-sectors of a particular layer[6]. It would be interesting to compare the residual distribution in other layers and ϕ-sectors.

In order to properly identify a valid *track pattern* in the CIP2k detector from which a reliable z-Vertex trigger decision can be made, it is normally required that a certain number of layers be hit. This is normally taken to be at least 4 (but can also be 3) [7].

[6]See *The new CIP2k z-Vertex Trigger for the H1 Experiment at HERA* by Max Christoph Urban, pp131, Figure 10.3

[7]See *The new CIP2k z-Vertex Trigger for the H1 Experiment at HERA* by Max Christoph Urban, pp35,74

The efficiency of the detector has been shown in this analysis to depend considerably on whether 3 or 4 layers are required.

A.6 Conclusions

In this analysis, tracks were between 20° and 160° in θ, which means that approximately half of the active area of the detector was used. For this part of the detector one can conclude that the track efficiency is 93.8 percent and 66.0 percent if 3 and 4 layers respectively are required for z-Vertex triggering.

Particular regions of the detector where there was a low efficiency or high noise level have been pointed out.

A.7 Electron Comparison

The residuals and noise levels of the CIP2k detector were subsequently checked using scattered electrons from DIS NC events. The DIS event sample used was the *final sample* (see *Section* 5.6) with the additional cuts:

- Require 1 DTNV Track in event
- Require 1 Lee West Track
- Require 1 Central Track
- Require 1 Electromagnetic particle cadidate.

After all cuts, the sample consisted of 1103 events. All hits were associated to the electron track. The residual plots for the scattered electrons are shown in Figures A.9 andA.10 A.9 Figure A.9 also shows the polar angle distribution of the muon tracks and the scattered electrons (taken from the LAr calorimeter).

Both muon and electron plots agree that the residual width σ is $\approx$ 2.0 cm (comparable to the resolution of a CJC hit). The electron residual plots also indicate a misalignment of the detector in the same direction as indicated in the muon analysis, but less in size. Layer 2 is noisy compared to other layers as seen in both electron and muon plots, Figure A.9. Table A.2 summarizes the comparison between the residuals using muons and scattered electron.

Fit Parameter	Mean μ[cm]	Width σ[cm]
Muons	0.3	2.0
Scattered Electrons	0.8	2.0

Table A.2: *Comparison of the mean μ and width σ of the CIP2k residual distributions determined using muons and scattered electrons.*

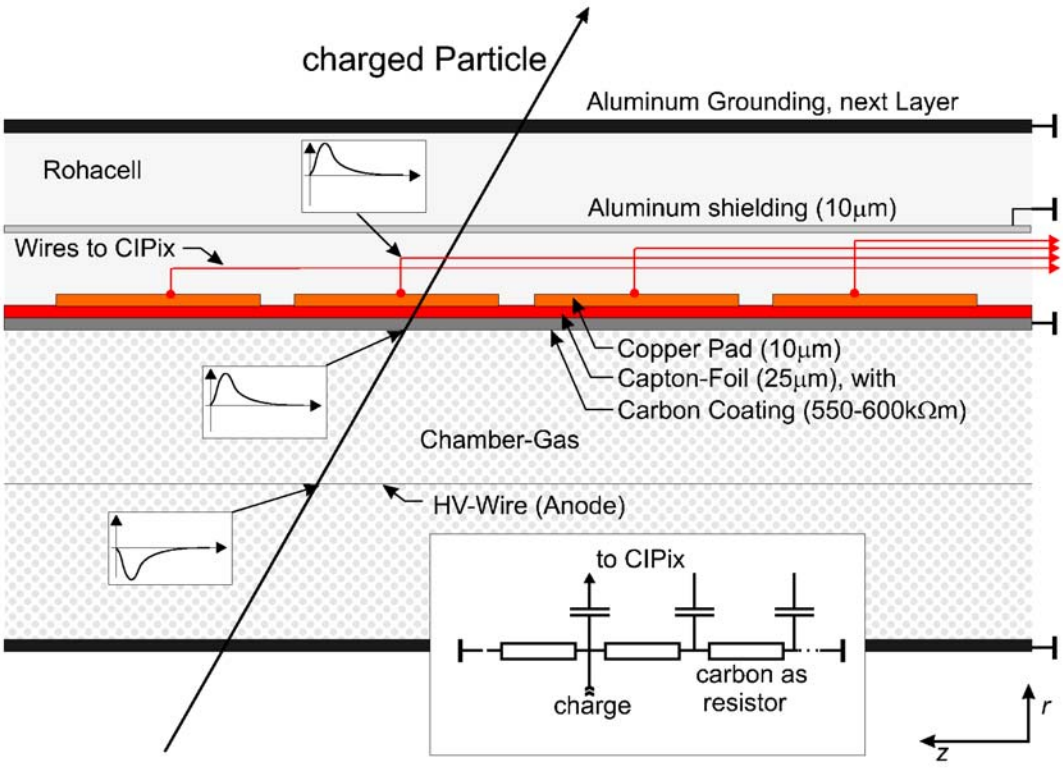

Figure A.1: *Side View of the CIP2k chamber in the rz plane. The charged particle deposits charge that cannot discharge immediately due to the high resistance of the carbon coating on the cathode. Thus a current is induced on the cathode pad near the accumulation of the charge.*

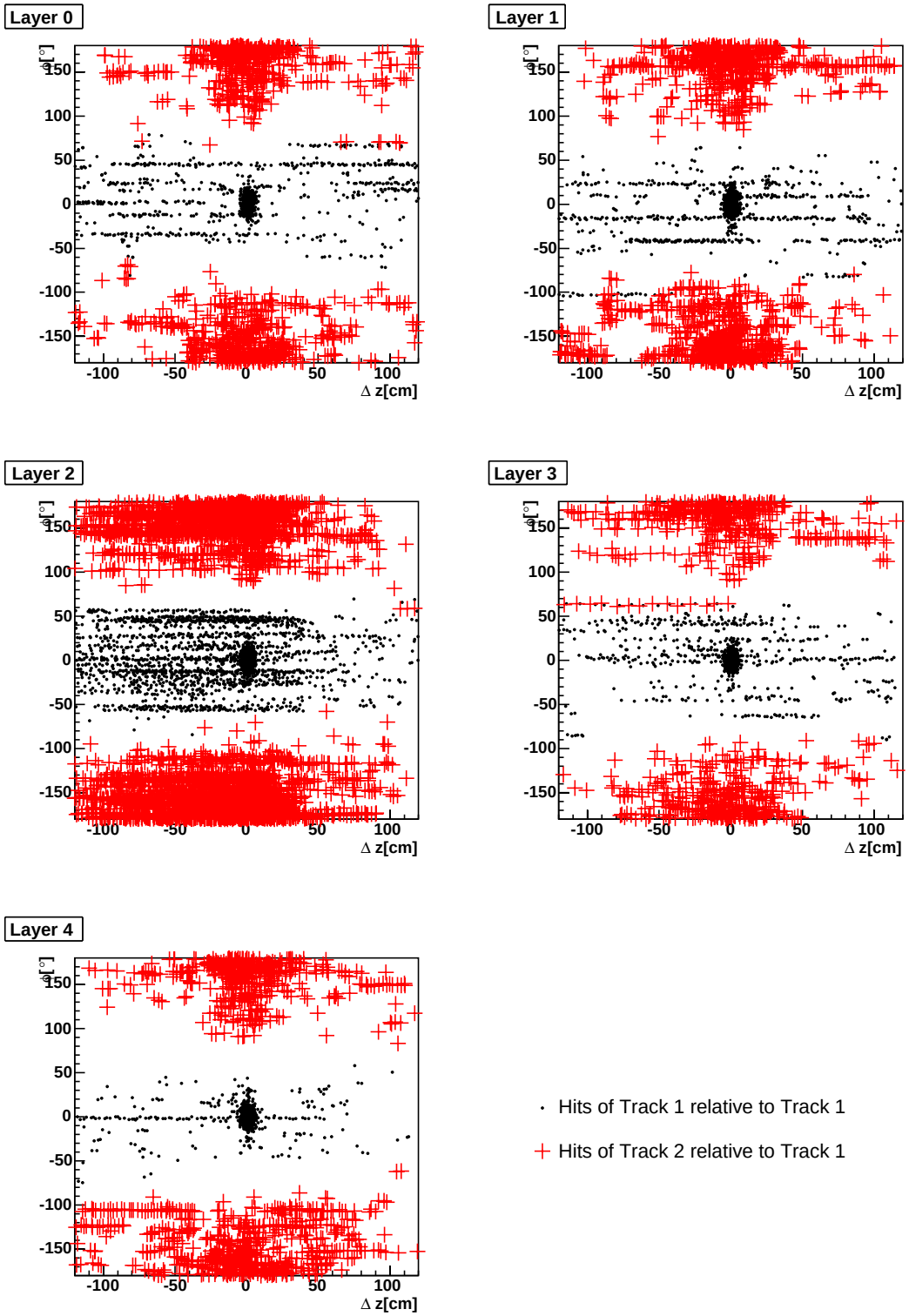

Figure A.2: *The hits associated to each track, relative to Track1, in ϕ and z, for the 5 layers.*

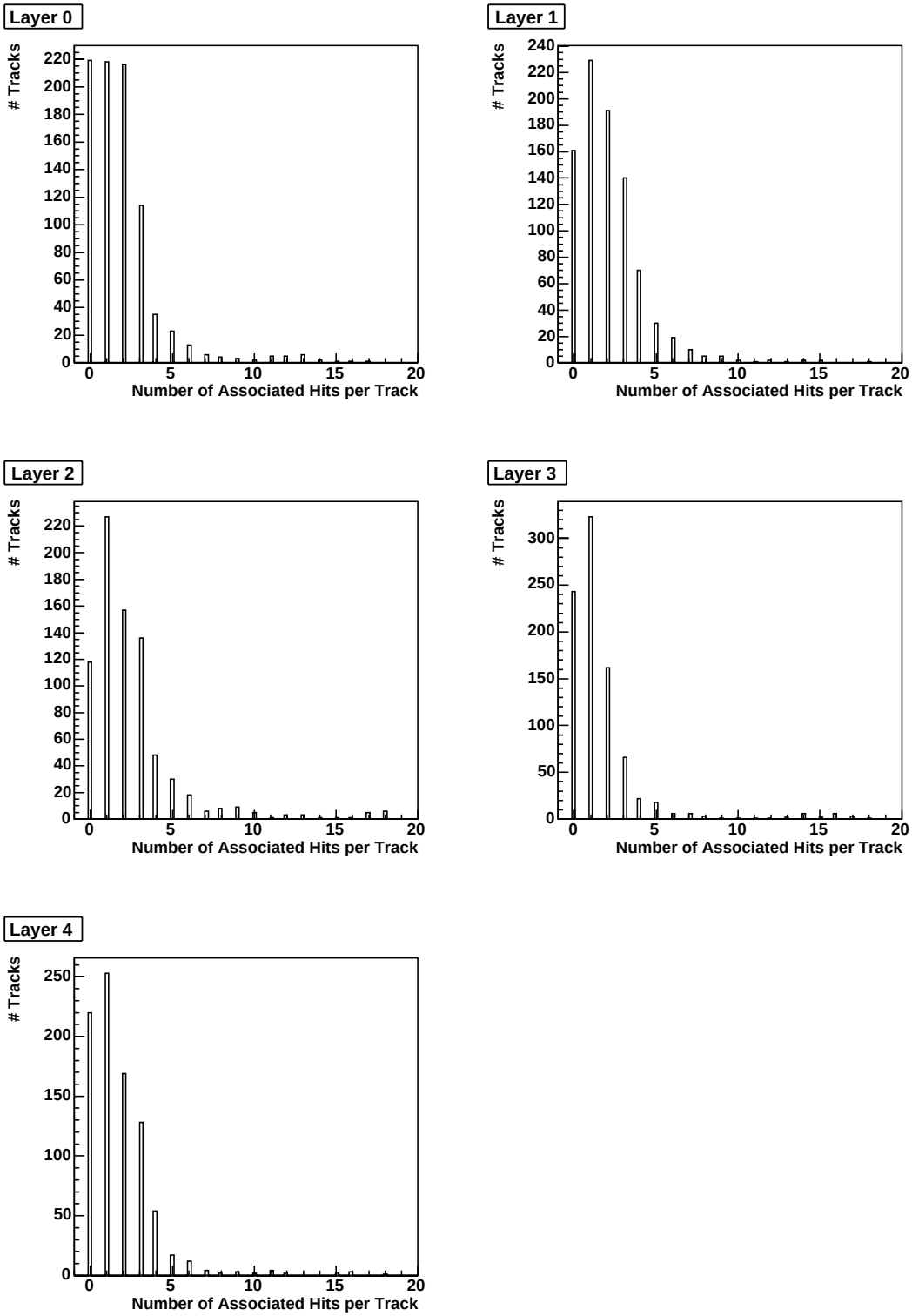

Figure A.3: *Distribution of the number of associated hits per track on each of the 5 layers.*

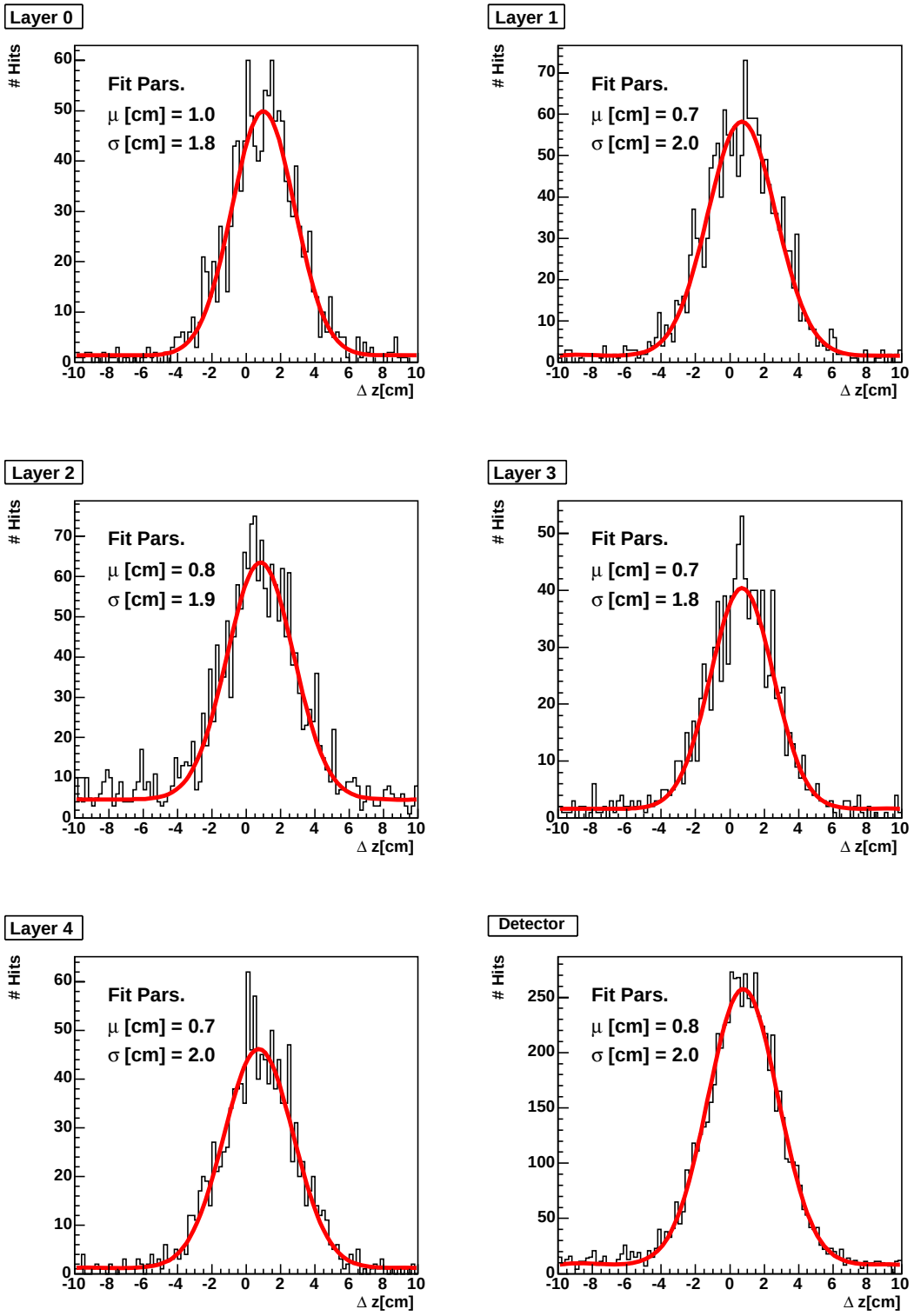

Figure A.4: *The residuals for different layers, then the detector as a whole (all layers taken together).*

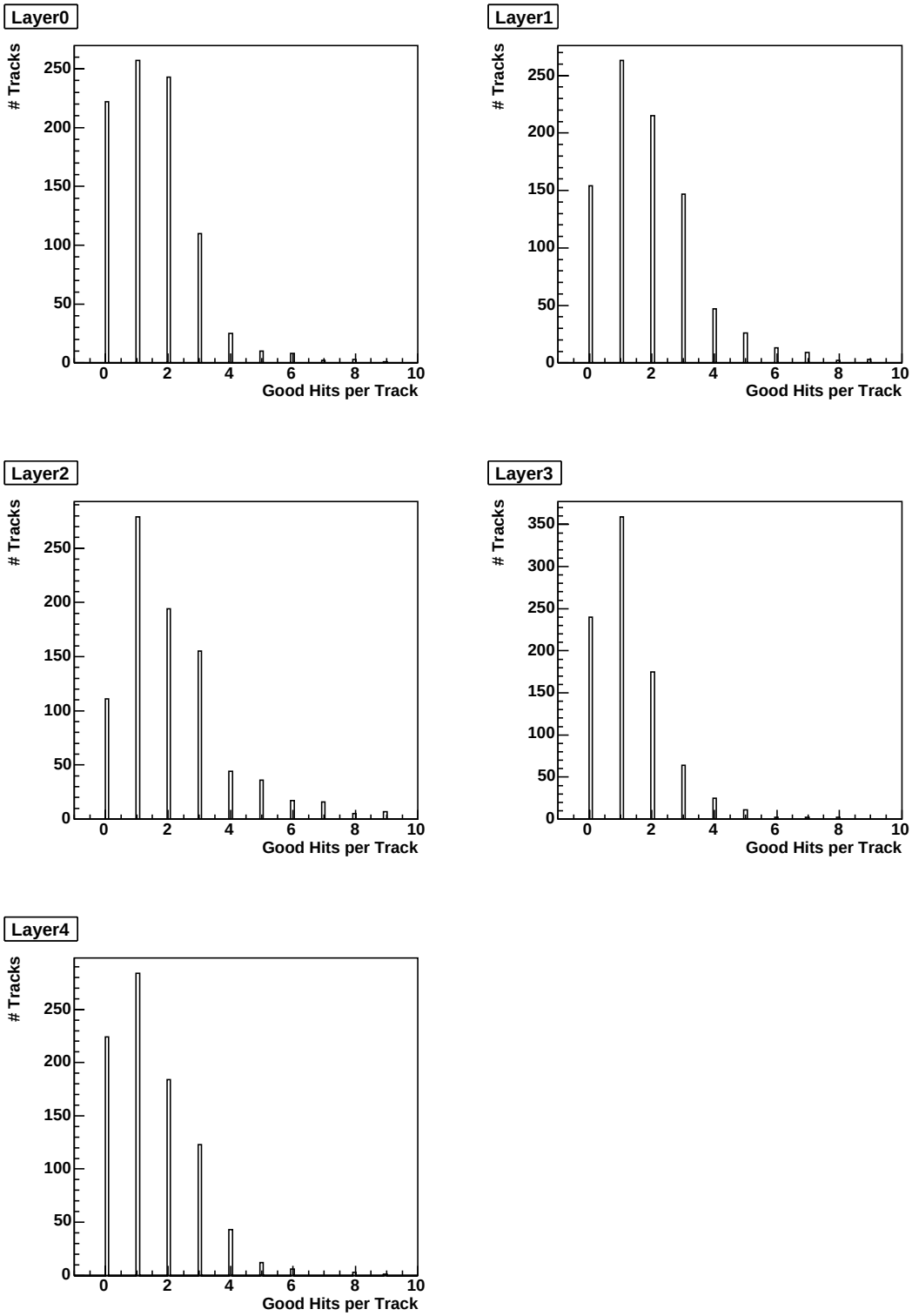

Figure A.5: *The distribution of the number of good hits per track, for each of the 5 layers.*

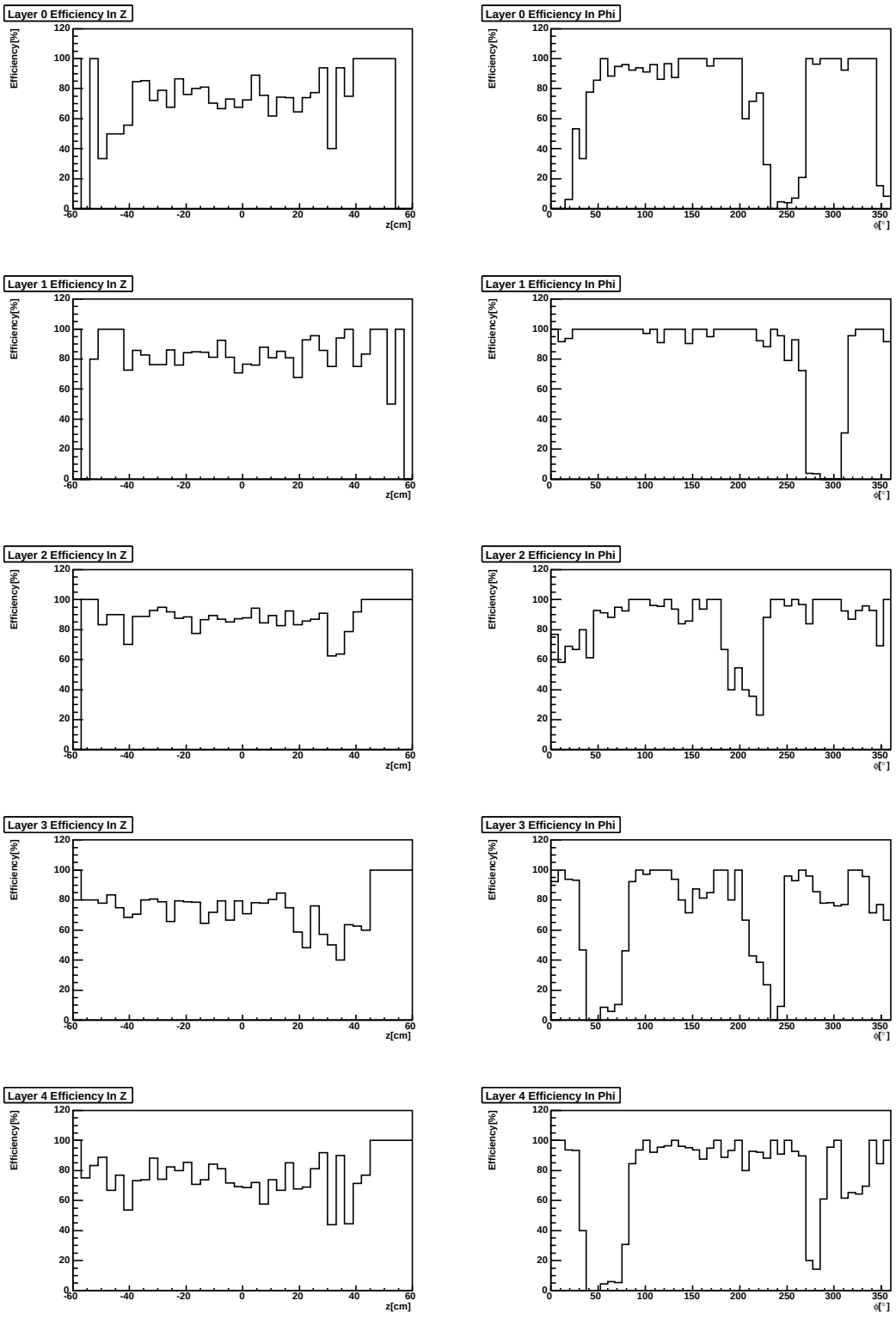

Figure A.6: *Efficiency of the various layers in z and ϕ.*

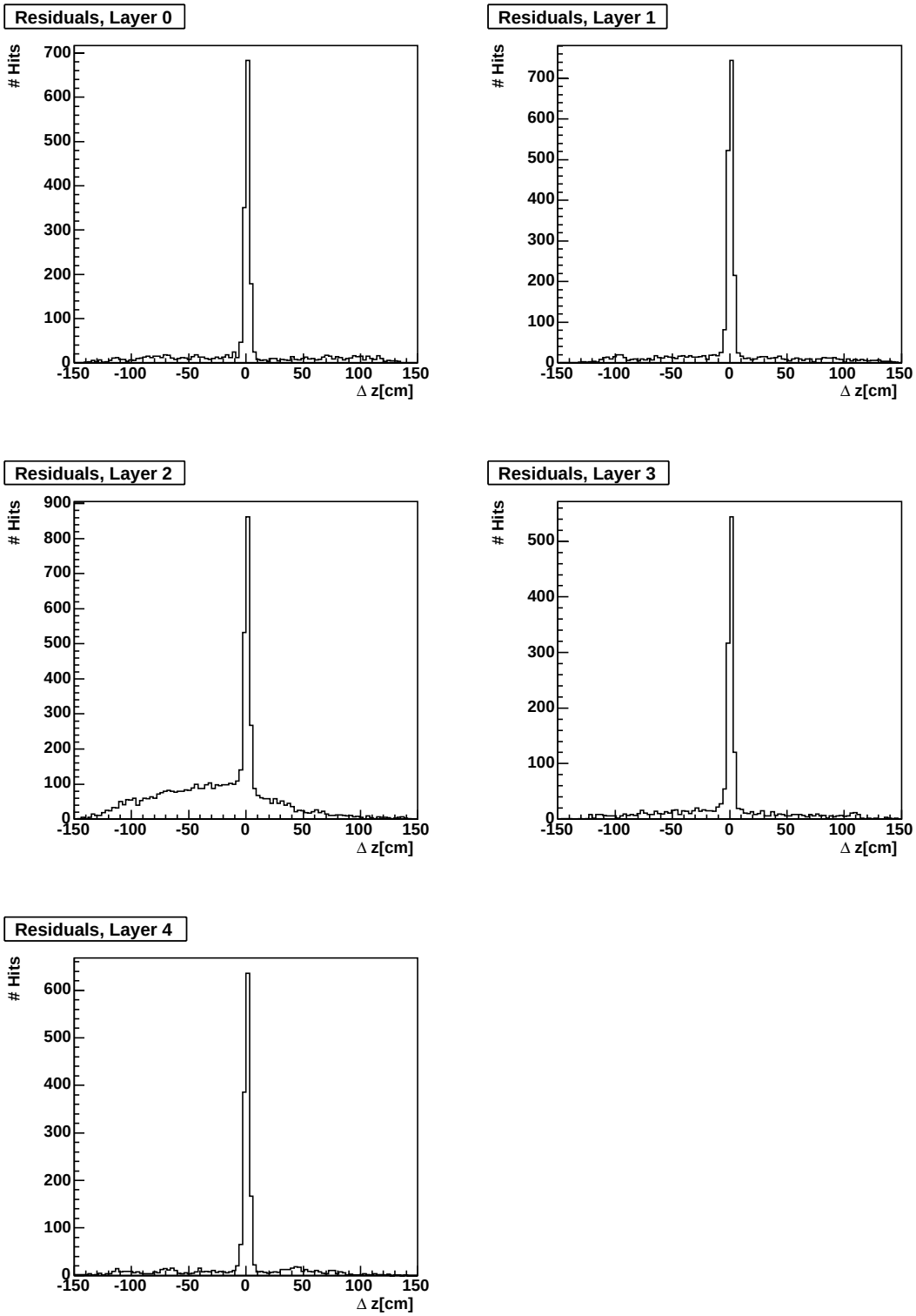

Figure A.7: *The residuals taken over a much wider range in Δz to show the amount of noise present. The unusual high level of noise in Layer 2 is clearly observable.*

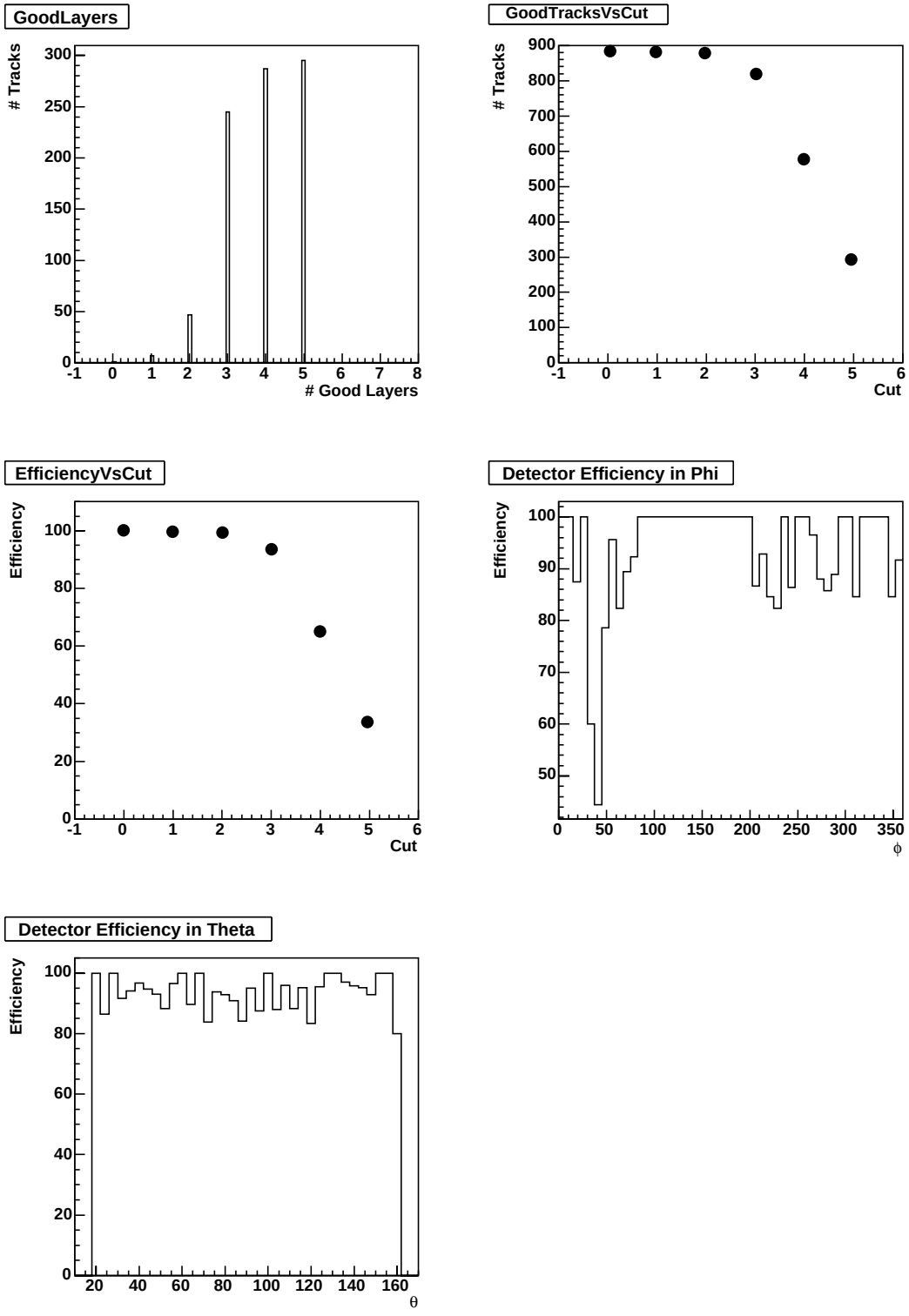

Figure A.8: *Overall Performance of the CIP2k detector.*

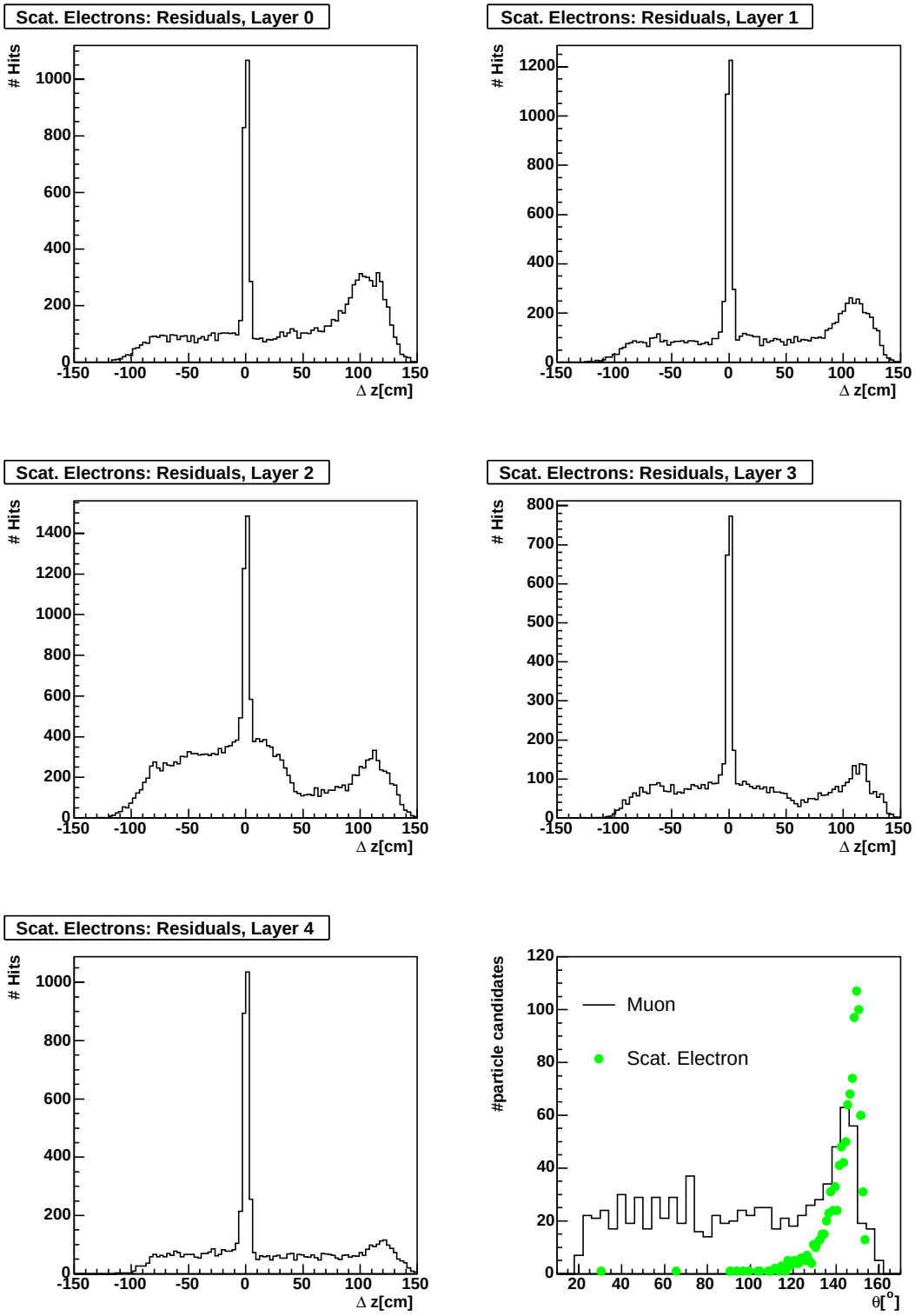

Figure A.9: *CIP2k evaluated using scattered electrons from DIS events: the residuals taken over a much wider range in Δz to show the amount of noise present. The unusual high level of noise in Layer 2 is clearly observable. Compare with muons, Figure A.7. Also shown (last plot) is the polar angle distribution of the muon and scattered electron tracks used to calculate the residuals.*

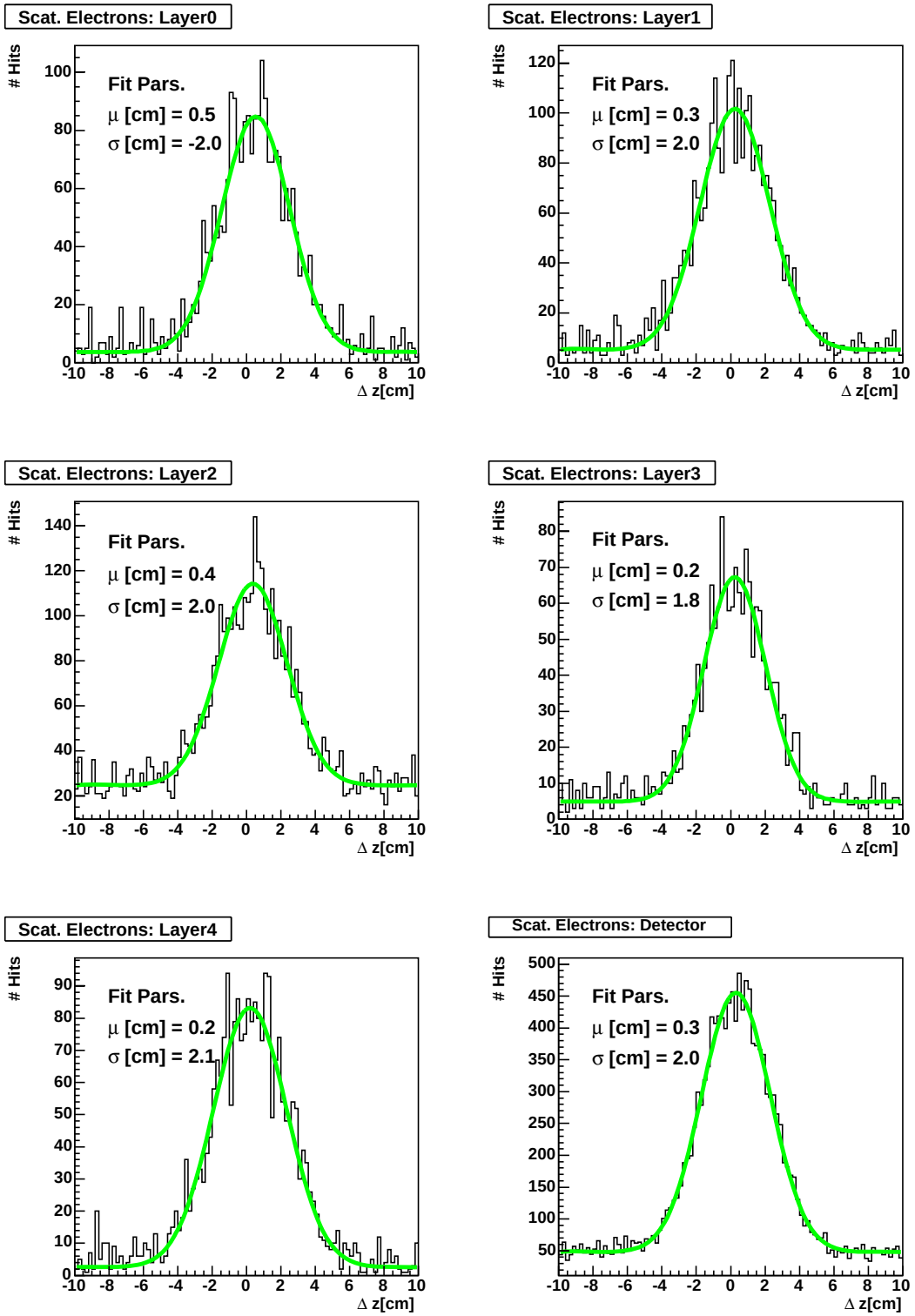

Figure A.10: *CIP2k evaluated using scattered electrons from DIS events: the residuals for different layers, then the detector as a whole (all layers taken together). Compare with muons, Figure A.4.*

Appendix B

Resolution Fits

The following pages contain the plots together with the respective fits used to determine the resolutions presented in chapters 4 and 6.

Generally the fits are made in the following way. First 2.5% of the sample is removed at each tail to reduce effects that may not be due to resolution. A fit comprising of a gaussian plus a constant is then made. Explicitly the fit is of the form:

$$f(x; P_1, P_2, P_3, P_4) = \frac{P_1}{P_3\sqrt{2\pi}} e^{-\frac{1}{2}\left(\frac{x-P_2}{P_3}\right)^2} + P_4$$

where the P_is are 4 free parameters. The mean μ and width σ are then P_2 and P_3 respectively.

Where the fit is poor, then the number of bins is reduced, or the range over which the fit is made is reduced. However the range is chosen to reasonably cover most of the distribution. The only exception to this is the bin corresponding to $Q^2 = 400$ GeV^2 and $x = 0.4$ (see Figure A.17) where the range is deliberately chosen to be very narrow. This is justified considering the behaviour of the surrounding bins.

Unsuccessful fits are indicated with "FIT NOT USED."

The plots are arranged as follows:

- Figure B.1 through Figure B.3 - Resolution of Q^2 using different reconstruction methods. Used in Figures 4.2 and 4.3.
- Figure B.4 through Figure B.6 - Resolution of Q^2 using different reconstruction methods but only using events without initial state radiation. Used in Figure 4.2.
- Figure B.7 through Figure B.9 - Resolution of x using different reconstruction methods. Used in Figures 4.2 and 4.3.
- Figure B.10 through Figure B.12 - Resolution of x using different reconstruction methods but only using events without initial state radiation. Used in Figure 4.2.

- Figure B.13 through Figure B.26 - Resolution of Q^2 and x usng the chosen methods of reconstruction (eΣ) for 2 dimensional bins. Used in Figure 6.1.
- Figure B.27 through Figure B.28 - Resolution of $\frac{E_{e'}}{E_{DA}}$ for data. Used to determine the electron energy calibration in Figures 6.7 and 6.8.
- Figure B.29 through Figure B.30 - Resolution of $\frac{E_{e'}}{E_{DA}}$ for signal MC. Used to determine the electron energy calibration in Figures 6.7 and 6.8.

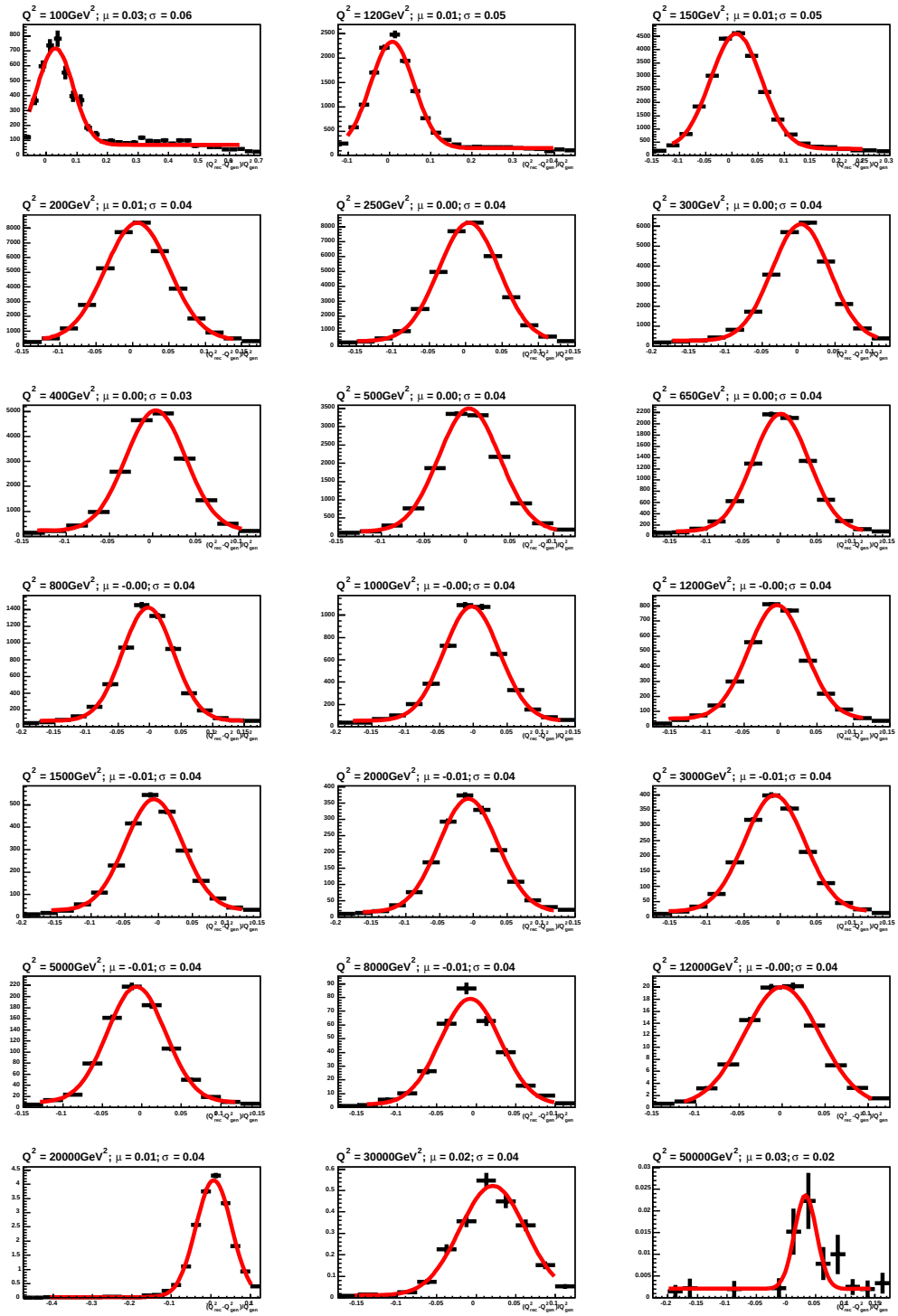

Figure B.1: *The distributions of* $\frac{Q_e^2 - Q_{gen}^2}{Q_{gen}^2}$ *used to determine the resolution of* Q^2 *using the e-method of reconstruction. Each plot corresponds to a particular bin in* Q_{gen}^2.

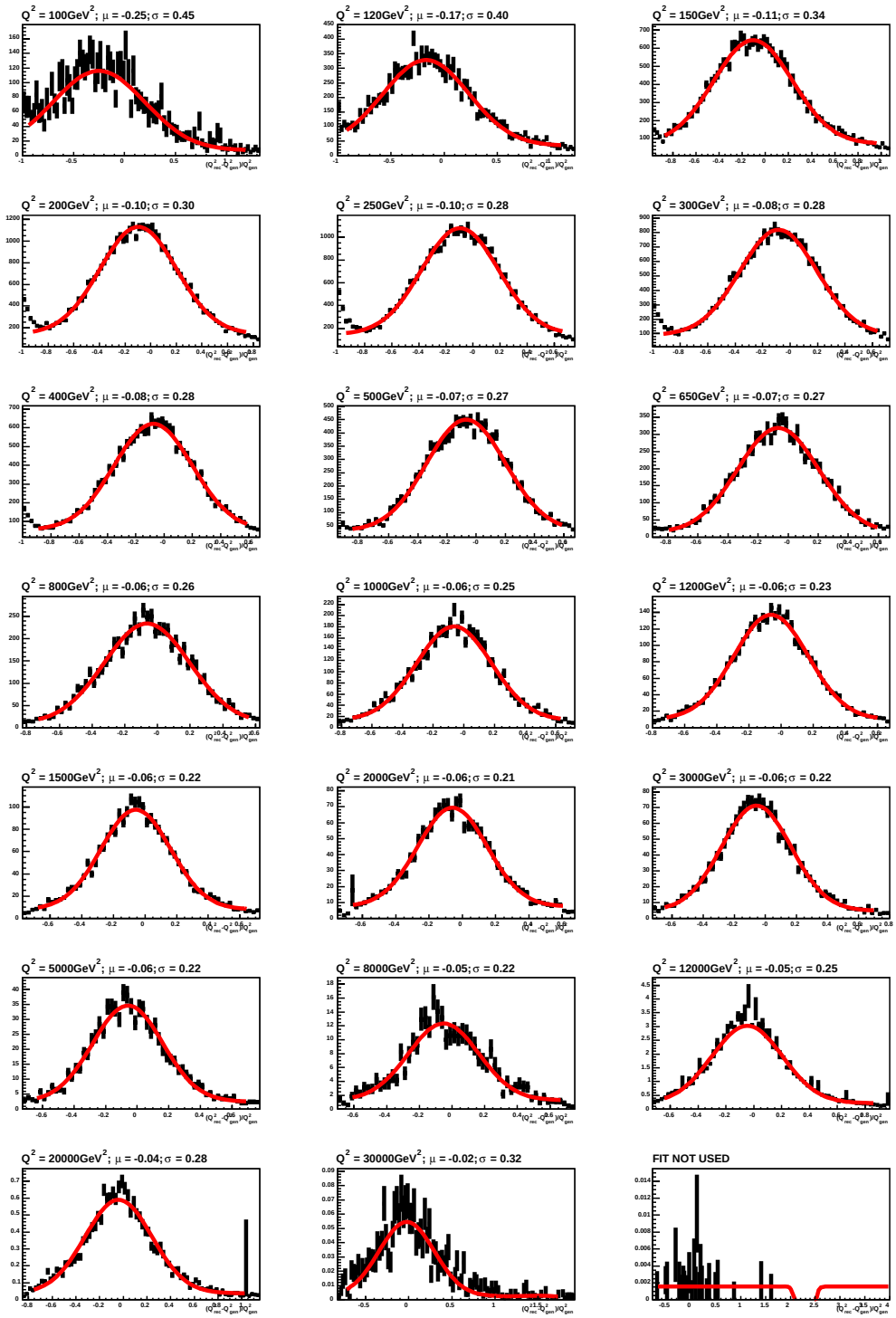

Figure B.2: *The distributions of* $\frac{Q_h^2 - Q_{gen}^2}{Q_{gen}^2}$ *used to determine the resolution of* Q^2 *using the h-method of reconstruction. Each plot corresponds to a particular bin in* Q_{gen}^2.

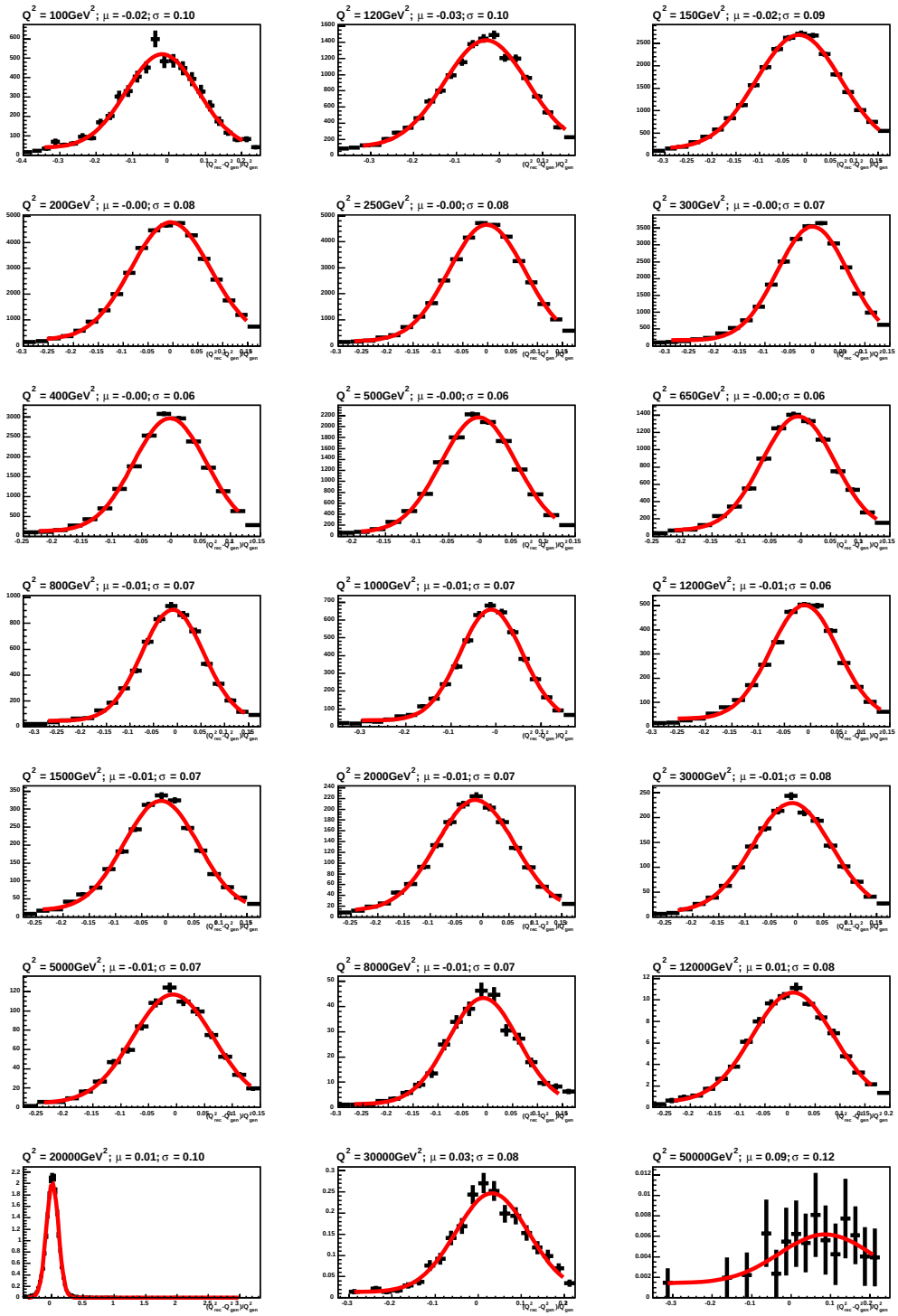

Figure B.3: *The distributions of* $\frac{Q^2_\Sigma - Q^2_{gen}}{Q^2_{gen}}$ *used to determine the resolution of* Q^2 *using the* Σ*-method of reconstruction. Each plot corresponds to a particular bin in* Q^2_{gen}.

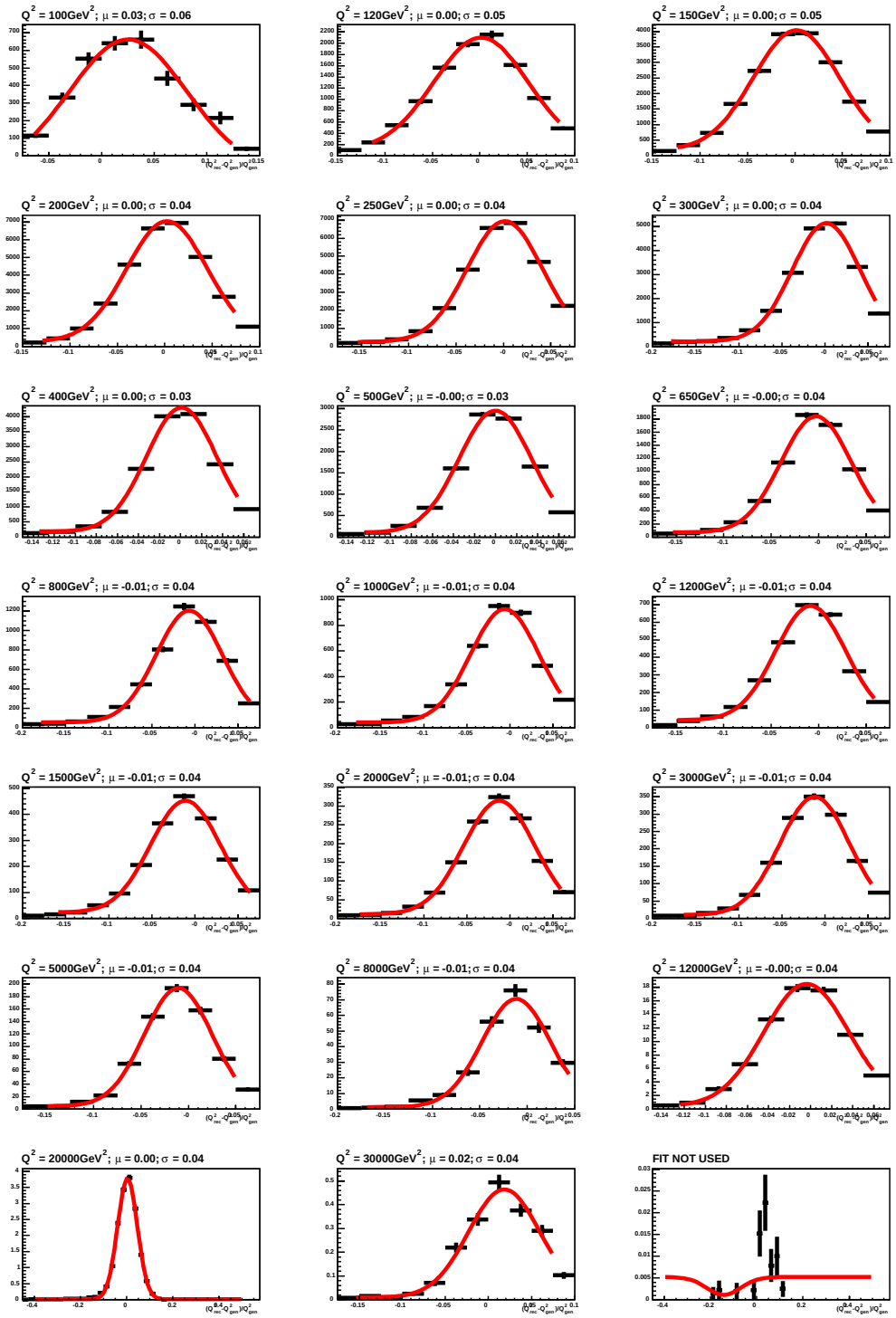

Figure B.4: *The distributions of* $\frac{Q_e^2 - Q_{gen}^2}{Q_{gen}^2}$ *used to determine the resolution of* Q^2 *using the e-method of reconstruction. Here MC events with no initial state radiation are used. Each plot corresponds to a particular bin in* Q_{gen}^2.

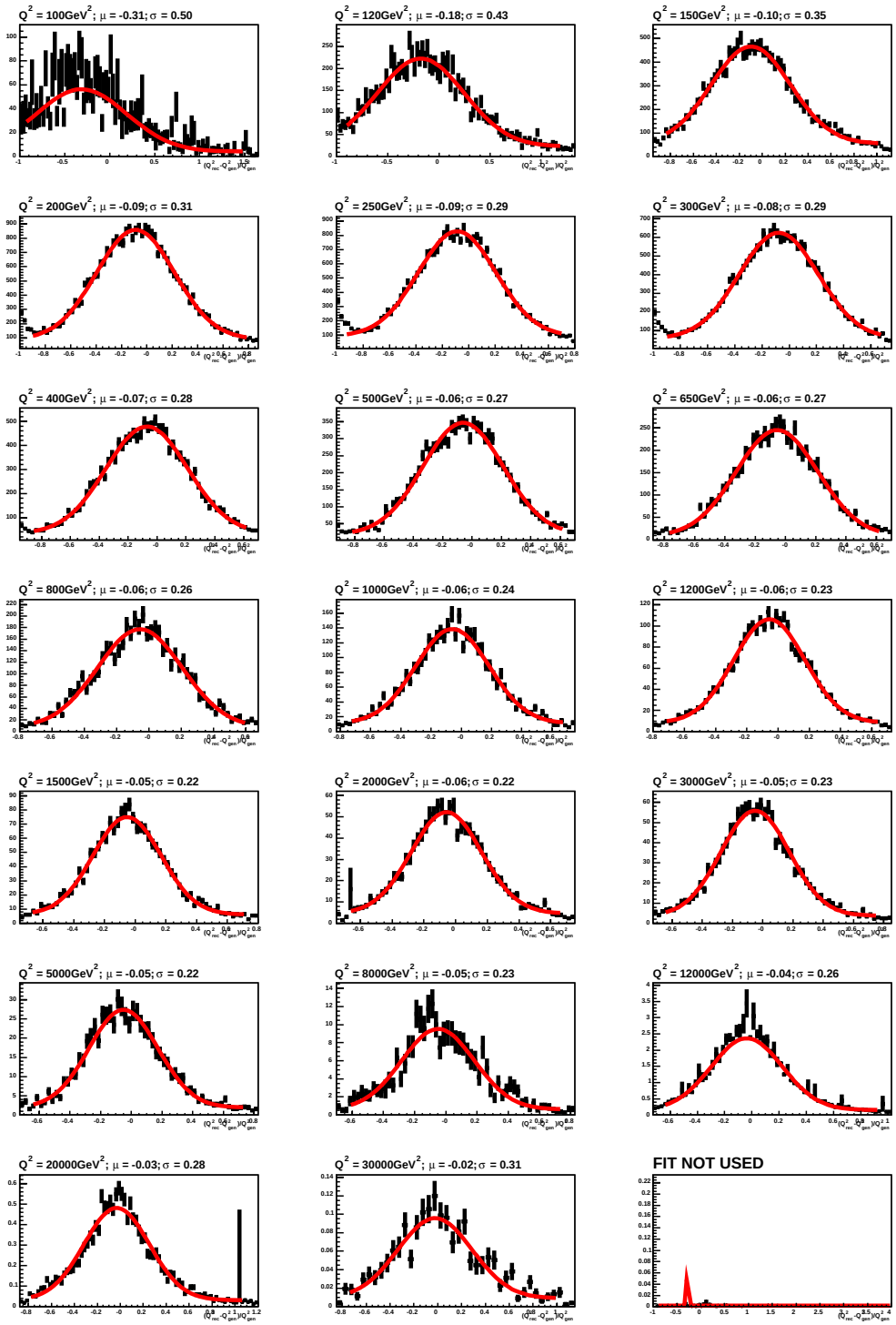

Figure B.5: *The distributions of* $\frac{Q_h^2 - Q_{gen}^2}{Q_{gen}^2}$ *used to determine the resolution of* Q^2 *using the h-method of reconstruction. Here MC events with no initial state radiation are used. Each plot corresponds to a particular bin in* Q_{gen}^2.

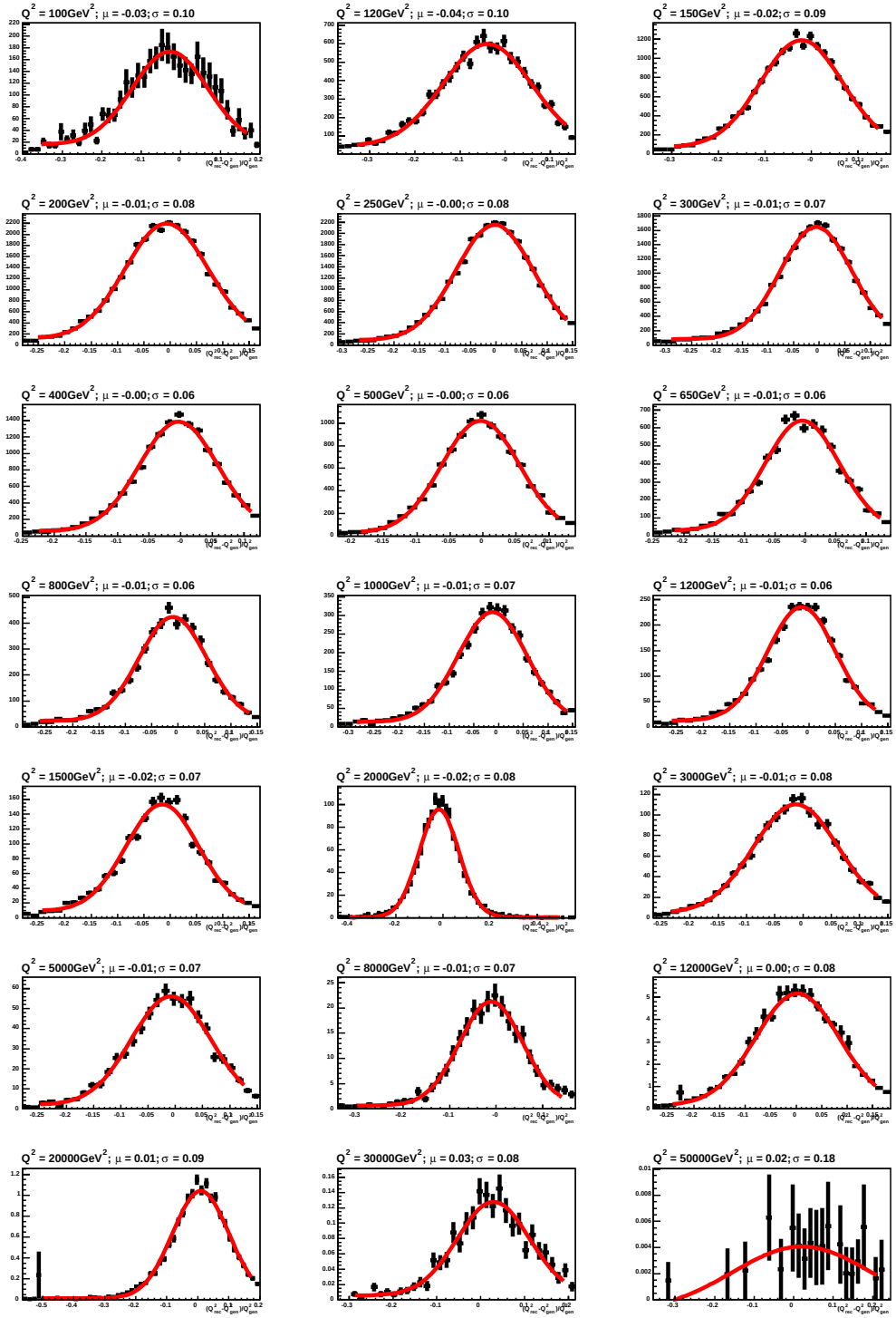

Figure B.6: *The distributions of* $\frac{Q^2_\Sigma - Q^2_{gen}}{Q^2_{gen}}$ *used to determine the resolution of* Q^2 *using the* Σ*-method of reconstruction. Here MC events with no initial state radiation are used. Each plot corresponds to a particular bin in* Q^2_{gen}*.*

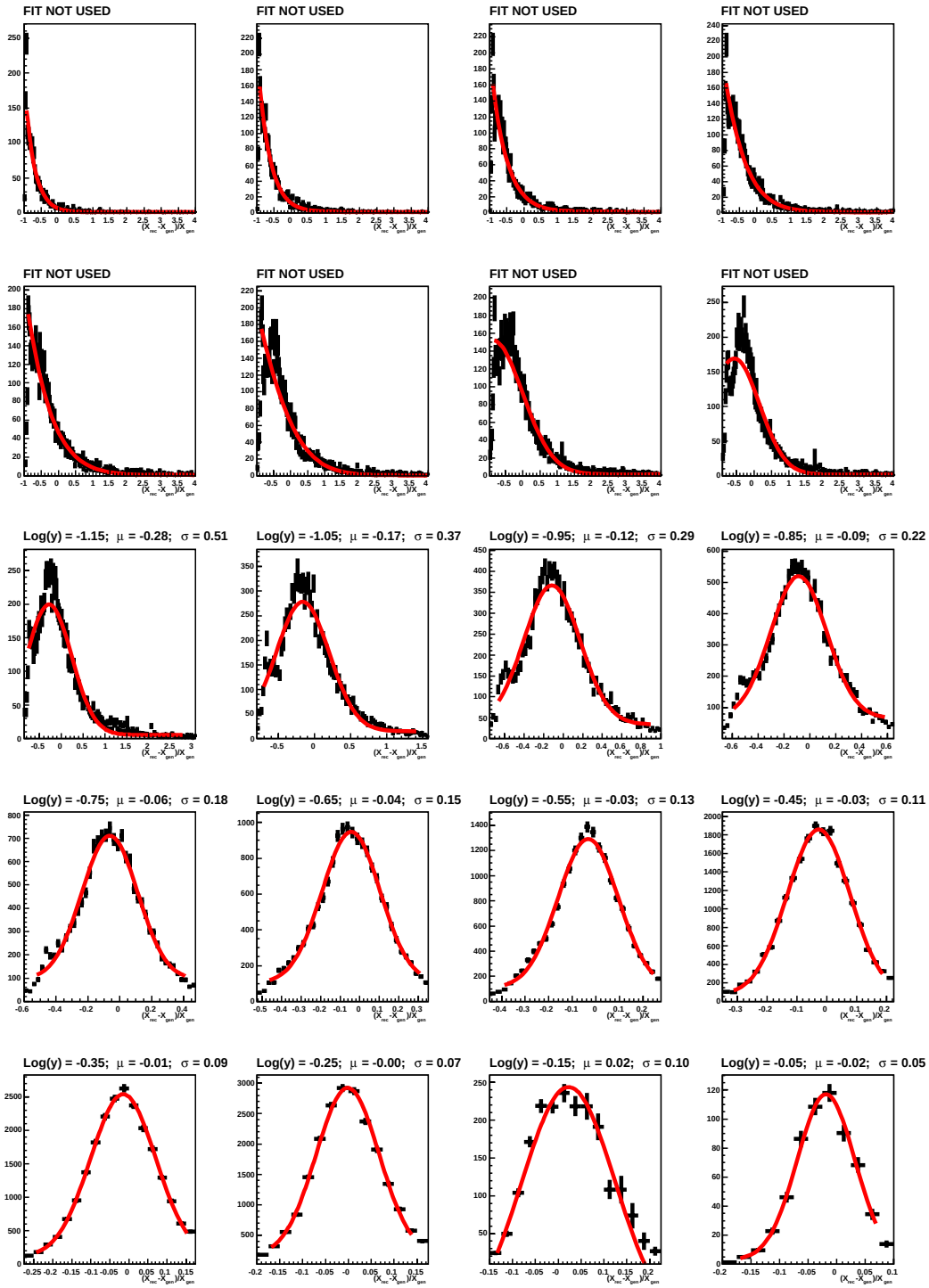

Figure B.7: *The distributions of* $\frac{x_e - x_{gen}}{x_{gen}}$ *used to determine the resolution of* x *using the e-method of reconstruction. Each plot corresponds to a particular bin in* y_{gen}.

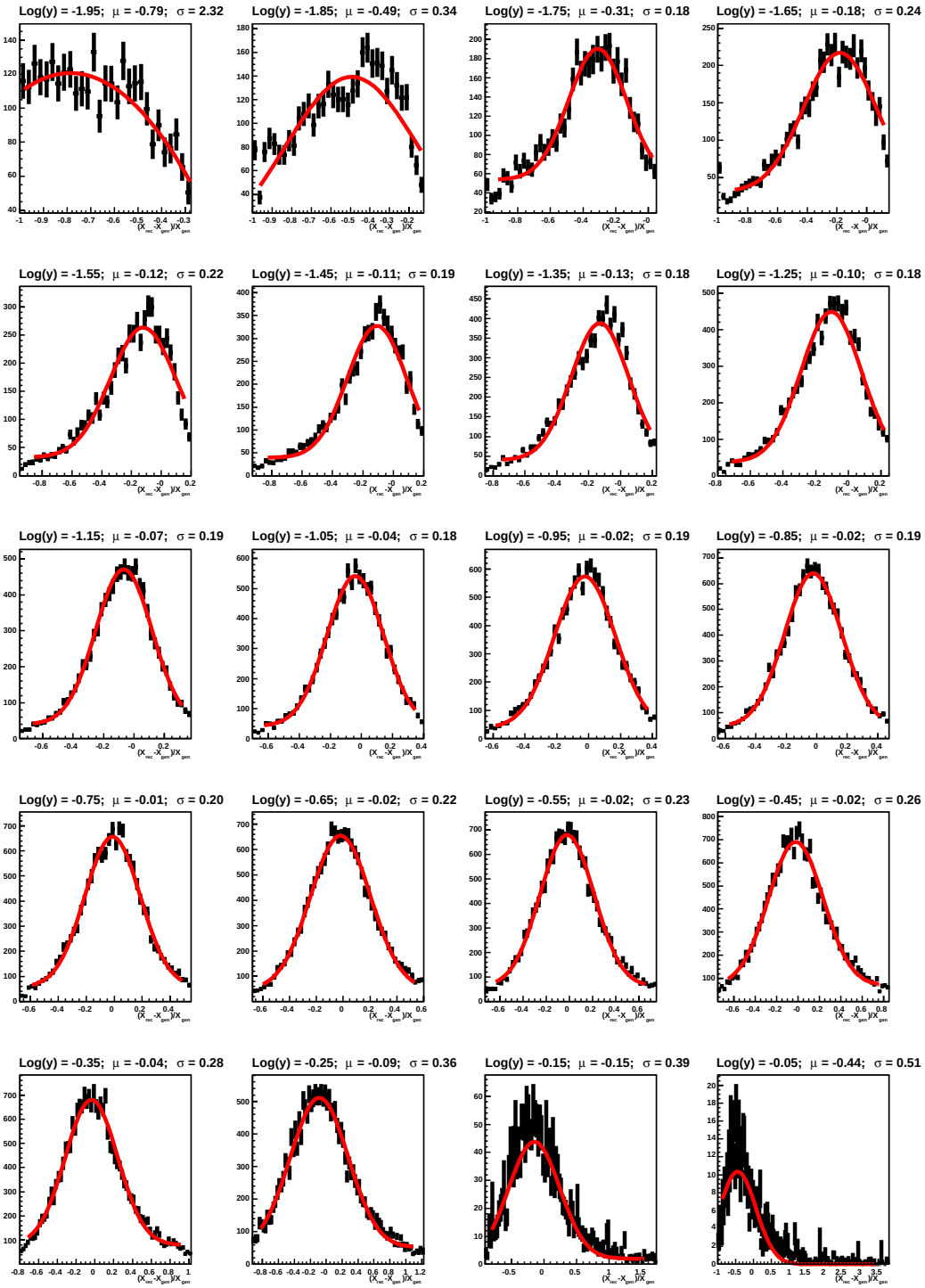

Figure B.8: *The distributions of* $\frac{x_h - x_{gen}}{x_{gen}}$ *used to determine the resolution of* x *using the h-method of reconstruction. Each plot corresponds to a particular bin in* y_{gen}.

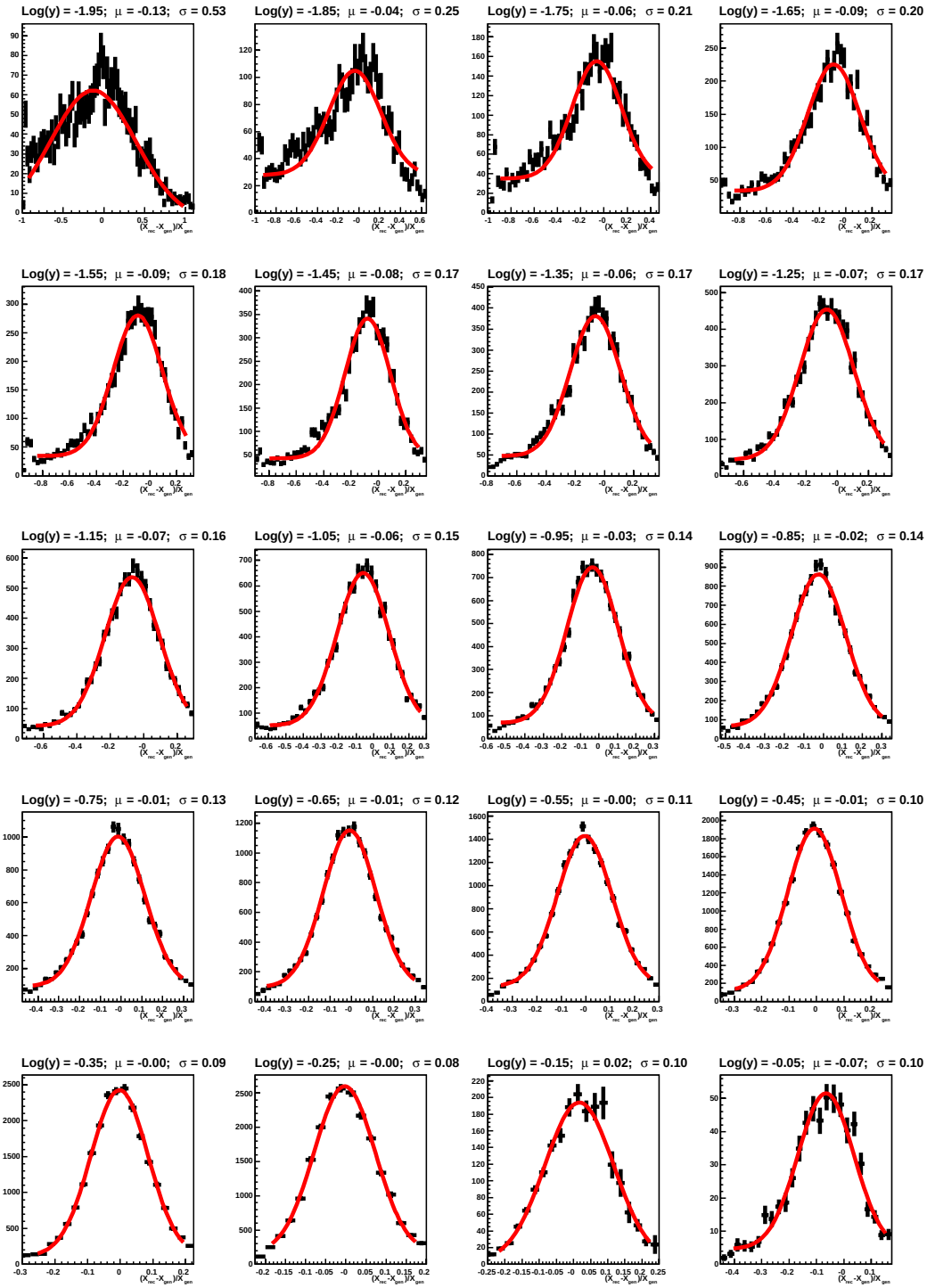

Figure B.9: *The distributions of* $\frac{x_\Sigma - x_{gen}}{x_{gen}}$ *used to determine the resolution of* x *using the* Σ*-method of reconstruction. Each plot corresponds to a particular bin in* y_{gen}.

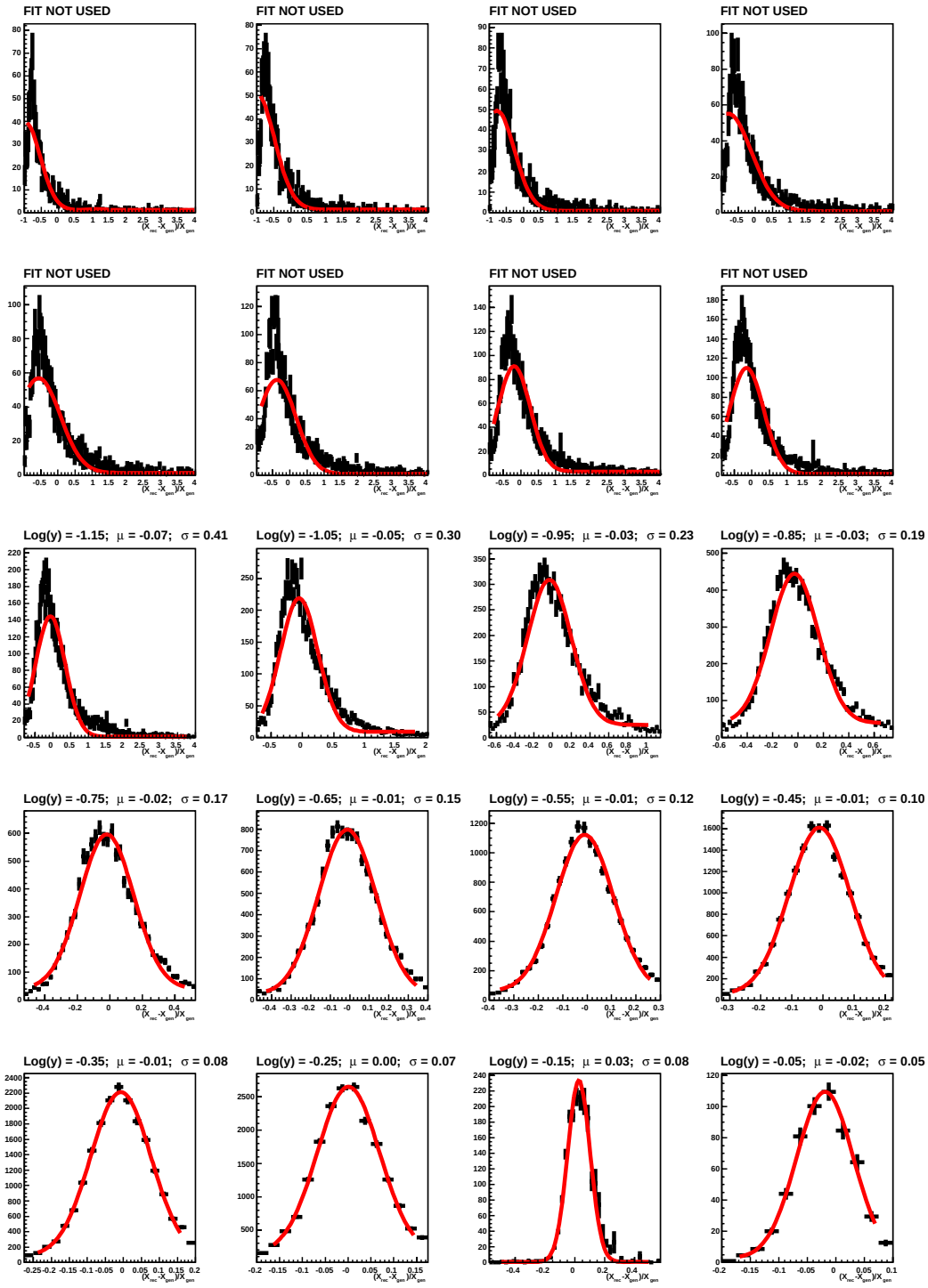

Figure B.10: *The distributions of* $\frac{x_e - x_{gen}}{x_{gen}}$ *used to determine the resolution of* x *using the e-method of reconstruction. Here MC events with no initial state radiation are used. Each plot corresponds to a particular bin in* y_{gen}.

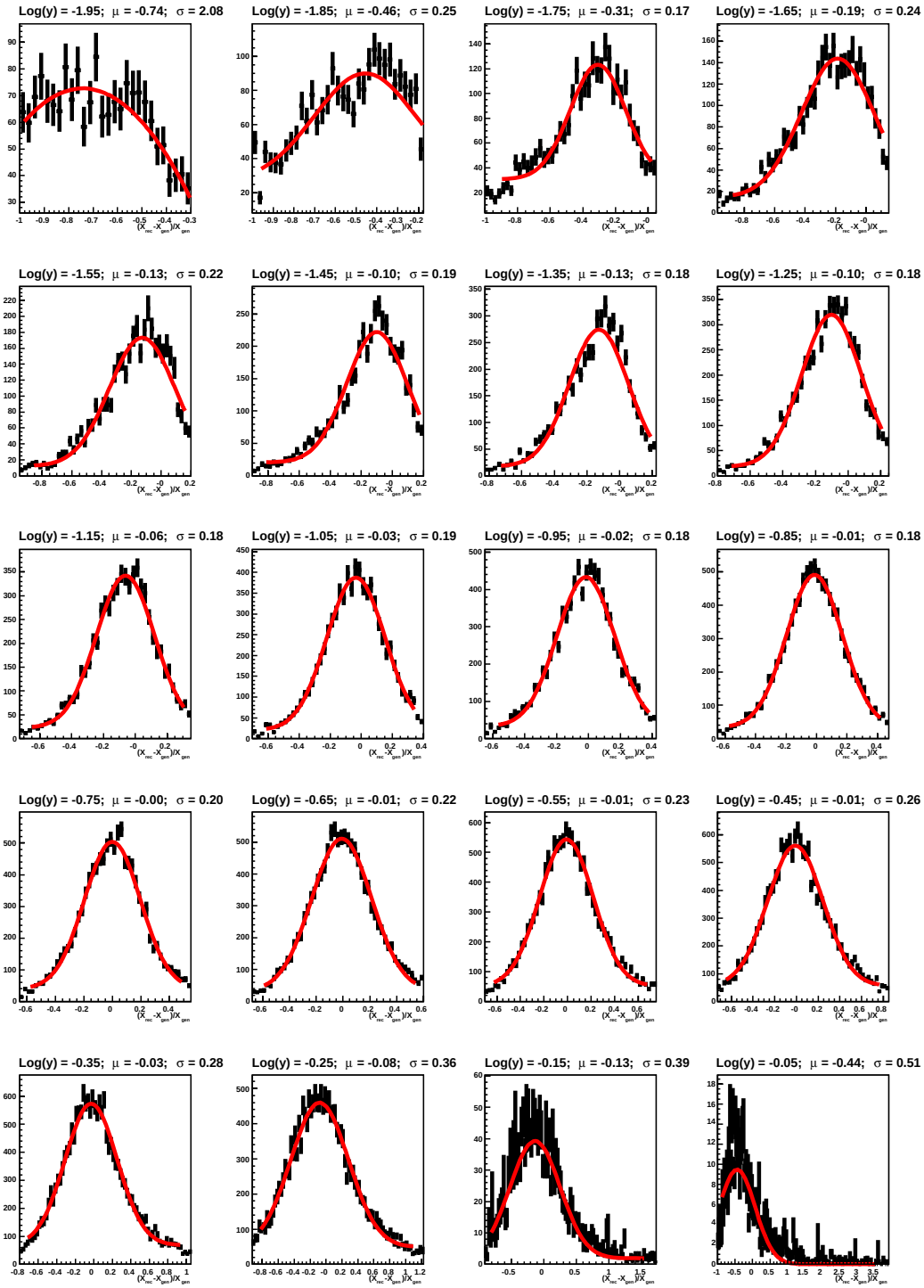

Figure B.11: *The distributions of* $\frac{x_h - x_{gen}}{x_{gen}}$ *used to determine the resolution of* x *using the h-method of reconstruction. Here MC events with no initial state radiation are used. Each plot corresponds to a particular bin in* y_{gen}.

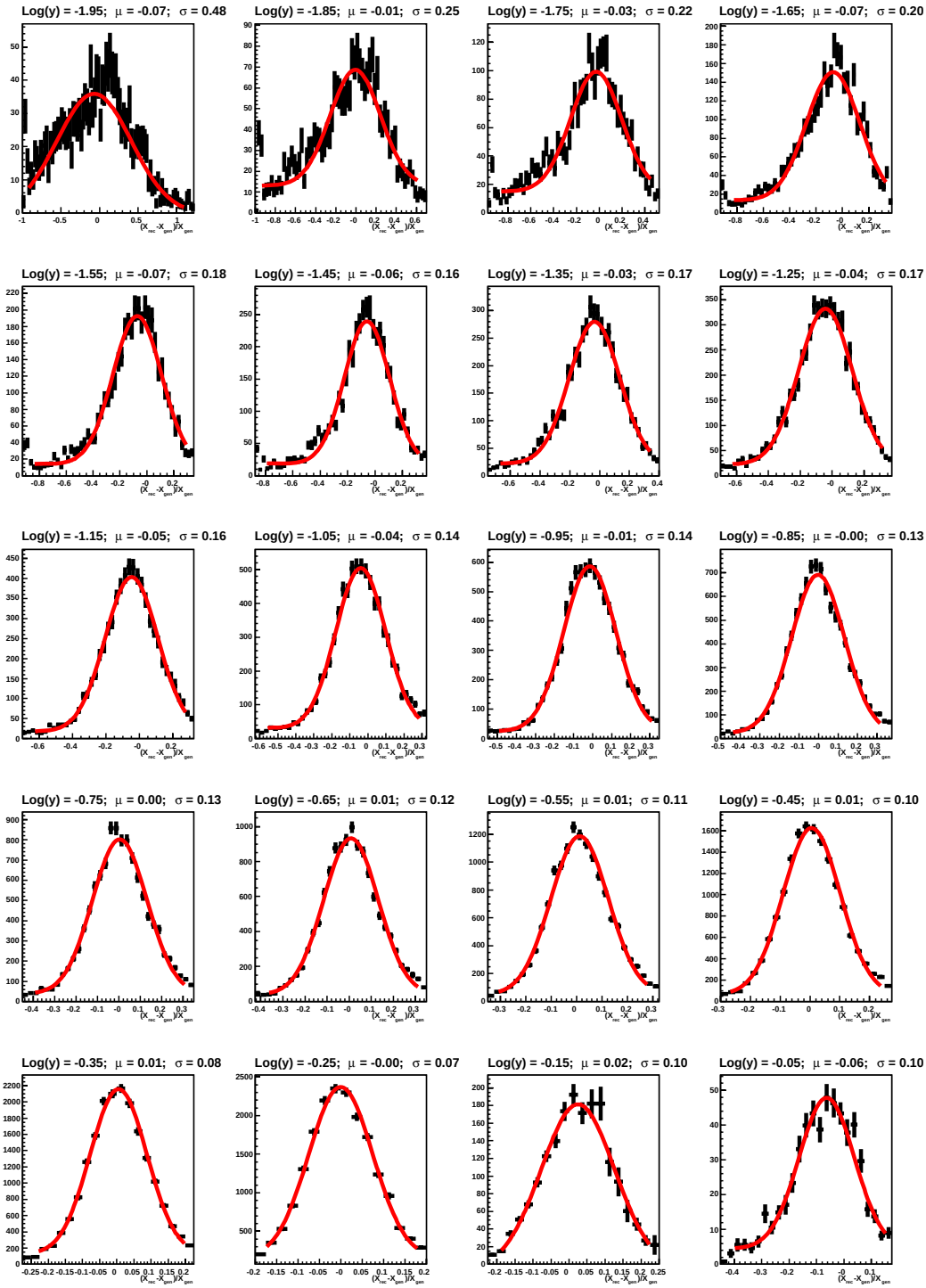

Figure B.12: *The distributions of* $\frac{x_\Sigma - x_{gen}}{x_{gen}}$ *used to determine the resolution of* x *using the* Σ*-method of reconstruction. Here MC events with no initial state radiation are used. Each plot corresponds to a particular bin in* y_{gen}*.*

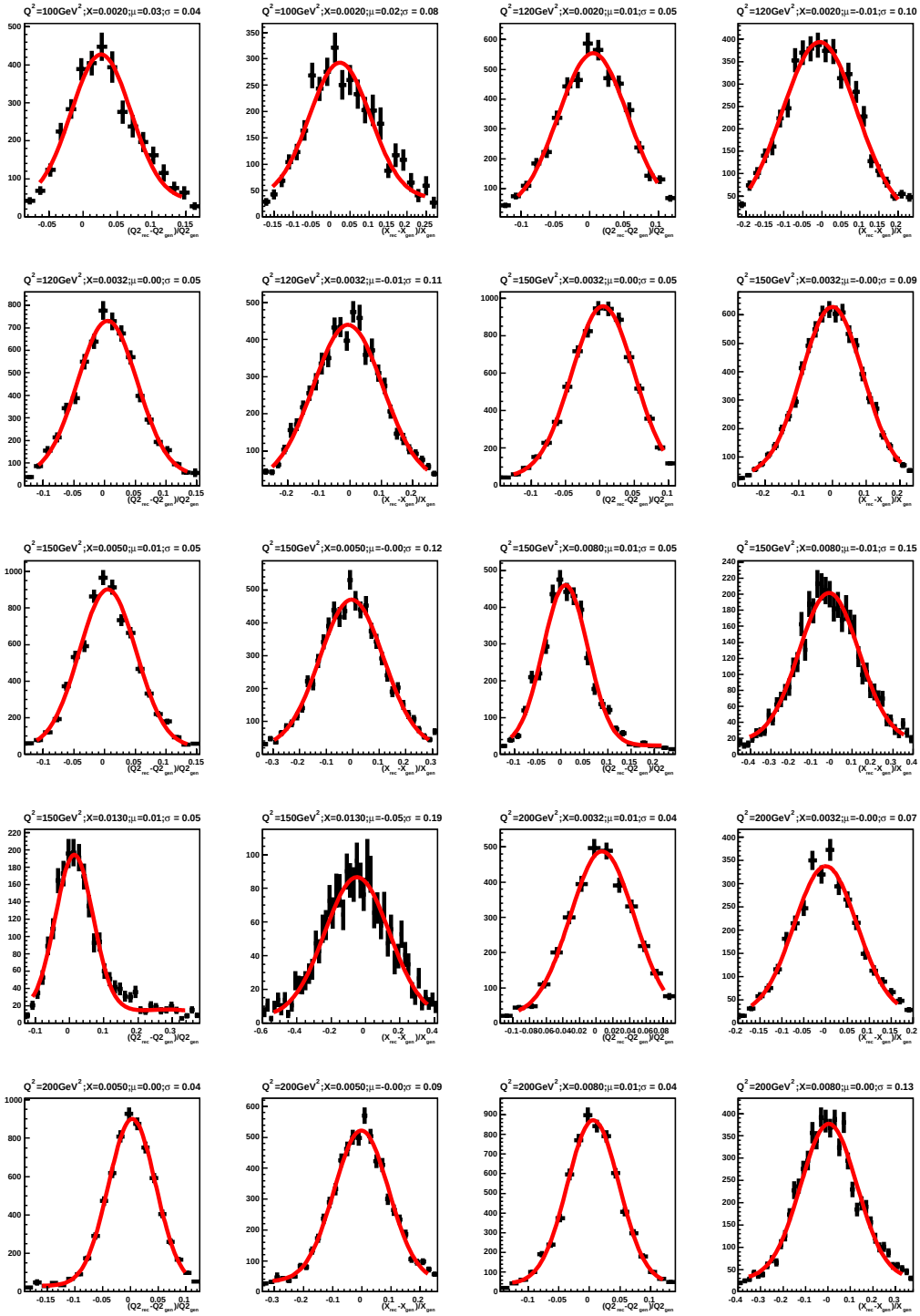

Figure B.13: *The distributions of* $\frac{Q^2_{rec} - Q^2_{gen}}{Q^2_{gen}}$ *and* $\frac{x_{rec} - x_{gen}}{x_{gen}}$ *used to determine the resolution of* Q^2 *and* x *for the chosen method of reconstruction used in the analysis (e-*Σ*). Each plot corresponds to a particular bin in* Q^2 *and* x*.*

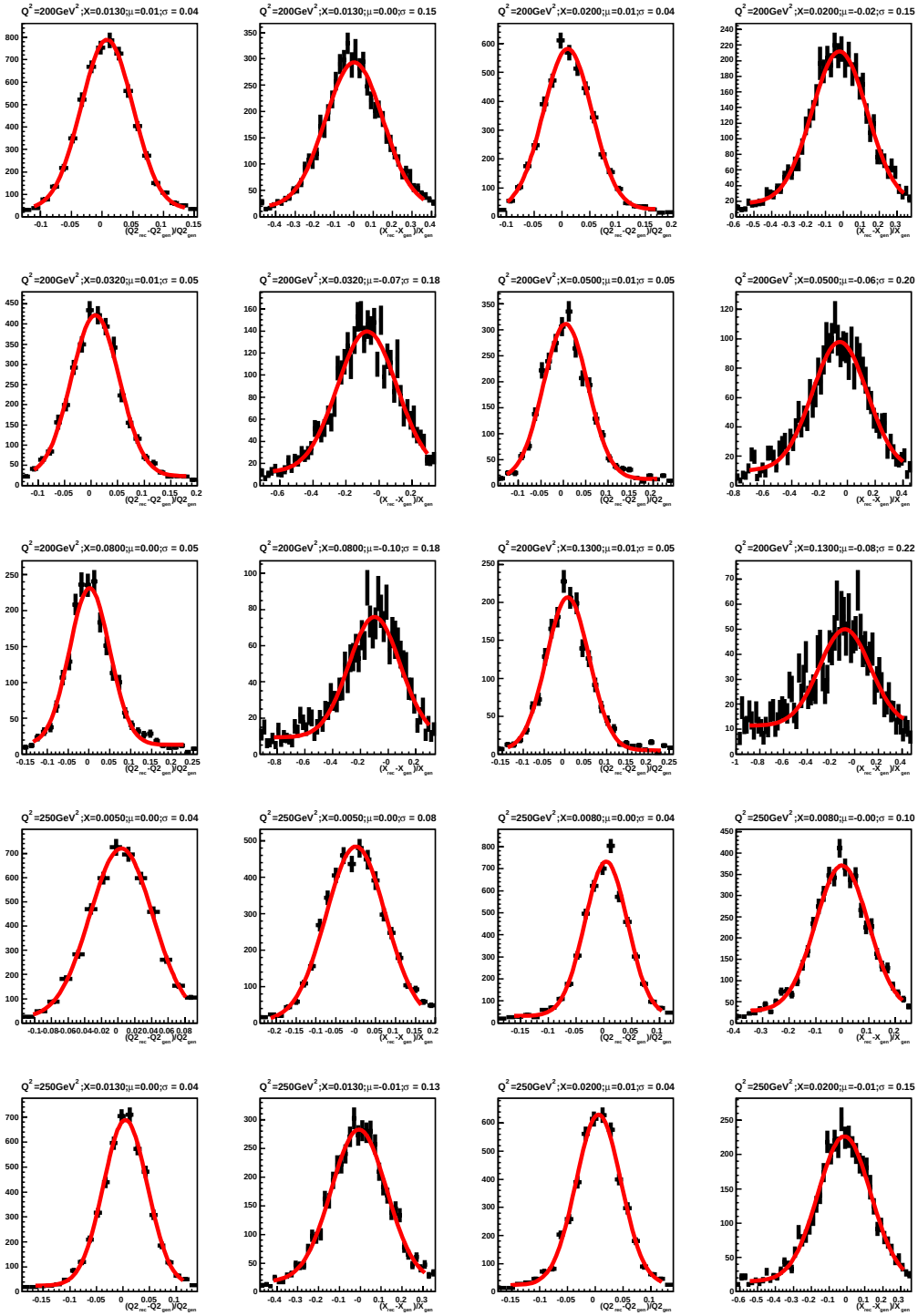

Figure B.14: *The distributions of* $\frac{Q^2_{rec} - Q^2_{gen}}{Q^2_{gen}}$ *and* $\frac{x_{rec} - x_{gen}}{x_{gen}}$ *used to determine the resolution of* Q^2 *and* x *for the chosen method of reconstruction used in the analysis (e-*Σ*). Each plot corresponds to a particular bin in* Q^2 *and* x*.*

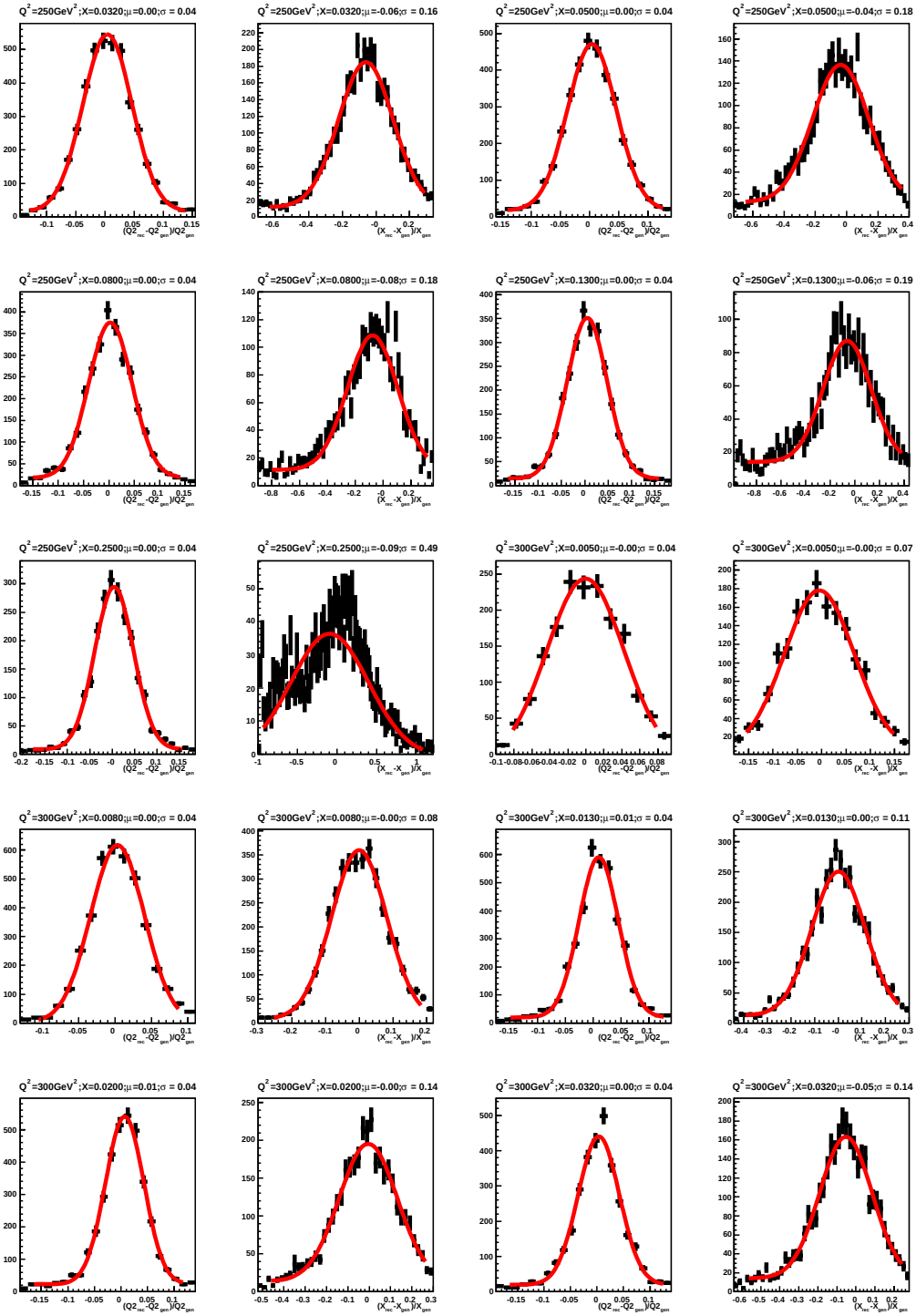

Figure B.15: *The distributions of* $\frac{Q^2_{rec} - Q^2_{gen}}{Q^2_{gen}}$ *and* $\frac{x_{rec} - x_{gen}}{x_{gen}}$ *used to determine the resolution of* Q^2 *and* x *for the chosen method of reconstruction used in the analysis (e-*Σ*). Each plot corresponds to a particular bin in* Q^2 *and* x*.*

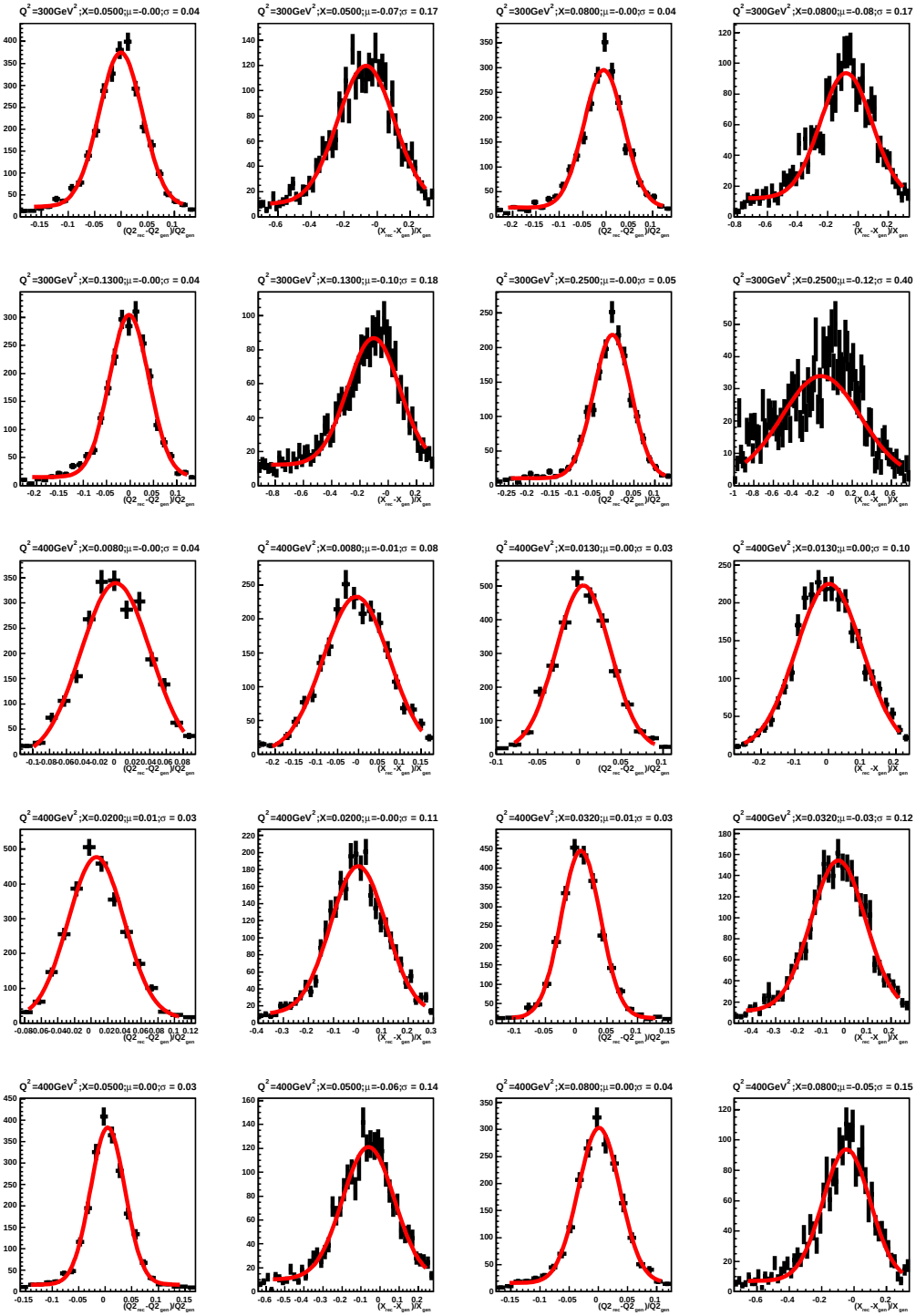

Figure B.16: *The distributions of* $\frac{Q^2_{rec} - Q^2_{gen}}{Q^2_{gen}}$ *and* $\frac{x_{rec} - x_{gen}}{x_{gen}}$ *used to determine the resolution of* Q^2 *and* x *for the chosen method of reconstruction used in the analysis (e-*Σ*). Each plot corresponds to a particular bin in* Q^2 *and* x*.*

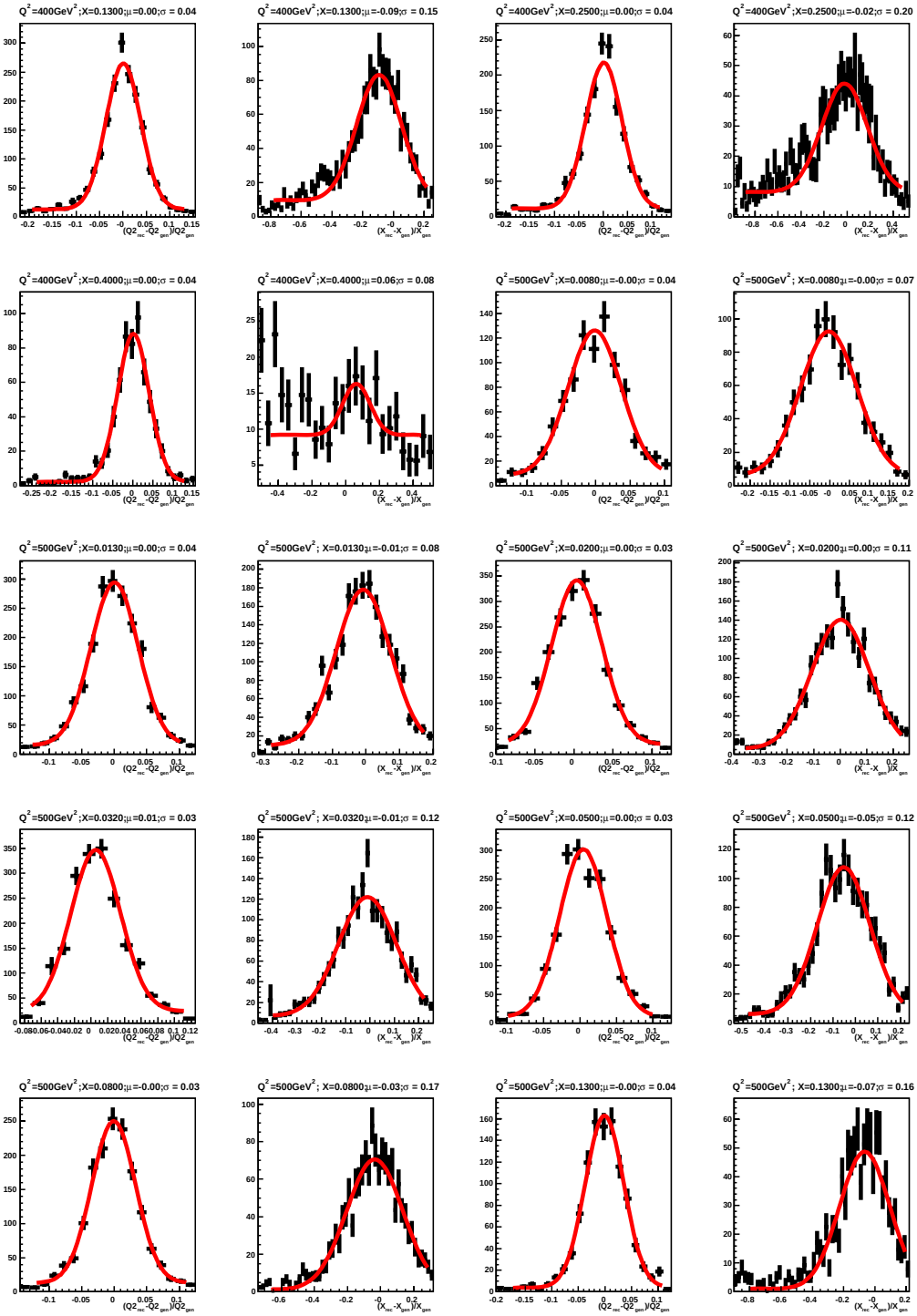

Figure B.17: *The distributions of* $\frac{Q^2_{rec} - Q^2_{gen}}{Q^2_{gen}}$ *and* $\frac{x_{rec} - x_{gen}}{x_{gen}}$ *used to determine the resolution of* Q^2 *and* x *for the chosen method of reconstruction used in the analysis (e-*Σ*). Each plot corresponds to a particular bin in* Q^2 *and* x*.*

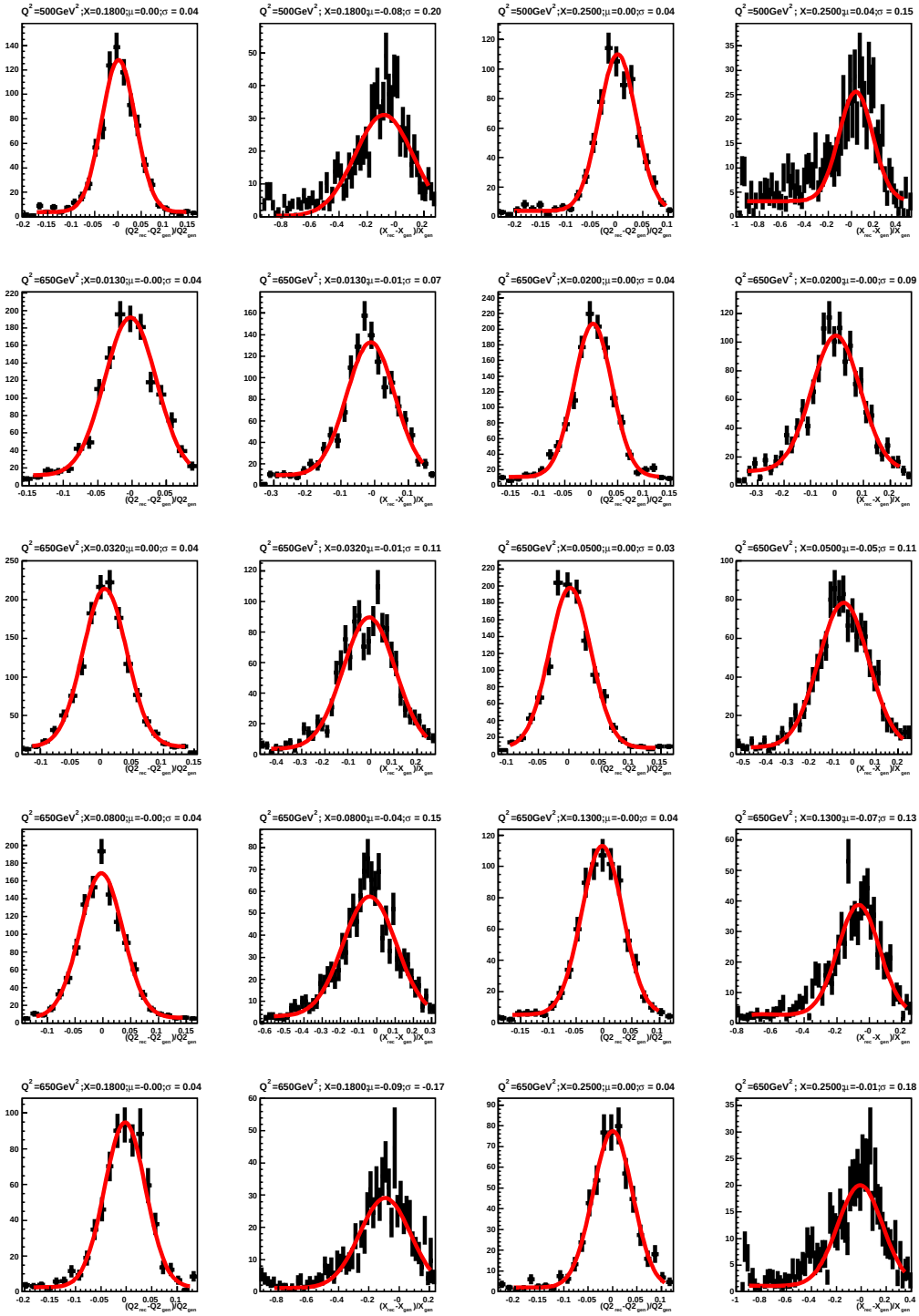

Figure B.18: *The distributions of* $\frac{Q^2_{rec} - Q^2_{gen}}{Q^2_{gen}}$ *and* $\frac{x_{rec} - x_{gen}}{x_{gen}}$ *used to determine the resolution of* Q^2 *and* x *for the chosen method of reconstruction used in the analysis (e-*Σ*). Each plot corresponds to a particular bin in* Q^2 *and* x*.*

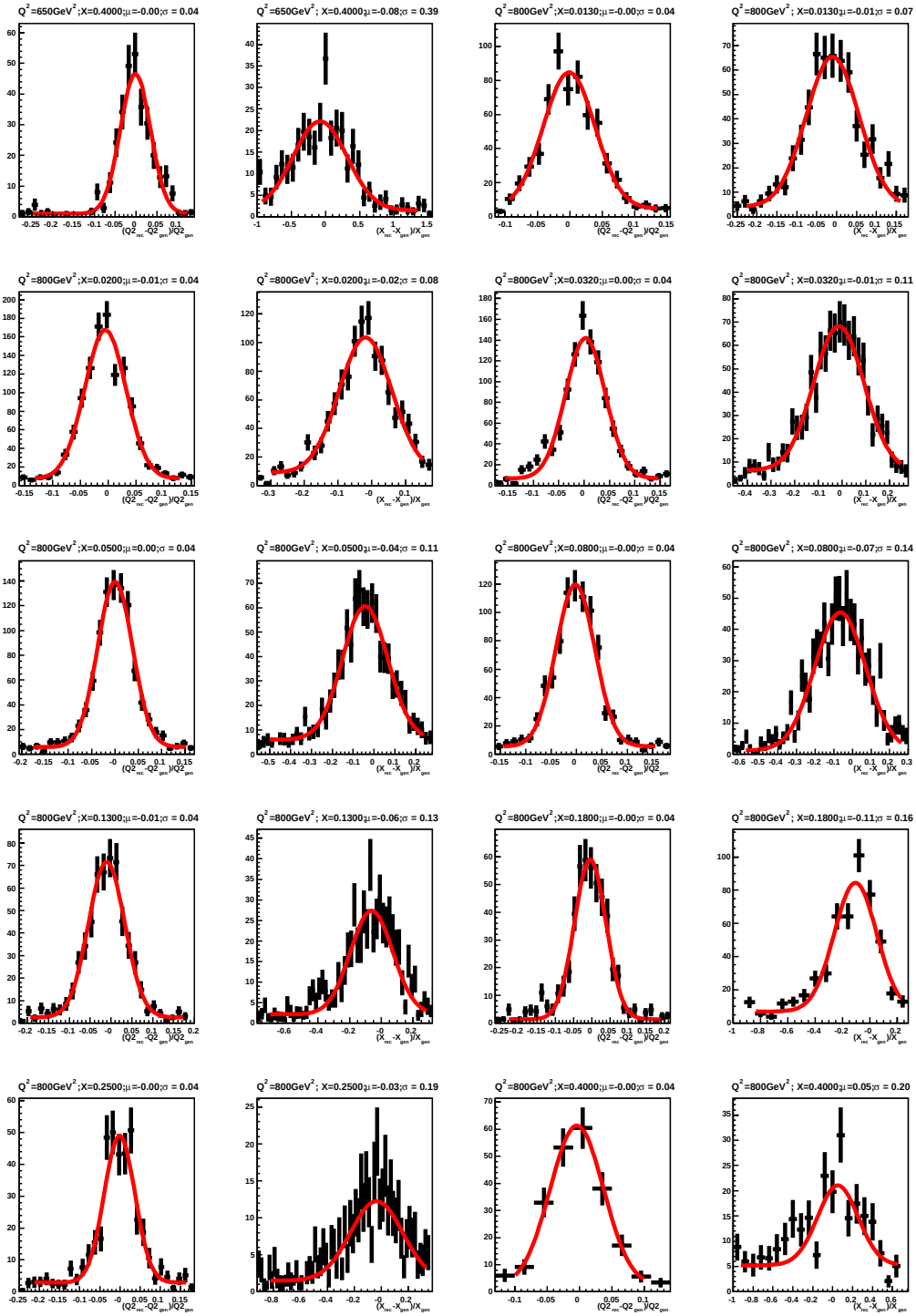

Figure B.19: *The distributions of* $\frac{Q^2_{rec} - Q^2_{gen}}{Q^2_{gen}}$ *and* $\frac{x_{rec} - x_{gen}}{x_{gen}}$ *used to determine the resolution of* Q^2 *and* x *for the chosen method of reconstruction used in the analysis (e-*Σ*). Each plot corresponds to a particular bin in* Q^2 *and* x*.*

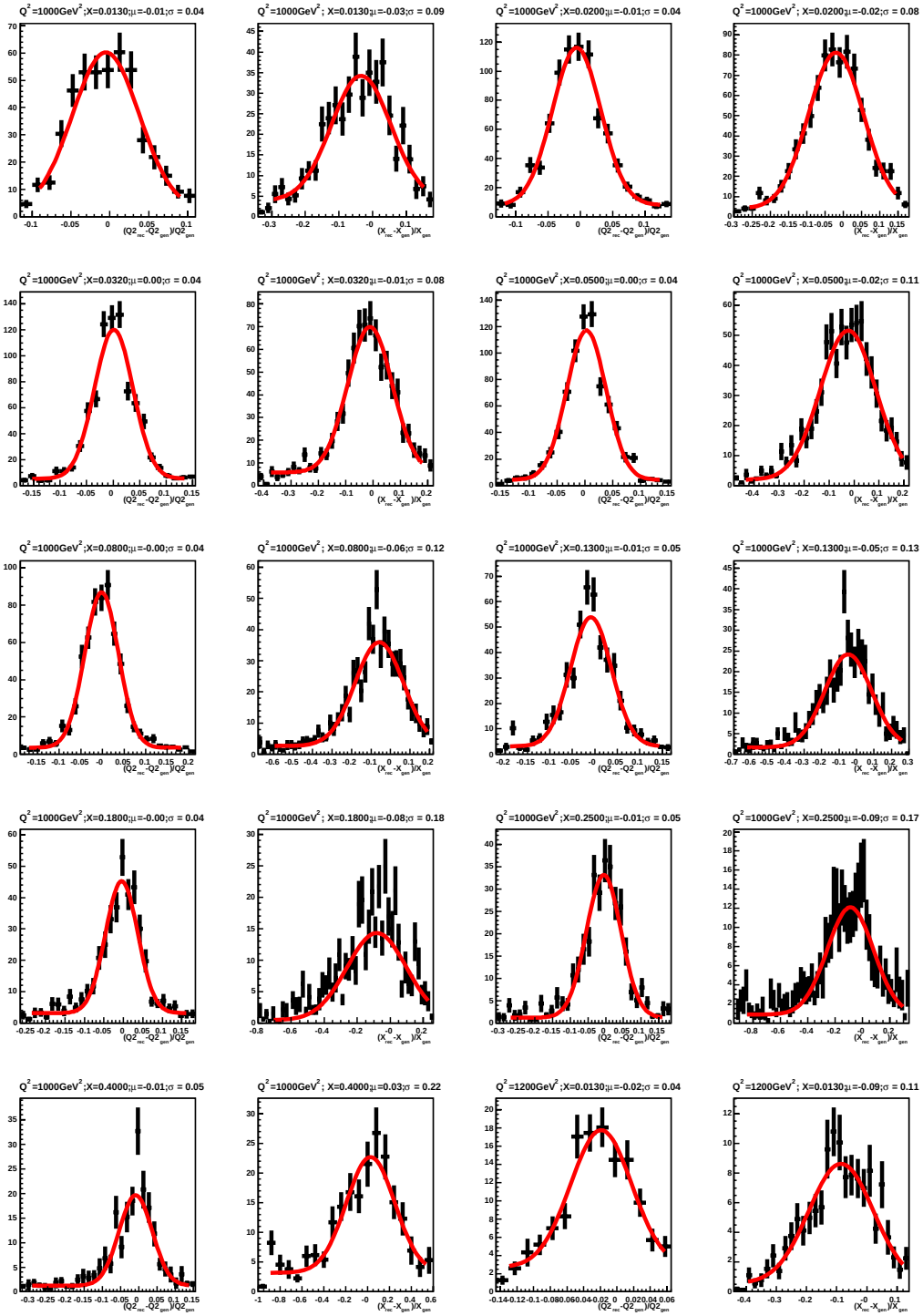

Figure B.20: *The distributions of* $\frac{Q^2_{rec} - Q^2_{gen}}{Q^2_{gen}}$ *and* $\frac{x_{rec} - x_{gen}}{x_{gen}}$ *used to determine the resolution of* Q^2 *and* x *for the chosen method of reconstruction used in the analysis (e-*Σ*). Each plot corresponds to a particular bin in* Q^2 *and* x*.*

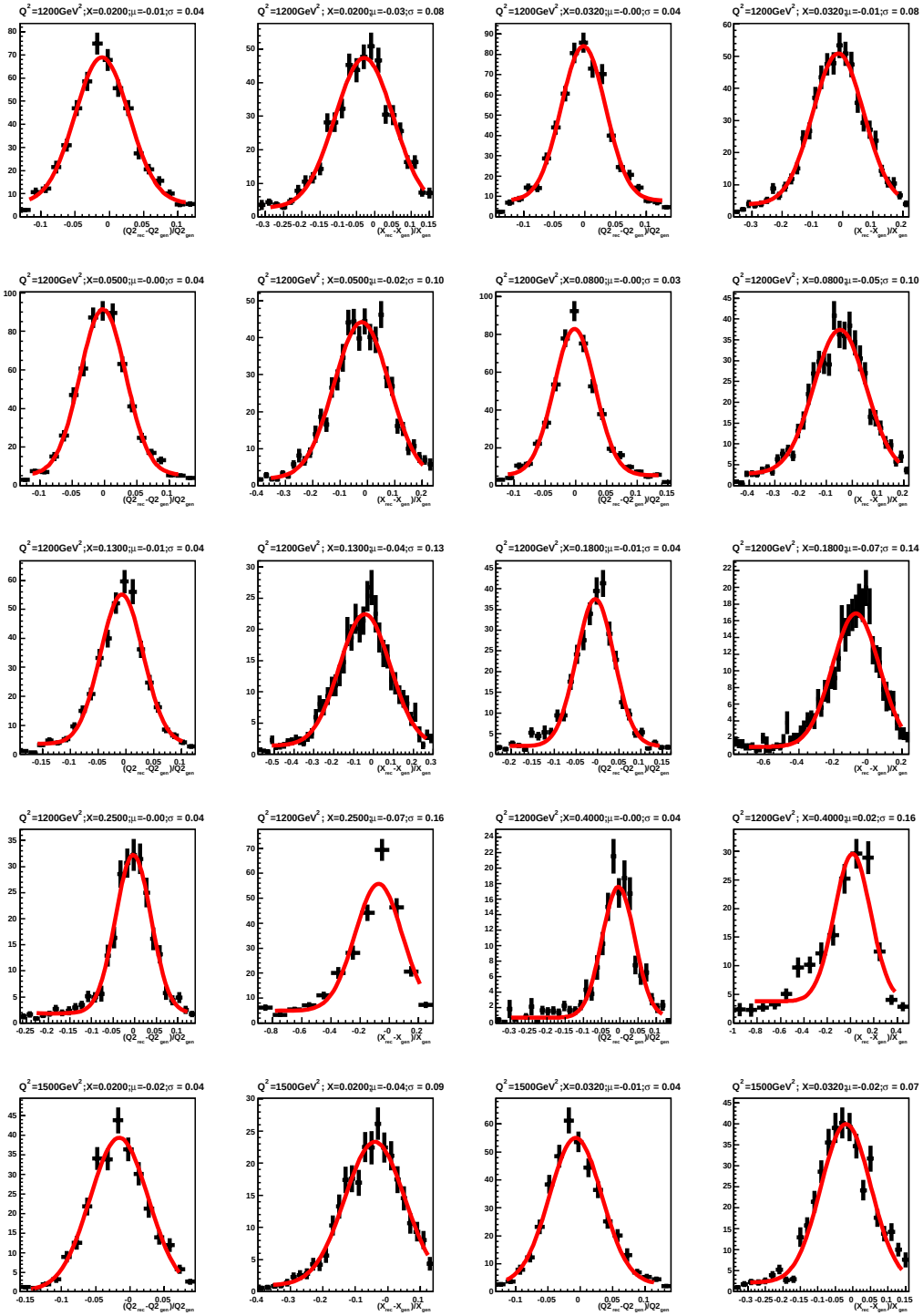

Figure B.21: *The distributions of* $\frac{Q^2_{rec} - Q^2_{gen}}{Q^2_{gen}}$ *and* $\frac{x_{rec} - x_{gen}}{x_{gen}}$ *used to determine the resolution of* Q^2 *and* x *for the chosen method of reconstruction used in the analysis (e-*Σ*). Each plot corresponds to a particular bin in* Q^2 *and* x*.*

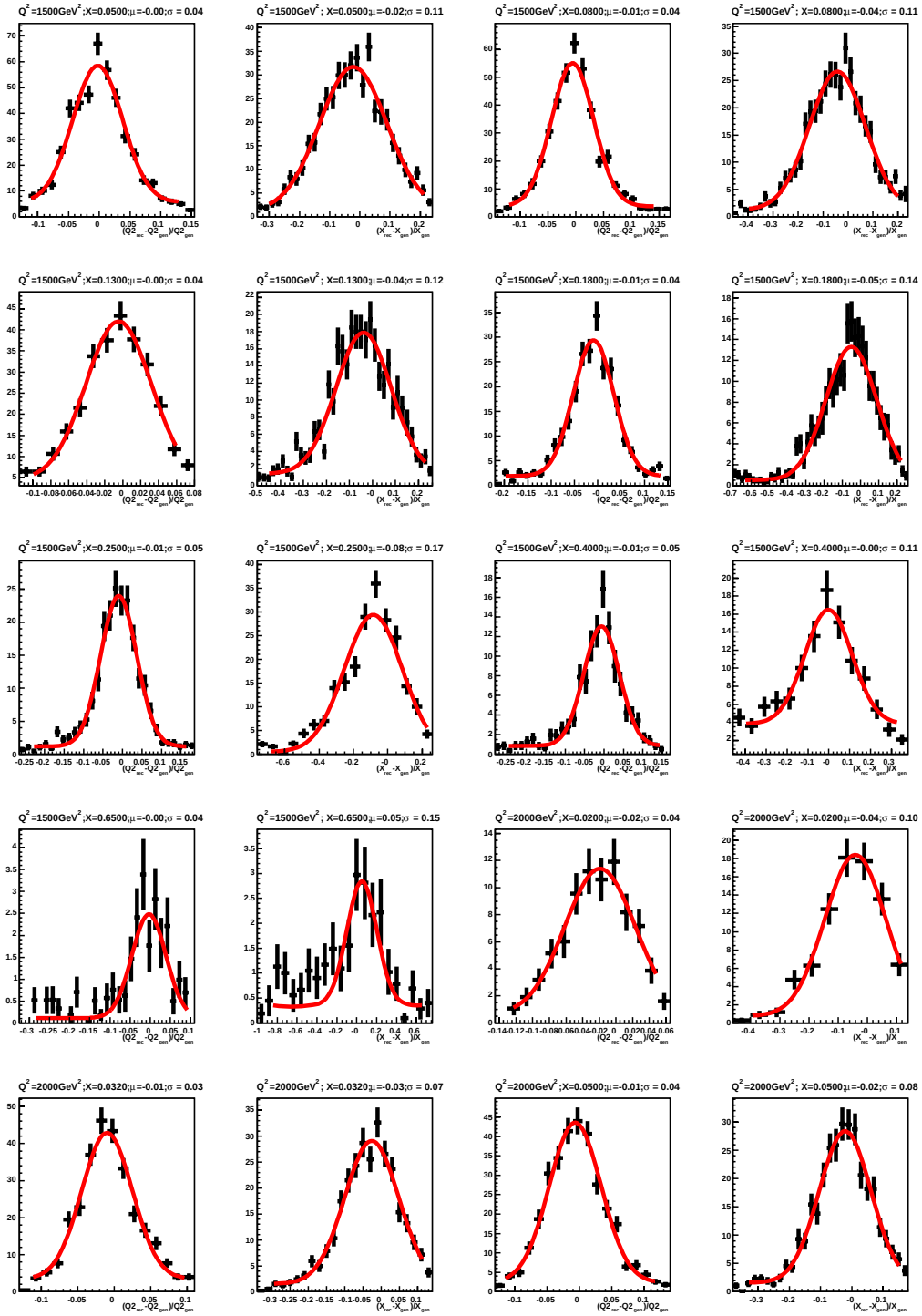

Figure B.22: *The distributions of* $\frac{Q^2_{rec} - Q^2_{gen}}{Q^2_{gen}}$ *and* $\frac{x_{rec} - x_{gen}}{x_{gen}}$ *used to determine the resolution of* Q^2 *and* x *for the chosen method of reconstruction used in the analysis (e-*Σ*). Each plot corresponds to a particular bin in* Q^2 *and* x*.*

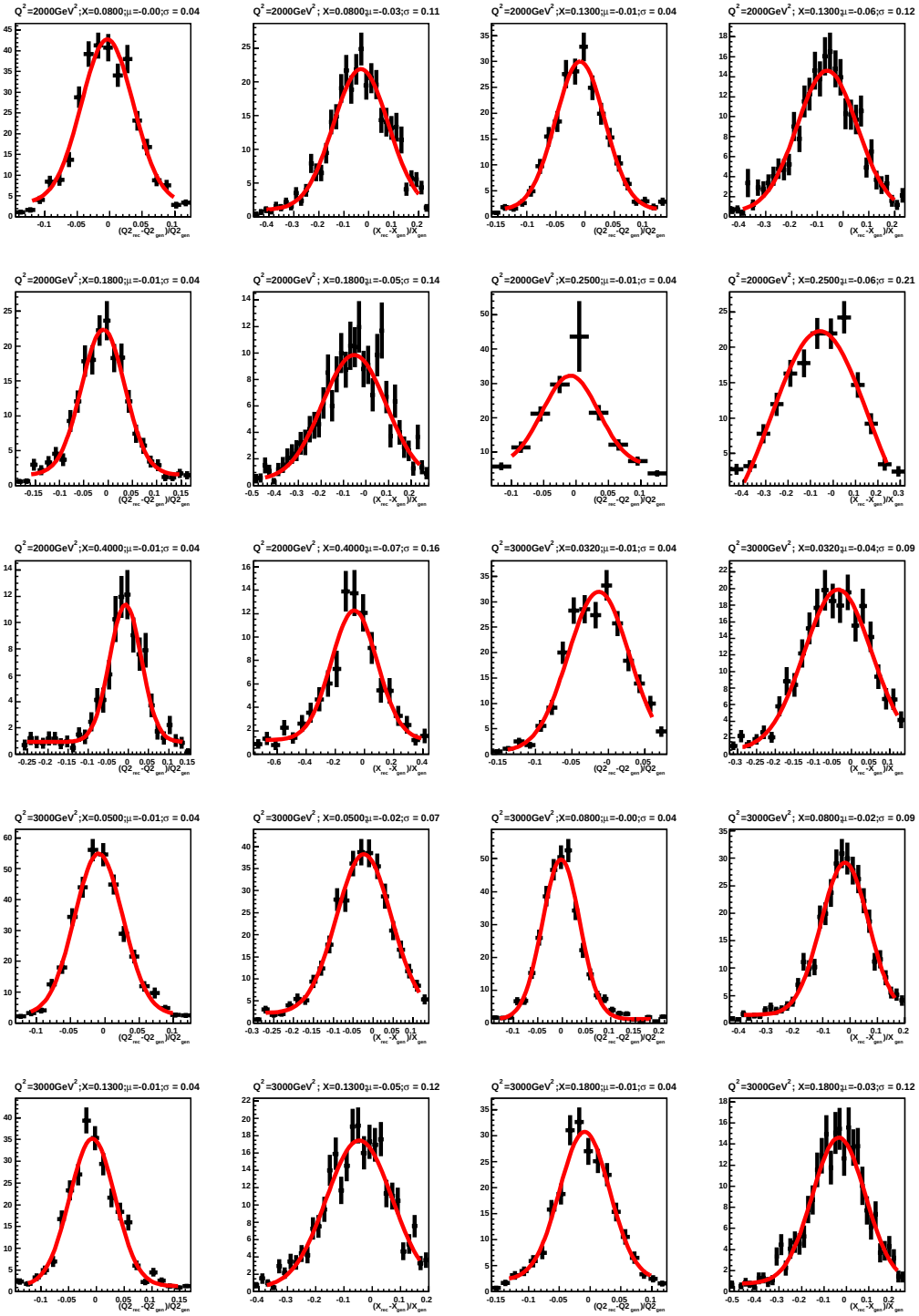

Figure B.23: *The distributions of* $\frac{Q^2_{rec} - Q^2_{gen}}{Q^2_{gen}}$ *and* $\frac{x_{rec} - x_{gen}}{x_{gen}}$ *used to determine the resolution of* Q^2 *and* x *for the chosen method of reconstruction used in the analysis (e-*Σ*). Each plot corresponds to a particular bin in* Q^2 *and* x*.*

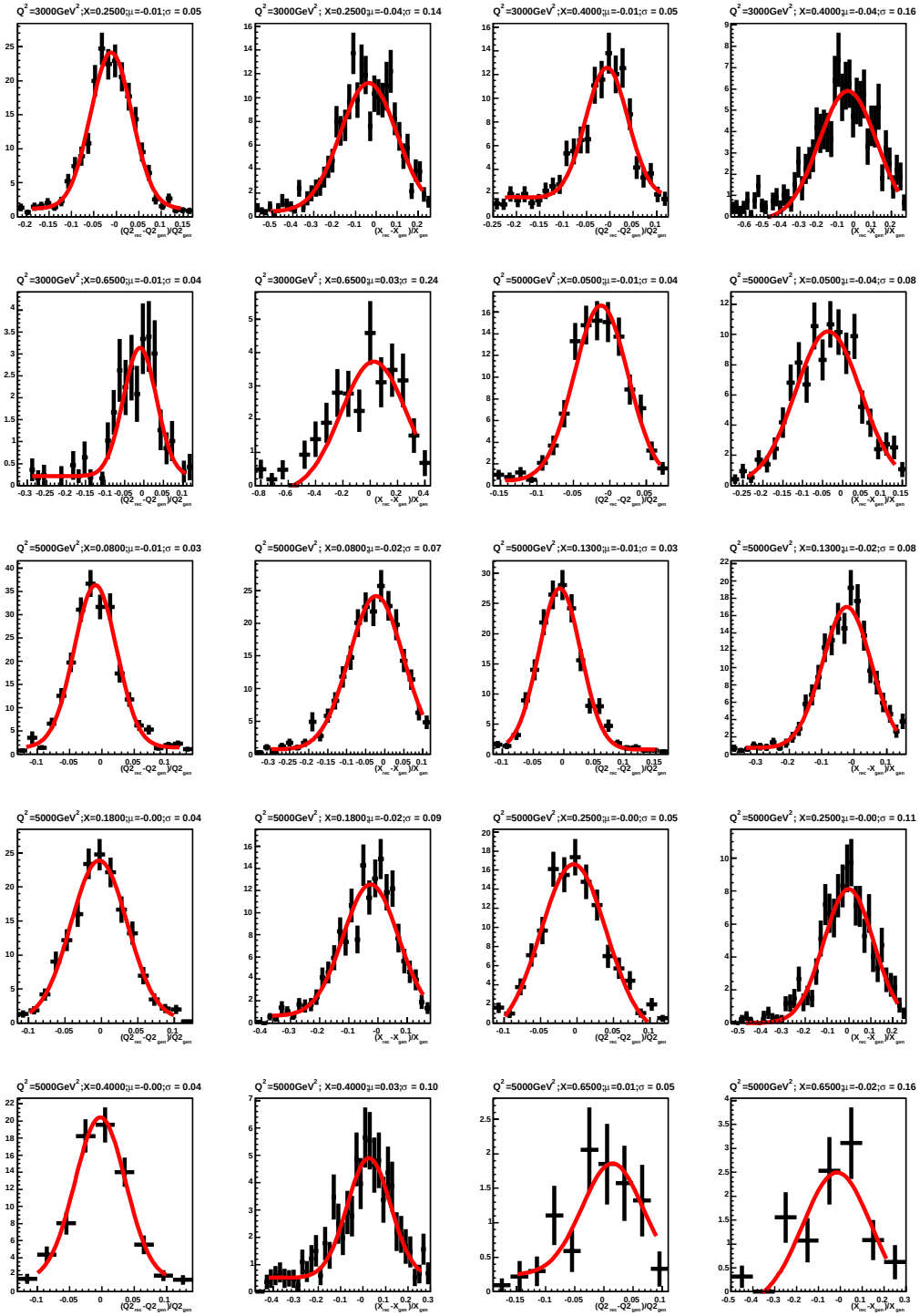

Figure B.24: *The distributions of* $\frac{Q^2_{rec} - Q^2_{gen}}{Q^2_{gen}}$ *and* $\frac{x_{rec} - x_{gen}}{x_{gen}}$ *used to determine the resolution of* Q^2 *and* x *for the chosen method of reconstruction used in the analysis (e-*Σ*). Each plot corresponds to a particular bin in* Q^2 *and* x*.*

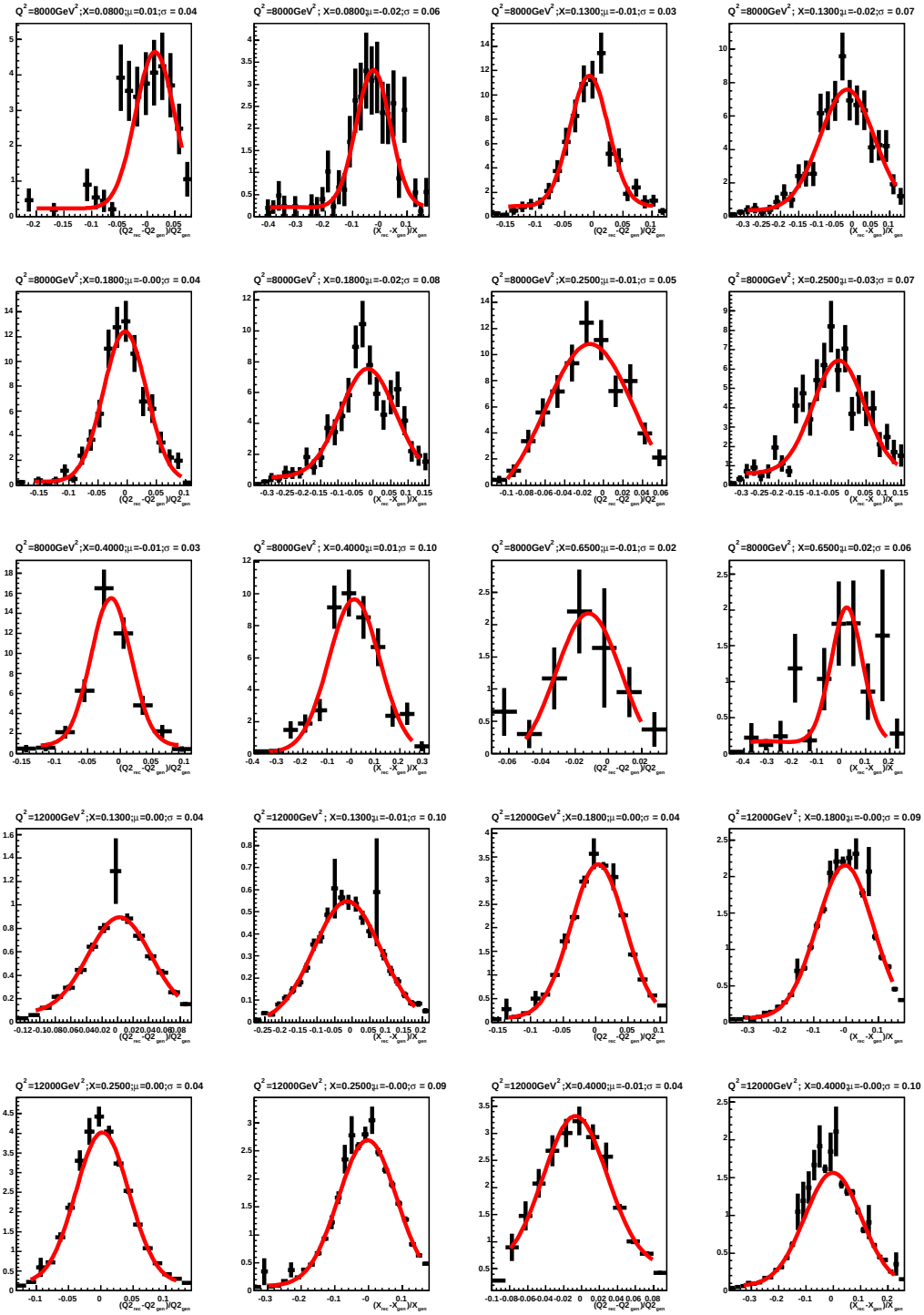

Figure B.25: *The distributions of* $\frac{Q^2_{rec} - Q^2_{gen}}{Q^2_{gen}}$ *and* $\frac{x_{rec} - x_{gen}}{x_{gen}}$ *used to determine the resolution of* Q^2 *and* x *for the chosen method of reconstruction used in the analysis (e-*Σ*). Each plot corresponds to a particular bin in* Q^2 *and* x*.*

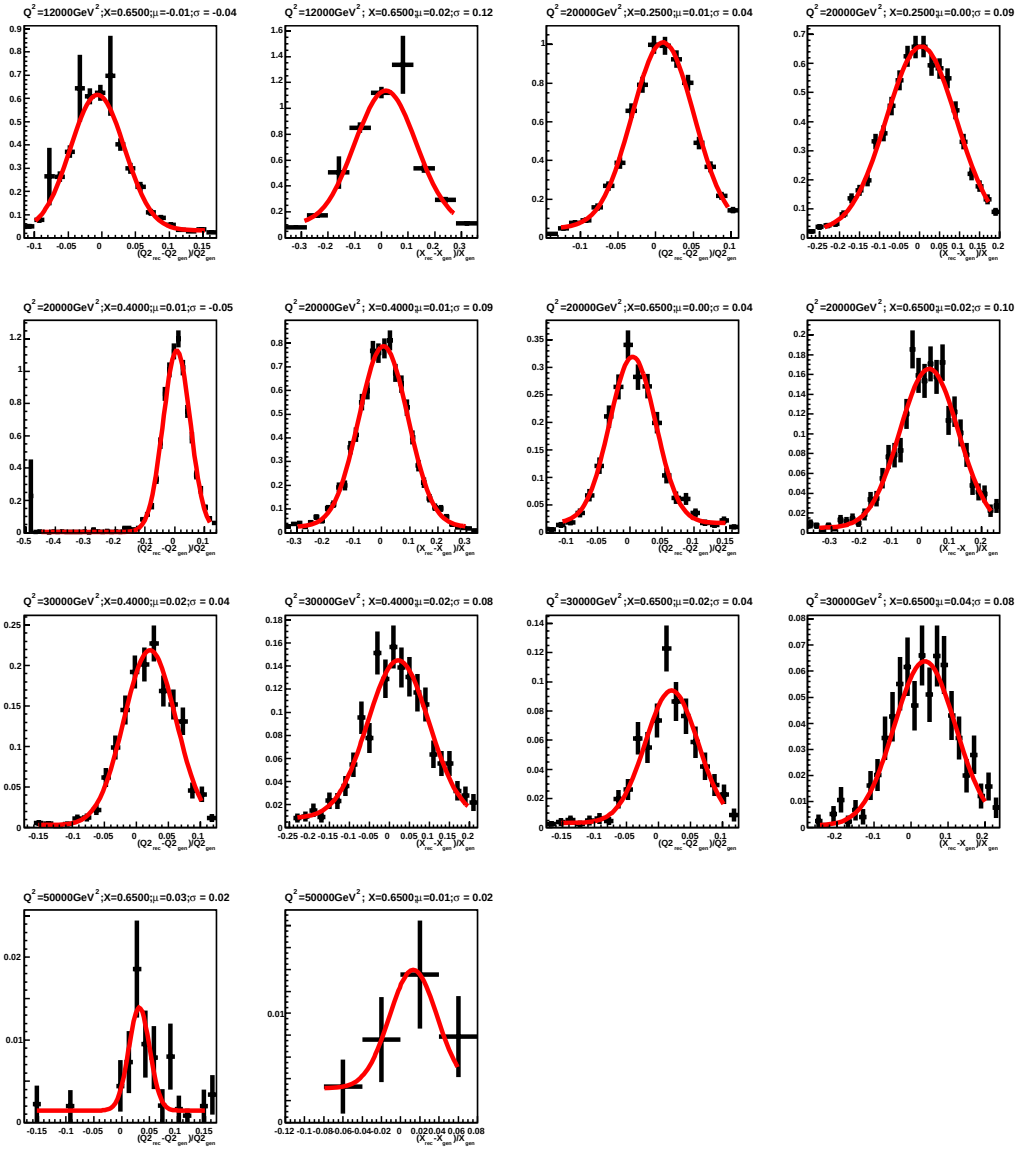

Figure B.26: *The distributions of* $\frac{Q^2_{rec} - Q^2_{gen}}{Q^2_{gen}}$ *and* $\frac{x_{rec} - x_{gen}}{x_{gen}}$ *used to determine the resolution of* Q^2 *and* x *for the chosen method of reconstruction used in the analysis (e-*Σ*). Each plot corresponds to a particular bin in* Q^2 *and* x*.*

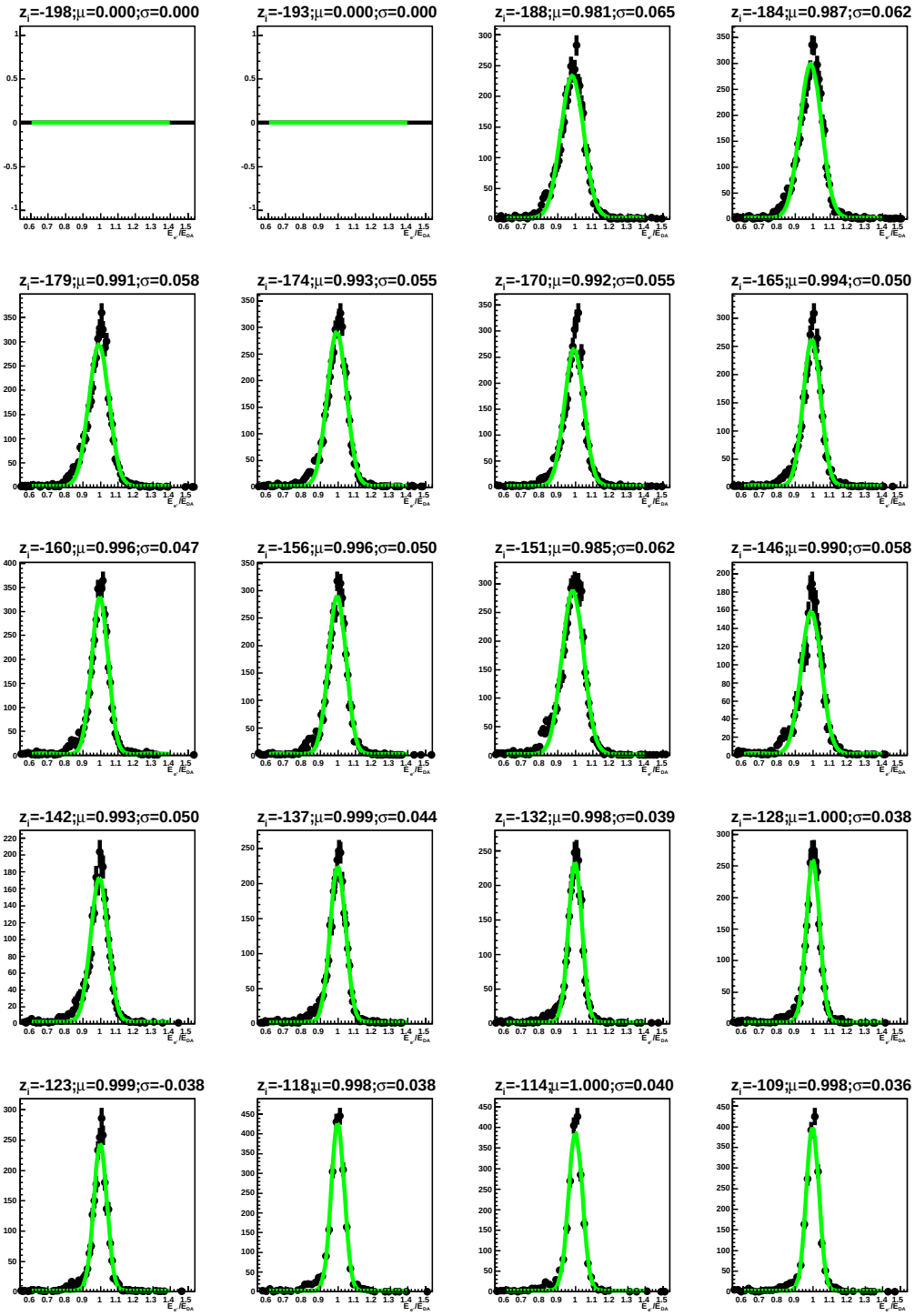

Figure B.27: *The* $\frac{E_{e'}}{E_{DA}}$ *distributions for data used to determine the resolution and systematic error of the energy calibration. Each plot corresponds to a particular bin in z-impact.*

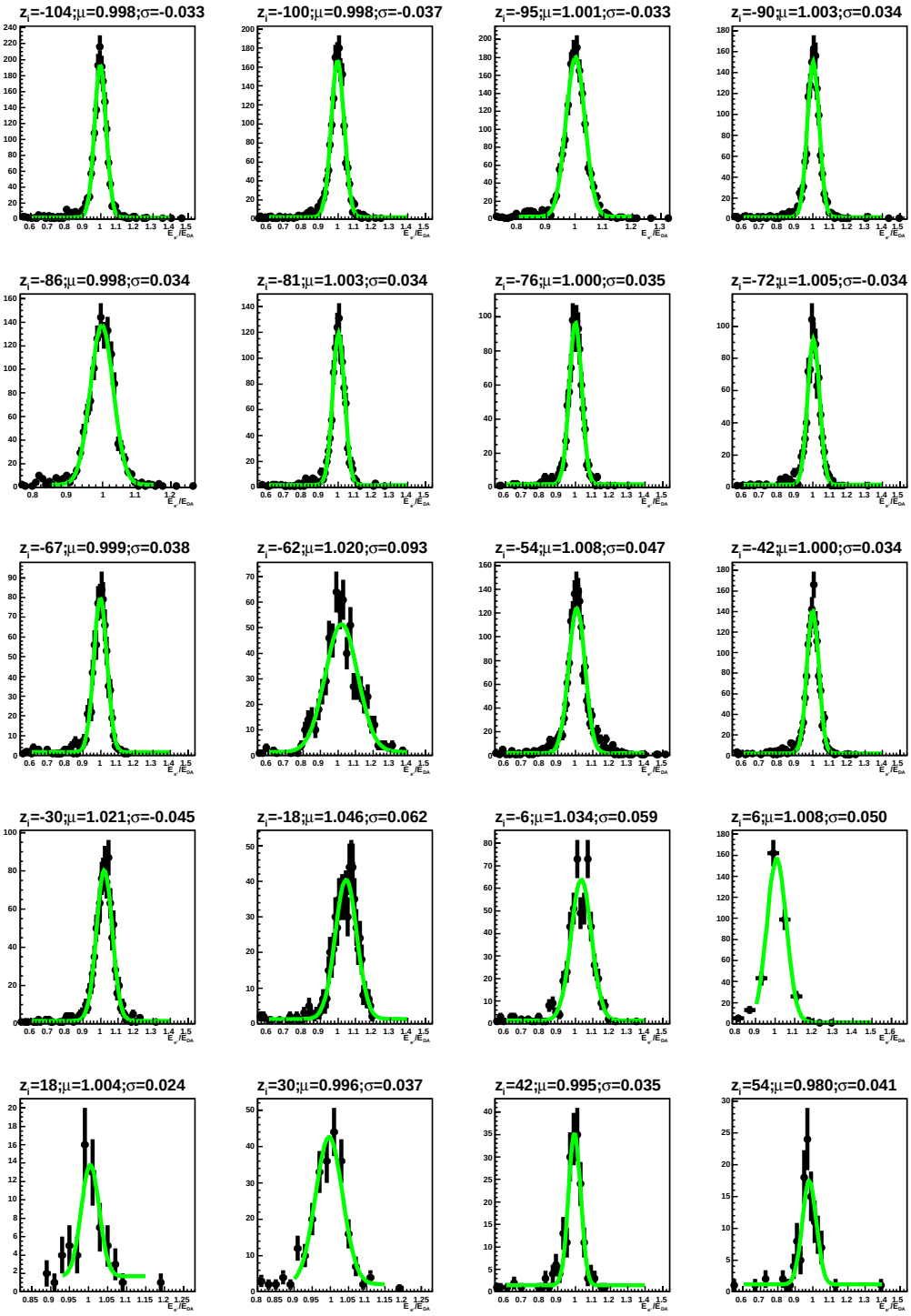

Figure B.28: *The* $\frac{E_{e'}}{E_{DA}}$ *distributions for data used to determine the resolution and systematic error of the energy calibration. Each plot corresponds to a particular bin in z-impact.*

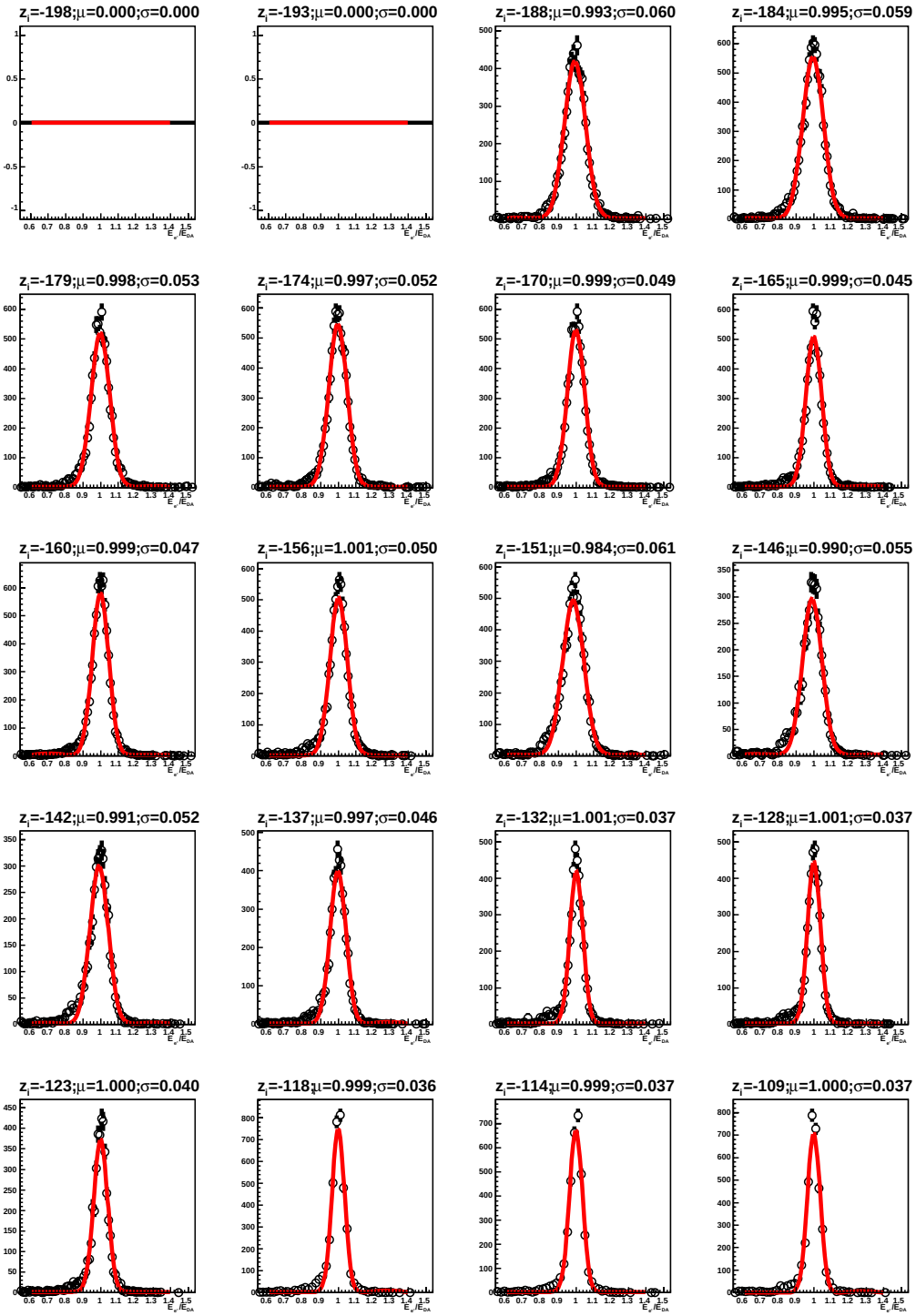

Figure B.29: *The* $\frac{E_{e'}}{E_{DA}}$ *distributions for signal MC used to determine the resolution and systematic error of the energy calibration. Each plot corresponds to a particular bin in z-impact.*

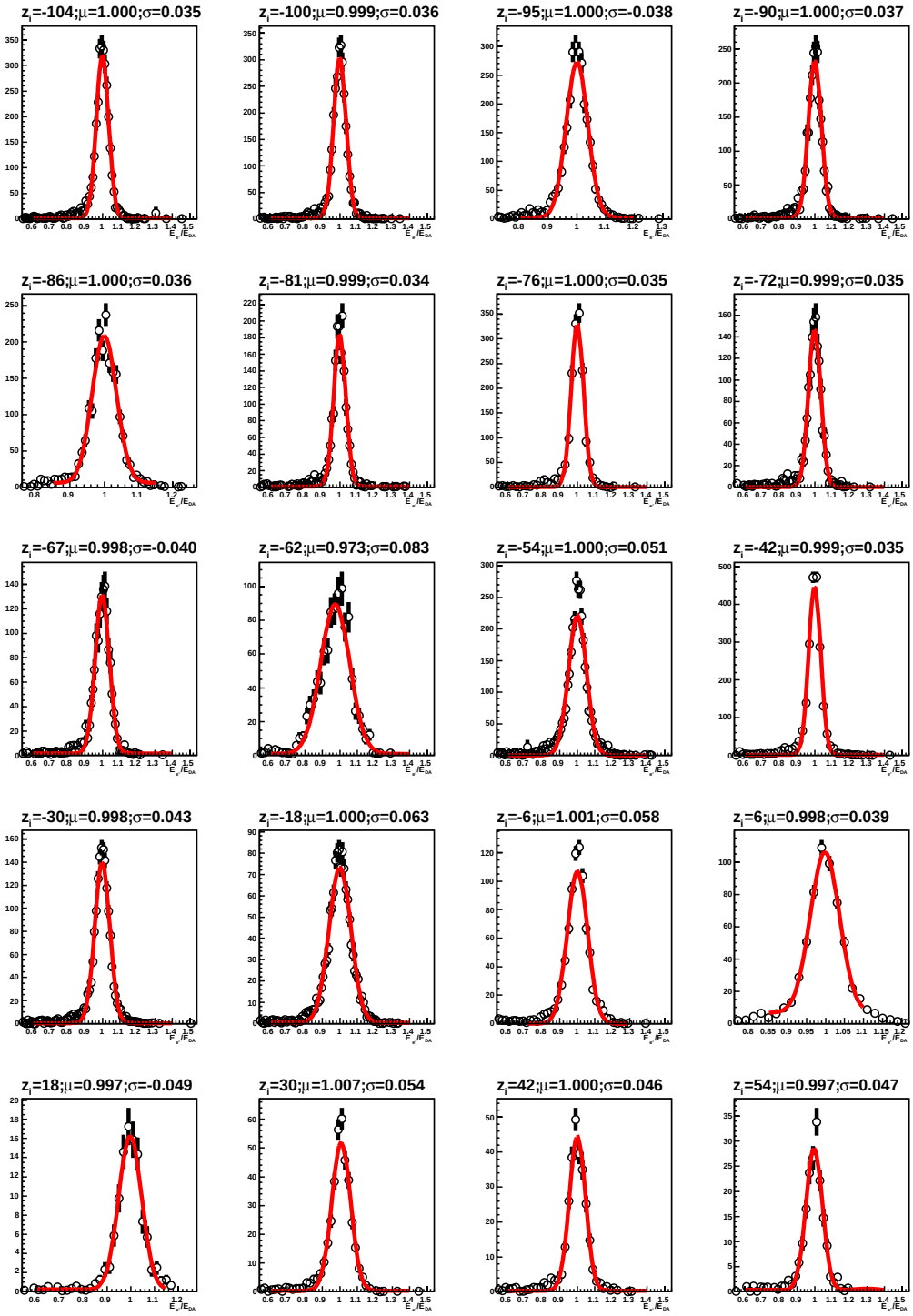

Figure B.30: *The* $\frac{E_{e'}}{E_{DA}}$ *distributions for signal MC used to determine the resolution and systematic error of the energy calibration. Each plot corresponds to a particular bin in z-impact.*

Acknowledgements

I've neglected to mention in *Chapter* 2 the most important part of an experiment, the people. I have to say many thanks to those that have helped me over the past year, and were generous with their time and knowledge. These are:

My Supervisor, Beate Naroska

Atkas Adil

Brandt Gerhard

Finke Lars

List Jenny

Lüders Henning

Martisikova Maria

Meyer Andreas

Meyer Joachim

Nikiforov Andrey

Olivier Bob

Platz Sabine

Rizvi Eram (and the guys from DESYUK)

Steder Michael.

I also wish to say thanks to the members of my group for making the workplace so enjoyable: Brian G., Christian B., Christian H., Christian S., Lea H., and Tammo G.

I wish to express a sense of gratitude to my institute, the International Centre for Graduate Studies (ICGS) for their support during my time here in Hamburg. Thank you

Dr. Thelen, Dr. Smidt, Shirlene, Karolin, Anja and Katherine. Thanks also to Professor R. Johnson for helping me find my way through my course of study.

Many thanks to the Deutscher Akademischer Austausch Dienst (DAAD) for their financial support.

To my family whom I love, it's good to know that even if we live on opposite sides of the planet, that you are still there for me: Zainool, Elisha, Sharon, Lystra, Feelisha and Azad.

To those friends whom I also love, and without whom my stay here would not have been the same: thanks Alexandra, Christoff, Mr. Larchenko, Sokhom, the Bach family and Raul Jacobs. Thanks Craig and Francis. My home group: Lida, Connie, Geysa, Sudhir and Carsten, you guys are great to hang out with. Freddy, you know that I have to mention you, as well as Rossi.

Finally, to the Great Time-splitter and Life-changer, Jesus Chris†. I wouldn´t have made it so far without you. Thanks for being in my boat over the past year and for your words of encouragement and comfort.

Bibliography

[1] *Introduction to Elementary Particles.* Wiley, 1987.

[2] Tetsuo Abe. Grape-dilepton (version 1.1): A generator for dilepton production in e p collisions. *Comput. Phys. Commun.*, 136:126–147, 2001.

[3] A.MEYER. *Measurement of the Structure Function $F_2(x, Q^2)$ of the Proton at Low Q^2 with the H1 Detector at HERA Using the New Detector Components Spacal and BDC.* PhD thesis, Universität Hamburg, 1997.

[4] B. Andrieu et al. The h1 liquid argon calorimeter system. *Nucl. Instrum. Meth.*, A336:460–498, 1993.

[5] B. Andrieu et al. Results from pion calibration runs for the h1 liquid argon calorimeter and comparisons with simulations. *Nucl. Instrum. Meth.*, A336:499–509, 1993.

[6] B. Andrieu et al. Beam tests and calibration of the h1 liquid argon calorimeter with electrons. *Nucl. Instrum. Meth.*, A350:57–72, 1994.

[7] Philippe Bruel. *Recherche d´interactions au-delà du Modèle Standard à HERA.* PhD thesis, L´Universite Paris XI Orsay, 1998.

[8] H1 Collaboration. Measurement of the polarisation dependence of the total e-p charged current cross section. Number H1prelim-05-042.

[9] DESY. *The Interface for the Event Generators HERACLES and LEPTO.*, volume 3 of *Proceedings of the Workshop: Physics at HERA*, October 1992.

[10] Ana Dubak. *Measurement of the e^+p Neutral Current DIS Cross Section and the F_2, F_L, xF_3 Structure Functions in the H1 Experiment at HERA.* PhD thesis, Technische Universität München, 2003.

[11] R.Brun et al. *GEANT3 User´s Guide*, 1987.

[12] E.WOEHRLING. *High Q2 Neutral Current Interactions at H1 and an Extraction of xF.* PhD thesis, The University of Birmingham, 2004.

[13] A. Blondel F. Jaquet. Proceedings of the study of an *ep* facility for europe. 1979.

[14] C. Adloff *et al.* H1 Collab. Measurement and qcd analysis of neutral and charged current cross sections at hera. *Eur. Phys. J. C.*, 30:1–32, 2003.

[15] Beate Heinemann. *Measurement of Charged Current and Neutral Cross Sections in Positron-Proton Collisions at* $\sqrt{s} \approx 300GeV$. PhD thesis, Universität Hamburg, 1999.

[16] G. Ingelman. Lepto version 6.1: The lund monte carlo for deep inelastic lepto - nucleon scattering. To appear in Proc. of Workshop on Physics at HERA, Hamburg, Germany, Oct 29-30, 1991.

[17] A. Kwiatkowski, H. Spiesberger, and H. J. Mohring. Heracles: An event generator for e p interactions at hera energies including radiative processes: Version 1.0. *Comp. Phys. Commun.*, 69:155–172, 1992.

[18] Alan D. Martin, W. James Stirling, and R. G. Roberts. Parton distributions updated. *Phys. Lett.*, B306:145–150, 1993.

[19] Emmanuel Sauvan Matti Peez, Benjamin Portheault. An energy flow algorithm for hadronic reconstruction in oo: Hadroo2, 2005.

[20] nElan Group. High q2 nc and cc binningh1nonepbgfinder. `http://www-h1.desy.de/h1/www/general/home/intra_home.html`.

[21] T. Nicholls et al. Performance of an electromagnetic lead / scintillating fiber calorimeter for the h1 detector. *Nucl. Instrum. Meth.*, A374:149–156, 1996.

[22] Andrey Nikiforov, July 2005. Private Communication.

[23] Torbjorn Sjostrand. High-energy physics event generation with pythia 5.7 and jetset 7.4. *Comput. Phys. Commun.*, 82:74–90, 1994.

[24] Torbjorn Sjostrand and Mats Bengtsson. The lund monte carlo for jet fragmentation and e+ e- physics: Jetset version 6.3: An update. *Comput. Phys. Commun.*, 43:367, 1987.

[25] H. Spiesberger *et al.* Proceedings of the workshop *Physics at HERA*, vol.2. 1992.

[26] D. E. Groom *et al.*[Particle Data Group Collaboration]. Eur. phys.j.c **15**. 2000.

[27] Max Christoph Urban. *The new CIP2k z-Vertex Trigger for the H1 Experiment at HERA*. PhD thesis, Universität Zürich, 2004.

[28] Christian Veelken. H1nonepbgfinder - rejection of cosmic muon and beam-halo events in the h100 framework, 2002.

[29] Ferdinand Willeke. Hera hits new heights. *CERN Courier*, 45:17–19, 2005.